A Complete Overview on Realizing Transfer-free Graphene-based Differential Pressure Sensor

R. Ramesha

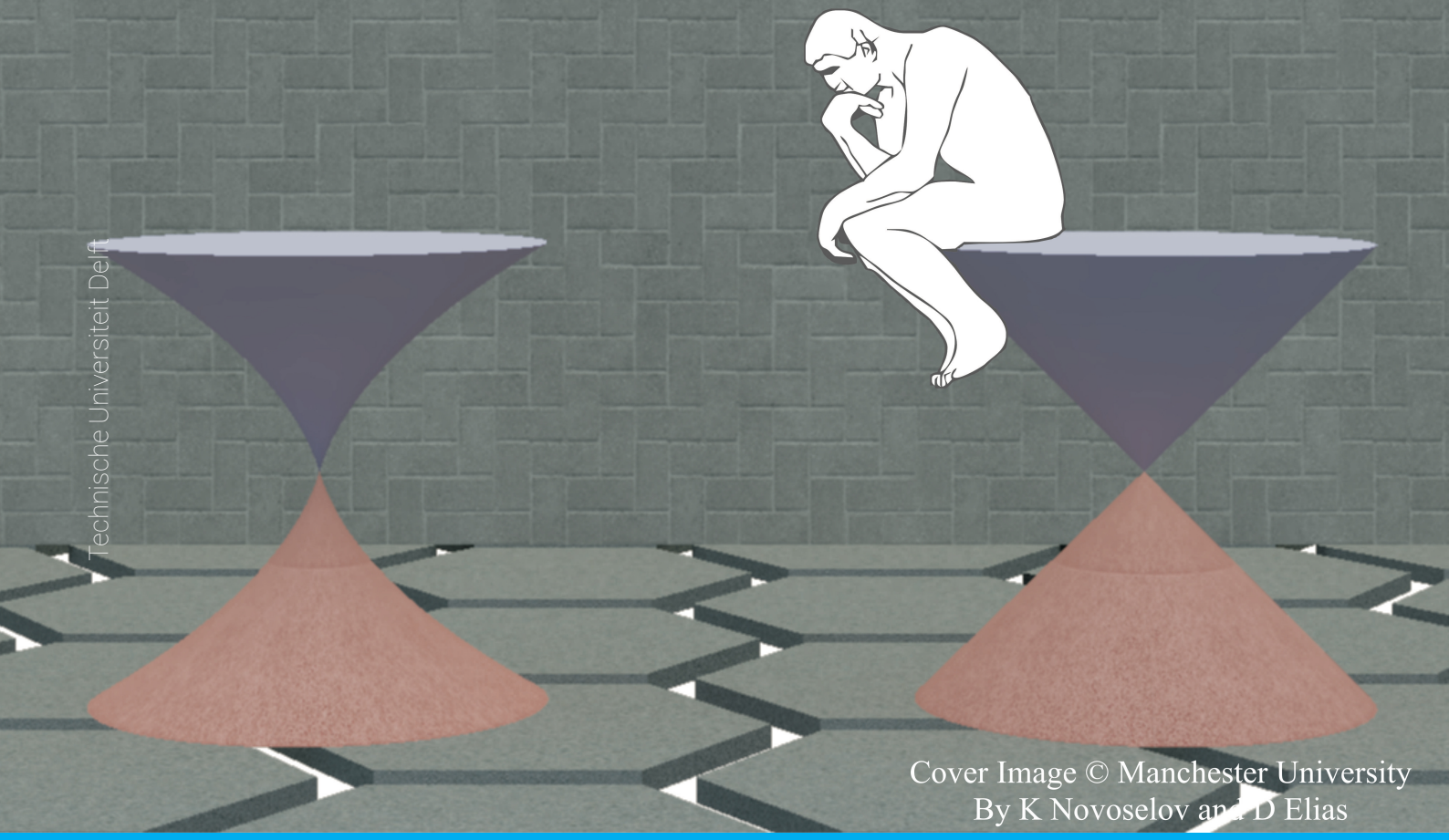

Cover Image © Manchester University
By K Novoselov and D Elias

Technische Universiteit Delft

TU Delft

A Complete Overview on Realizing Transfer-free Graphene-based Differential Pressure Sensor

by

R. Ramesha

to obtain the degree of Master of Science
at the Delft University of Technology,
to be defended publicly on Friday September 20, 2019 at 14:00 PM.

Student number:	4739701	
Project duration:	November 1, 2018 – September 20, 2019	
Thesis committee:	Dr. ir. S. Vollebregt,	TU Delft, supervisor
	Prof. Dr. P. M. Sarro,	TU Delft
	Prof. Dr. P. G. Steeneken,	TU Delft

This thesis is confidential and cannot be made public until September 20, 2020.

TU Delft

The peace of God is with
them whose mind and soul are
in harmony, who are
free from desire and wrath, who
know their own soul

THE GEETA

Preface

This thesis is a part of the Master graduation program that is conducted in partial fulfillment for the degree Master of Science in Electrical Engineering. The thesis project was performed for ten months and during the project, transfer-free graphene-based differential pressure sensors were successfully designed, fabricated and characterized. In doing so, transfer-free graphene processing was successfully integrated into semiconductor bulk micro-machining processes.

The first stage of the project consisted of a literature review to asses the feasibility of this project. This was followed by building and validating a simulation model on *COMSOL Multiphysics* and concluding on the design parameters through them.

During the next phase, I underwent training for Cleanroon processing. The training I received under the guidance of Silvana, Tom and Mario is immensely valuable.

The next phase consisted of converting my design parameters into mask designs using L-Edit. Discussions with Henk van Zeijl were extremely informative. A total of five masks were used for fabrication of the devices.

In the following stage, the devices were fabricated in the cleanroom. This was the longest stage of my thesis project. The first batch of processing was started in the first week of May and it concluded in the last week of August.

The final stage consisted of building a pressure measurement setup. The setup consisted of a pressure redistribution chuck designed by Jia Wei, a vacuum pump and a pressure controller. The fine tuning of the setup took some time and the vaccum leaks were as minimized as possible. Further the device was characterized on the four point probe and on Keyence Laser Scanning microscope. The measurement results were successful and the transfer-free graphene processing was successfully integrated with bulk micro-machining.

The thesis committee consists of professor Lina Sarro, the head of ECTM Laboratory, my supervisor Sten Vollebregt and professor Peter Steeneken from 3ME.

R. Ramesha
Delft, September 2019

Abstract

braphene is an attractive material to be used for pressure sensors due to its thinness, electrical conductivity, and potential high gauge factor. One of the issues with processing graphene is the scalability, which is largely limited by the transfer process that is required for graphene deposited by chemical vapour deposition (CVD). In this work we employed a novel, transfer-free bulk-micromachining approach to realize graphene-based differential pressure sensors. The devices were successfully fabricated, and the samples were examined under Raman Spectroscopy, and electrically characterized. Further, pressure dependent measurements were performed for a dynamic range of 0 to 80 kPa of differential pressure and the corresponding change in resistance of the membrane was measured. The fabricated device have a mean gauge factor of 2.80.

Contents

1

Introduction

The modern world is driven by technology. One of the main driving forces behind the technological advancement is electronics. Electronics play a huge role in our day to day life. From modern gadgets like smartphones, to electronics that control avionics in an airplane and to supercomputers that predict the behaviour of atoms. The application of electronics is endless. The technological advancement took a giant leap since the discovery of semiconductors like Silicon. Silicon is abundantly available on Earth, has taken multiple forms in the world of electronics. It first started with *Bipolar Junction Transistors*, then to *MOSFETs* and now *FINFETs*. The demand for Silicon based electronics gave rise to an industry which by today's standards is worth more than 400 Billion USD. However, our curiosity did not stop there. Researchers explored other properties of Silicon like mechanical, optical and chemical. With the help of tools available in the semiconductor industry devices like Si-based strain gauges, Si-based pressure sensors, Si-based temperature sensors, to name a few were developed. These devices have undergone a series of optimizations and they are almost at the peak of their performance in terms of sensitivity, power consumption and noise optimization [4]. It would be extremely difficult to optimize these devices further since the material physics has become the limiting factor. Hence, to have better devices than the current ones, we need to look at new materials that have better physical properties than the existing ones.

In their quest for novel materials, A.K Geim and K. Novoselov isolated one such material called graphene [5]. Graphene is a Carbon allotrope, one atom in thickness (mono-layer) and the atoms are arranged in a honey-comb hexagonal fashion. Graphene can be considered as an infinitely large aromatic molecule. Graphene has excellent mechanical, electrical, optical, chemical and thermal properties [5]. Using these properties, we can improve the performance of many devices . One such example has been in the field of sensors. Graphene based Hall-effect and chemical sensors have shown excellent performance than their Si counterparts ([6], [7]).

However, they have not yet been realized to their potential in terms of a technological break through. This is partly due to the fact that most of the tools in the industry are mainly based on semiconductor processing and standards. Hence, to make graphene devices scalable and also to increase the through-put, it is very necessary to find a common ground between the two and integrate graphene processing into the standards of semiconductor processing.

In the initial years, graphene was mechanically exfoliated from graphite into mono-layers. This technique produced graphene of excellent quality, but their dimensions were limited and hence, achieving scalability through this technique of graphene production became a challenge. In the recent years, many novel methods for graphene production have been tried, but, it is Chemical Vapor

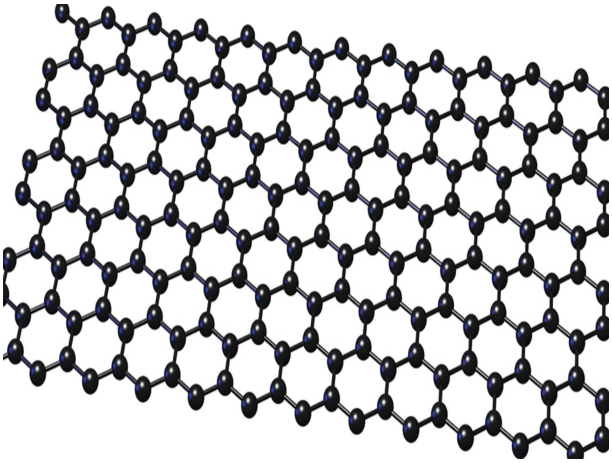

Figure 1.1: Graphene mono-layer. Visible, the hexagonal atomic structure. Taken from [8]

Deposition (CVD) of graphene that has shown most promise towards achieving better scalability. In this technique, graphene is chemically grown over a transition-metal catalyst with the use of hydrocarbons at a high temperature. Generally, CVD grown graphene undergoes a transfer process, where graphene is transferred from the catalyst interface to a semicaonductor wafer using polymers like *PMMA*. Transfer techniques of graphene have been known to cause wrinkles in the graphene membrane which can hamper the properties of graphene [9]. Additionally, they are known to cause polymer contamination and pin holes in the membrane. The transfer techniques have been a hurdle in graphene processing and has affected graphene scalability too [10].

In this research work, we present a novel transfer free approach to graphene processing. Here, we aim to integrate graphene processing into bulk-micromachining to fabricate graphene-based differential pressure sensors. This method is based on previous results by Vollebregt et al [11], which we extended for the first time to bulk micro-machining.

1.1. Problem Statement

As discussed in the earlier section, the transfer process of CVD graphene has been a hurdle in achieving better scalability for graphene-based devices. Since there is no process flow that has a transfer-free integration of graphene to bulk-micromachining, it would be of prime value to investigate the feasibility of this approach with the tools and standards available for semiconductor bulk micromachining. Hence, the fundamental research question of this work is:

"Can graphene processing be integrated into standard semiconductor bulk micromachining using the transfer-free approach?"

Furthermore, we employ the transfer-free approach to design a graphene-based differential pressure sensor. Although researchers have worked on graphene-based pressure sensors, all of them are based on transferred graphene. Hence, the additional research question can be framed as:

"Is it possible to design and fabricate a graphene-based differential pressure sensor using the transfer-free approach?"

Once the device is fabricated, the performance of the device will be compared with the state of the art in graphene-based pressure sensors and further characterization will be done to see if the inte-

gration of transfer-free process into bulk micromachining has any impacts on graphene.

1.2. Research Goals

In order to achieve the problem statements, the complete research work has been divided into individual research goals. Each research goal has been assigned a separate chapter individually.

1. Perform a background literature review to analyze the feasibility of transfer-free graphene based pressure sensors.
2. Build a valid simulation model for the device and conclude on the design parameters.
3. Translate the design parameters into mask design, build the process flow and fabricate the device.
4. Characterize the device through Raman Spectroscopy, build the pressure measurement setup, perform static and dynamic electrical measurements.
5. Also, further extend the work to investigate the feasibility of having free-standing transfer-free graphene membranes and employ it as a pressure sensor.

1.3. Thesis Outlook

This work will employ the novel tranfer-free approach developed by Sten Vollebregt to realize graphene-based pressure sensors. All the other aspects of this research work will revolve around this central concept. In the below section, the outlook of the thesis will be discussed.

- Chapter 2 - Literature Overview: In this chapter a background literature review was performed to analyze the feasibility of having transfer-free graphene-based pressure sensors. A literature analysis was performed on properties of graphene, characterization of graphene, use of graphene for pressure sensing and the state of the art in graphene-based pressure sensors.
- Chapter 3 - Design and Simulation: This chapter involves the validation of theoretical calculations on to a simulation platform, simulation of the state of the art, concluding on design parameters from results of the simulations.
- Chapter 4 - Mask Design and Process Flow: The design parameters derived from Chapter 3 are translated into mask designs. Later using these masks, a process flow is defined to achieve the devices.
- Chapter 5 - Device Characterization: This involves Raman spectroscopy of the devices, static and pressure dependent electrical measurements, and other device performance analysis.
- Chapter 6 - Conclusion - This chapter gives a complete overview on the thesis. The problem statements resolved and the research goals achieved will be discussed.

2

Literature Overview

Pressure, physically is the force per unit area applied along the normal of a surface.

2.1. A rewind to the past

The early methods to measure atmospheric pressure was developed during the late 16th century. Gasparo Berti, in his quest to prove the existence of vacuum, created one of the first barometers. A barometer consists of a simple inverted tube filled with water and the tube is placed inside a reservoir filled with water. He observed that when the tube was opened from one end, some of the water poured into the reservoir and after a while, the water level in the tube stabilized. This made him to conclude that the pressure exerted by atmospheric air made sure that the water level in the tube didn't fall beyond a particular point. Till then, people believed that air had no mass and hence could not exert any pressure. Berti's experiment proved them wrong. The later models used mercury instead of water as it was more dense and this allowed them to have compact tubes. Blaise Pascal took one of these tubes up a mountain and he observed that the levels in mercury dropped further than at sea level. This made him to conclude that the atmospheric pressure of earth decreases with altitude.
As time passed on, these systems have undergone a process of modification. We saw devices like manometers, McLeod gauges and Bourdon gauges to name a few, that made the measurement of pressure more reliable and accurate. The application of pressure measurement is very extensive. The principal of pressure measurement is used in systems like Altimeters, Barometers, Pitot tubes and Sphygmomanometer.

2.2. The Modern Pressure Sensors

The term sensor refers to a device that detects changes in the environment and represent the change in terms of a known quantity or a signal. Though historically, there were devices to measure the changes in the environment, they never made use of electricity. Credit has to be given to James Maxwell and his equations, which enabled the use of electric signals for devices. The advantages electrical signals offered were quite evident. They could be post processed easily, and also could be effectively transmitted over relatively large distances.

Evolution is the rule of nature, and so, we saw modernization in terms of sensors too. New materials, new signal processing techniques enabled accurate and reproducible sensor measurements. However, the most significant revolution was led by discovery of Silicon as a semiconductor. A semicon-

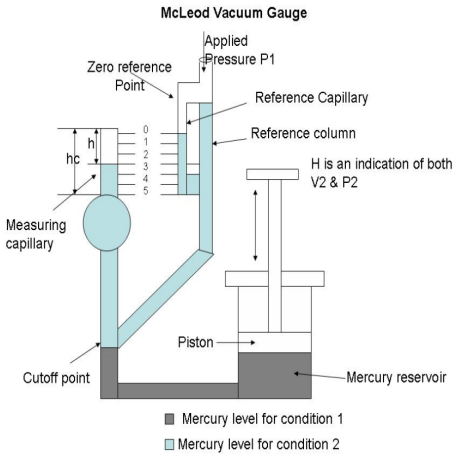

Figure 2.1: A McLeoad Gauge, teken from [12].

ductor is a material whose conductivity is in between an insulator and a metal. The first transistors, developed in the 1950s, paved way to newer, faster and efficient electronic circuits. This revolution led to a development of a whole industry related to semiconductor processing and manufacturing. Devices kept getting smaller and smaller, while their efficiency and performance went up. However, by using the machinery and materials of the semiconductor industry, researchers made new devices that could sense changes in the environment and output a corresponding electrical signal. Later, this area of semiconductor processing was called as *Micro Electro-Mechanical Systems* or as *Semiconductor Micro-machining*.

The earliest semiconductor based pressure sensor was developed by Smith et al., in 1952 [13]. This was technically a piezoresistive strain gauge, which when loaded by a pressure, underwent a change in its resistance. The was one of the first efforts to develop MEMS pressure sensors using piezoresistive single crystal silicon. Later, there were many significant developments in this regards and many physical properties have been explored to measure pressure. In the next section, some of the different transduction methods for pressure sensing will be discussed.

2.2.1. Thermal Conductivity based Pressure Measurements

When the density of a gaseous medium increases, it's pressure also increases and hence the ability to conduct heat also increases. In this method, a filament is heated by passing current through it and a temperature sensor is used to measure the temperature of the filament. The rate at which the filament loses the heat to surrounding air is directly proportional to the thermal conductivity of air and hence the pressure.

Pirani gauge is one of the example for this. Here, a conductive filament is exposed to the media whose pressure is to be measured. The filament is heated by current passing through it and is subsequently cooled by the surrounding media. If the pressure of the system is reduced, the thermal conductivity of the surrounding media decreases and the rate at which the filament loses heat also decreases. As the resistance of the wire is a function of temperature, by measuring the resistance, the pressure around the filament can be evaluated.

2.2.2. Ionization Gauge

Here, the gas atoms are subjected to high energy electrons and this causes the atoms to get ionized. The number of ions so produced will be directly proportional to the density of the gaseous medium.

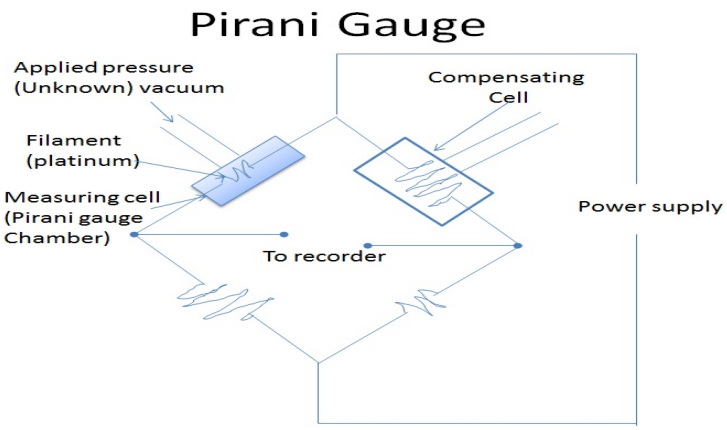

Figure 2.2: A Pirani Gauge, from reference[14].

However, the generation of ions depends on the type of gas in the media. Also, this is suitable for pressures in the range of 10^{-9} to 10^{-1} Pa.

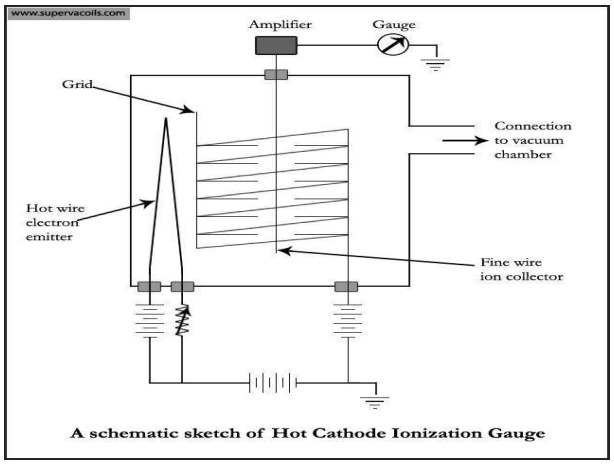

Figure 2.3: An Ionisation Gauge, from reference[15].

Electrons, after they collide with the gas atoms, generate positive ions. The ions can be collected by a suitably biased terminal. The current collected by the terminal is proportional to the rate of ionisation which in turn is proportional to the density of the gaseous medium. Hence, the terminal current can be calibrated as a function of pressure.

2.2.3. Membrane Based Pressure Sensors

Here, the sensing element consists of a membrane on which the pressure is applied. Due to the applied pressure, the membrane undergoes deformation and also, this induces strain. Based on the type of the material, multiple read out schemes like piezoresistive, capacitive or optical can be employed.

In the upcoming section, membrane based pressure sensing will be discussed in detail.

2.2.4. Overview of Membrane Based Pressure Sensors

Membrane based pressure sensors are suitable for relatively higher pressure ranges and are also suitable with MEMS processing. The sensors can be further classified on the basis of the read-out

schemes like piezoresistive, optical or capacitive. They are explained the section below

Piezoresistive

These work on the principle of piezoresistance, where the resistance of the membrane changes as a function of the applied pressure. Due to the applied pressure, the membrane undergoes deformation and also, this induces strain in the membrane. By virtue, piezoresistance being a native property to certain materials, due to the strain in the membrane, the resistance changes. This change when measured will correspond to the change in the applied pressure. See figure 2.4.

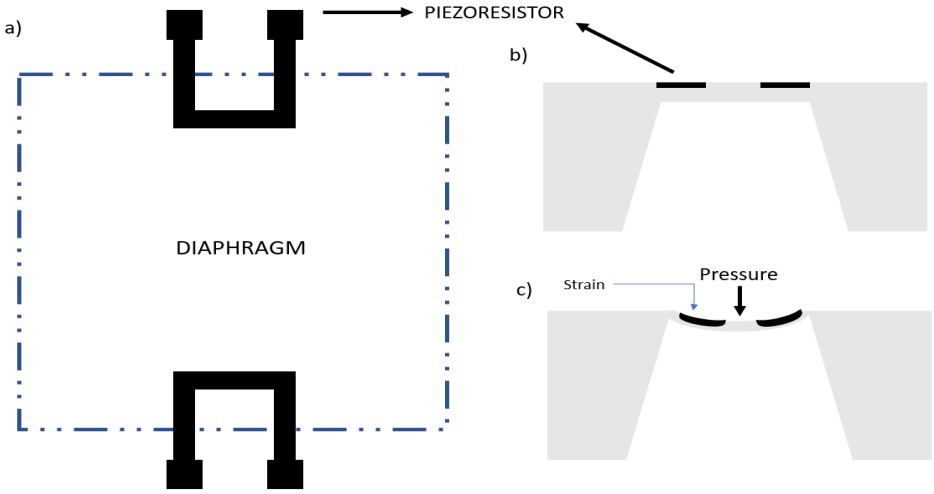

Figure 2.4: A piezoresistive Si based pressure sensor.

In the figure 2.4, the suspended membrane and the piezoresistors can be seen.

Capacitive

The membrane on which the pressure is applied is one of the plates of a parallel plate capacitor. Due to the applied load, there is a deflection in the membrane, which results in reduction of separation between the terminals of the capacitor. This changes the capacitance as a function of the applied pressure [16].
Here, the suspended membranes acts as one of the terminal of the capacitor. Any change in the distance between them will result in a change in the capacitance.

Optical

In a Fabry-Perot cavity based pressure sensor, the incident light will reflect back from a membrane that is loaded by the pressure. The reflected light is then fed into a receiver where a phase difference between the incident and reflected wave is calculated. This is proportional to the applied pressure [17].

Not only the physics, the materials behind the devices also can be varied. Each material is associated with different properties and also react with the environment differently. Hence, choice has to be made in terms of physics and materials when designing a MEMS pressure sensor.

After an extensive literature overview on MEMS based pressure sensors, a choice was made to pursue membrane based piezoresistive pressure sensors. This will be discussed in detail in the following section.

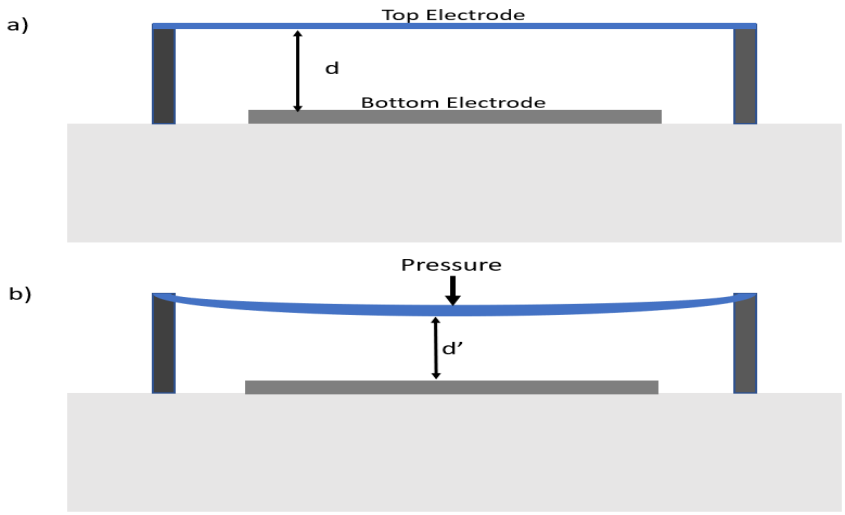

Figure 2.5: Capacitive Pressure Sensing. The distance between the electrodes d' decreases as the membrane bends due to the applied pressure.

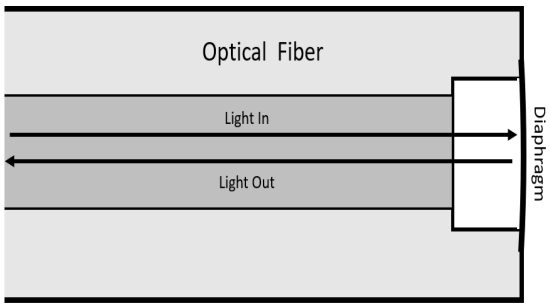

Figure 2.6: A Fabry-Perot cavity based pressure sensor

.

2.3. Piezoresistive MEMS Pressure Sensors

Piezoresistance is a property of a material when under strain, it undergoes a change in it's resistance. The strain is due to an external load applied on the membrane.

2.3.1. Piezoresistance in Metals

Piezoresistance in metals is highly influenced by the change in geometry due to an applied load. For a metal, we know resistivity can be defined by the equation,

$$R = \rho \frac{l}{A} \tag{2.1}$$

Where R is the resistance, ρ is the resistivity, l is the length and A is the area.
Also, the Gauge Factor (G.F) is given by

$$GF = \frac{\Delta R/R}{\epsilon} \tag{2.2}$$

Gauge Factor is the measure of normalized change in resistance to strain.

The corresponding change in resistance is [18],

$$\frac{\Delta R}{R} = (1+2\nu)\epsilon + \frac{\Delta\rho}{\rho} \tag{2.3}$$

where ν is the Poisson's ratio, ϵ is the Young's Modulus and $\Delta\rho$ is the change in resistivity due to strain.

In the equation 2.3, the first term is due to the change in geometry while the second term is due to change in resistivity due to strain. In metals, the contribution of the geometric term is very high in comparison to the change in resistivity due to strain and hence, this can be ignored.

2.3.2. Piezoresistance in Semiconductors.

In case of semiconductors like Silicon, the equation 2.3 holds true. However, the change in resistivity due to strain is around 100 times higher in magnitude than in metals [18] and also greater than variation due to change in geometry.

The change in resistivity can be due to the change in the band-gap against an applied strain. This was observed by Smith et al [19]. In a similar work by J Bardeen et al.[20], it was noted that the application of strain influences the carrier mobilities and hence their effective masses which in turn change the resistivity.

Also, the magnitude of piezoresistance is also dependent on the orientation of the semiconductor crystal and the direction of the force applied.

2.3.3. Piezoresistance in Graphene.

Even though graphene is a conductor, it's piezoresistivity is very different from that of metals. Like in semiconductors, in addition to geometric variation of resistance, there is a very high influence from the non geometric variation due to strain on the change in resisitance.

In the study by A.D Smith et al. [3], they observed that Fermi Velocity(V_f) of electrons decreases with increase in strain. Also, the mobility of the electrons can be expressed as below

$$\mu_e(\epsilon) \sim v_f(\epsilon)^4 \tag{2.4}$$

Where ϵ in the strain, μ_e is the mobility of electrons.

Resistivity can be expressed as

$$\rho = \frac{1}{qN_e\mu_e} \tag{2.5}$$

Where ρ is the resistivity, N_e is the electron density and q is the charge. From this we get a relation between resistivity and fermi velocity. So, if the strain in the graphene film increase, it's fermi velocity goes down and hence the resistivity increases.Also, the type of graphene, the orientation of graphene will have a considerable amount of influence on the piezoresistance.

The effect of grain boundaries and it's relation with piezoresistnce has been also been researched. Generally, graphene is polycrystalline with crystals arranged as grains. Due to the application of strain, there is elongation of the grain boundaries, and the grains may get seprated. This restricts the conductive pathways that are used by electrons and the electrons are forced to take longer pathways. Hence, there is an increase in the resistance [21].

2.3.4. Overview on Membrane-based Piezoresistive Pressure Sensors

A semiconductor based piezoresistive pressure sensor consists of a membrane or a diaphragm which acts as a piezoresisitor on its own, or acts as a support layer on which piezoresistors are formed. The work by Smith et al. [13], uses a silicon based bulk micromachined diaphragm, on which piezoresistors are deposited. When the membrane is loaded by a differential pressure, a strain is induced in the piezoresistors and this forces a change in its resistance.

As mentioned earlier, it is possible to use a number of materials as the piezoresistor. Doped Silicon, doped SiC, graphene or any other material that is piezoresistive can be used as piezoresistors. However, in cases where the piezoresitive material is extremely delicate, like graphene or MoS_2, thin dielectrics that provide a structural support platform for the piezoresitors are needed. SiO_2 or Si_3N_4 can be used for this purpose. In the upcoming section, the material choices for the structural layer and for piezoresistors will be discussed in detail.

2.4. Materials for Structural Support Layer

As discussed in the previous section, based on the choice of the piezoresistor, there might be a need for a structural support membrane for the piezoresistor. In this section, we will look at various materials that might be suitable candidates for this purpose. In these cases, the mechanical property, and hence the geometric dependence of gauge factor (equation 2.3) will be dominated by the structural support membrane.

2.4.1. Silicon

Silicon is a semiconductor with a bandgap of 1,12 eV. Silicon can be classified into monocrystalline, polycrystalline and amorphous. Monocrystalline Si is SP_3 hybridized with a tetrahedron geometry. Silicon is the first material to be used as a diaphragm for pressure sensors. The advantage Silicon offers is the ease in processing. Silicon can be etched in both wet and dry methods. However, in the recent years, materials which offered better mechanical properties have been opted for the structural layer. For MEMS processing, it is preferred to use monocrystalline Silicon. The below table outlines the mechanical properties of monocrystalline silicon.

Table 2.1: Properties of Silicon [22]

Properties	Value
Poissons's Ratio	0.265
Young's Modulus(GPa)	140

2.4.2. Silicon-Oxide

Silicon Oxide is one of the most abundant materials on this planet. It is the most common constituent of sand and is the major source for pure Silicon. Silicon-oxide is an insulator and is mainly used as gate oxide. However, since the development of MEMS processing and technology, Silicon oxide is used in various capacities. Native silicon can be oxidised to form Silicon-oxide either by wet or dry processing. Dry oxidation is usually slower, but is much denser. Also, oxide can be deposited through LPCVD or PECVD processes. In surface micromachining, Silicon-oxide is used as a sacrificial layer and is wet etched in Hexa-flourine. Through the modern IC processing, it is also possible to have suspended Silicon-oxide membranes of roughly 100 nm in thickness.

Table 2.2: Properties of Silicon-oxide [23]

Properties	Value
Poissons's Ratio	0.15
Young's Modulus(GPa)	66

2.4.3. Silicon Nitride

Silicon Nitride has very useful properties. It's resistance to thermal shock, mechanical wear has made it to be used as a mechanical support or structural layer in many applications. Also, being electrically neutral, it has been used as an isolating layer between conducting elements. Generally, Si_3N_4 is resistant to wet etching and hence is not often used as a sacrificial layer. It is possible to deposit thin layers (100nm) of LPCVD SiN_X with minimal stress. This would be an ideal material to be used as a structural layer as it is very strong, while being relatively thin.

Table 2.3: Properties of Silicon-nitride [24]

Properties	Value
Poissons's Ratio	0.23
Young's Modulus(GPa)	166

2.4.4. Silicon-Carbide

Silicon-carbide or SiC is one of the hardest materials on the planet. SiC can exist in both amorphous and crystalline forms. SiC exists in more than 200 crystalline forms, but major types of SiC are:

- 3C-SiC
- 4H-SiC
- 6H-SiC

While amorphous SiC is an insulator, crystalline SiC is a wide-bandgap semiconductor. SiC is stable up to temperatures of 1500°C and hence is mainly used for high temperature, high volatage and fast switching applications. The conductivity of SiC can be varied by doping with n or p type materials. It has also been used in LED's, heating filaments, etc.

SiC has been investigated heavily for MEMS devices and applications. Its high stability, relatively high strength and inertness has offered great advantages for MEMS devices. Undoped SiC can be used as a diaphragm for piezoresistive based pressure sensors. Thin layers of approximately 200 nm can be deposited through an LPCVD or PECVD techniques. In the table, 2.4 are the properties of SiC.

Table 2.4: Properties of Silicon-carbide[25]

Properties	Value
Poissons's Ratio	0.35
Young's Modulus(GPa)	90

2.4.5. Materials for Piezoresistors

A number of materials can be used as piezoresistors. Metals and semiconductors are piezoresistive and when strained, they undergo change in their resistance. However, not all metals are compatible with IC processing. Since semiconductor based piezoresistors have a gauge factor that is very high than metals(owing to nonliner change in resistivity due to strain), modern piezoresisitive pressure sensors make use of doped Si or SiC as piezoresistors.

In our model, we are exploring graphene-based piezoresistors, which theoretically have a higher piezoresistive effect than semiconductors [26]. In the following sections, the properties of graphene, synthesis and characterization will be discussed.

2.5. Graphene

Graphene is an allotrope of Carbon. The name is very similar to graphite, which too is a Carbon allotrope. Graphite can be decomposed into multiple individual layers. These individual layers when isolated, can be called as graphene. Graphene has six sp_2 hybridised carbon atoms forming a hexagonal structure. Each carbon atom has four bonds, three sigma, σ bonds along the plane and one pi bond, in the perpendicular plane respectively. The atoms in the π bonds form a cloud of electrons that encircle the carbon chain. This cloud is responsible for excellent electrical properties of graphene.

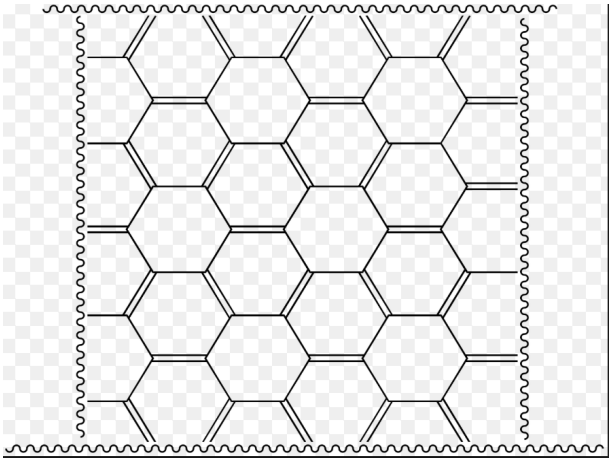

Figure 2.7: The hexagon lattice of Carbon atoms in graphene, taken from [27]

2.5.1. Graphene: As a MEMS material

Graphene is a novel material with many remarkable qualities to its name. At one atom thick, it is the thinnest material ever known and with an intrensic strength of 42 Nm^{-1}, it is the strongest ever to be measured. The charge carriers in graphene exhibit very high intrinsic mobility with negligible effective mass and at room temperature, they can travel without scattering. In comparison to metals like Copper, graphene can handle current densities upto five magnitudes higher, and has a high thermal conductivity of $5.30 * 10^3$ W/mK, [28].It has other properties like transparency, high stiffness and also, it is impermeable to gases.

Owing to it's structure, graphene has exhibited superlative properties in many domains. Graphene can be cited as a semiconductor with zero bandage, i.e the valence and the conduction band overlap each other at dirac points. Graphene also has a very high electron mobility, which is reported to be around 15000 cm^2V^11 [29]. The other interesting aspect of the charge carriers is that the hole and the electron mobility are nearly identical. This is in contrast to semiconductors like silicon, where

there is a credible difference is the mobilities.

Some researchers claim graphene to be the strongest material ever to be tested, with Young's modulus if 1 TPa and intrinsic tensile strength of 130 GPa. In comparison, Silicon has a Young's modulus of 169 GPa in (110) direction. To illustrate this, we can imagine a single crystal graphene hammock weighing 0.77 mg on which we can balance a 4 kg cat. Chemically, graphene is the only solid material in which all atoms can take part in a reaction. This makes graphene to be used for chemical sensing applications.

However, graphene is not perfect. Many research works have shown that graphene to to very brittle too. It has a fracture toughness of 4 MPa$\sqrt{m}$. In contrast, metals have a fracture toughness of 15–50 MPa$\sqrt{m}$ [30]. This is due to the lattice defects in graphene which lead to structurally weak points and act as carriers for deformation due to fatigue.

Using graphene as a material for MEMS has expanded the reach and the capacity of the technology. Graphene has further enabled the doors to realize a new range of devices with high sensitivity, lower power consumption and based on applications, high selectivity too.

2.5.2. Types of Graphene

Graphene can be categorized on the basis of its structure. In terms of dimension, graphene can be categorized as a 2D material where as carbon nanotube is categorized as 1D and fullerene as 0D material. Coming to graphene layers, thay are further categorized on the basis of it's constituent layers. They are:

- Mono-layer Graphene
- Bi-layer Graphene
- Few-layer Graphene
- Multi-layer Graphene

Mono-layer Graphene

This constitutes of a single layer of hexagonally arranged C-C atoms. Hence, the layer is only one atom thick.

Bi-layer Graphene

This is made of two mono layers of graphene. The thickness is around 1nm.

Few-layer Graphene

Multi-layer graphene is made up of anywhere from two to ten mono layers. The thickness is greater than 2 nm and lesser than 10 nm.

Multi-layer Graphene

Here, there are more than 10 constituent layers and the thickness is greater than 10 nm. However, if the number of layers increase further, the material will move closer towards graphite.

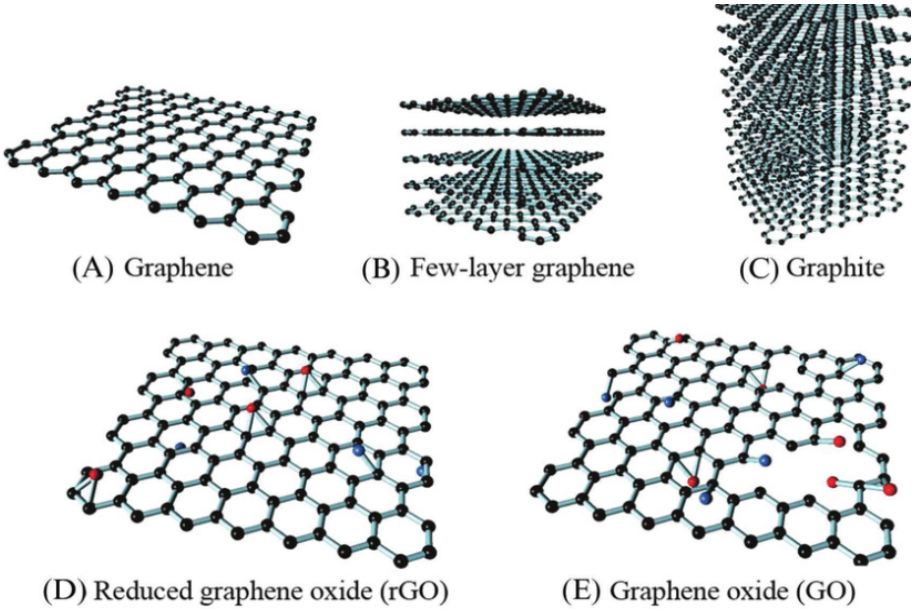

Figure 2.8: Graphene Allotropes, taken from [31].

2.5.3. Properties of Graphene

The properties of graphene will vary depending on its constituent layers. While most of the works in the literature are mainly focused on mono-layer graphene, only limited data is available with regards to bi or multi-layered graphene. However, by comparing the properties of mono-layer graphene to bulk graphite, we can get an idea on the trends of the deviation in properties between the two. In the table 2.5 are the properties of mono-layer graphene.

Table 2.5: Properties of Graphene

Properties	Value
Electron Mobility (Theoretical) [29]	200,000 cm^2/Vůs
Electron Mobility (Experimental) [29]	15000 cm^2/Vůs
Electrical Conductivity [32]	2700 S/cm
Sheet Resistance [33]	700 to 1700 Ω/sq
Opacity [34]	2.3%
Poissons's Ratio [35]	0.19 to 0.46
Young's Modulus(GPa) [35]	500 to 1500
Ultimate Tensile Strength(GPa) [36]	150

2.6. Characterization of Graphene

Graphene is a very thin material and it is very hard to characterize is without having specific tools. Since graphene is optically transparent, it is difficult to confirm it's presence trough optical observations. Raman spectroscopy is one of the tools that can be used to characterize graphene and the same is explained in the subsection below.

2.6.1. Raman Spectroscopy

Raman spectroscopy, named after C.V Raman, is based on Raman Scattering. When a monochromatic radiation is incident on matter, the photons are scattered either elastically or non elastically.

The non elastic photons with less energy than incident photons are called as Raman scattered photons.
In Raman spectroscopy, a monochromatic light source is used to excite the matter. The light interacts with molecular vibrations (phonons) which causes the energy of the incident photons to shift. The shift in energy is dependent on the vibrational modes of the matter under test. By studying the energy shifts, the composition of the material can be estimated

2.6.2. Raman Spectroscopy of Graphene

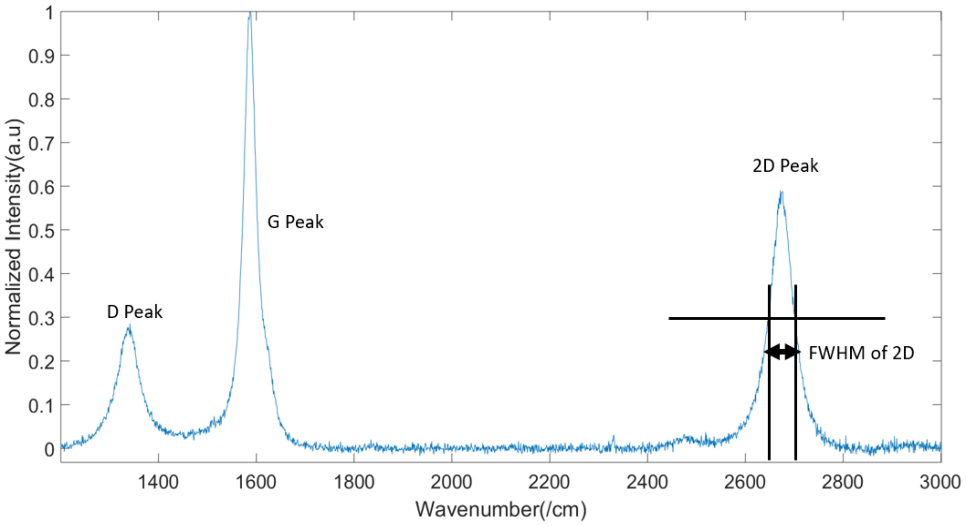

Figure 2.9: Raman Spectroscopy of Graphene.

When a layer of graphene is subjected to Raman spectroscopy, three distinct peaks can be observed. *G peak* at 1580cm $^{-1}$ represents the primary in-plane vibration of the hexagonal lattice atoms. This peak is an indication of the presence of hexagonal Carbon atoms. The D peak at 1350 cm^{-1}, may not be necessarily be seen in a graphene membrane with no defects. This represents the different in plane vibrations and this is due to the deviation from the hexagonal lattice structure. The deviation could be due to atomic defects or structural defects like wrinkles. The double resonance of Raman scattering gives rise to the 2D peak seen at 2690 cm^{-1}[37]. 2D peak will be present in the Raman spectra of graphene even in the absence of the D-peak. This is shown in the figure 2.9.

The spectrum undergoes a change if the number of layers of graphene increases. The 2D peak splits into multiple modes and when combined, increases the width of the 2D peak. When the number of layers increase, the 2D peak gets reduced in intensity, however, gets wider in comparison to monolayer graphene. Also, the reduction in intensity for the 2D peak will get saturated as the layers get increased [38].

For few layers of graphene (less than 5), the number of layers can be estimated by comparing the ratio of intensities of 2D and G peaks, i.e I_{2D}/I_D. I_{2D}/I_G has a value greater than 1 for FLG (few-layer graphene) and has a value lesser than 1 for multi-layer graphene [39]. Howevever, as the number of layers increase, the intensity of the 2D peak (I_{2D}) decreases and becomes saturated beyond a certain number of layers and hence, multi-layer graphene cannot be characterized using I_{2D}/I_G. However, in the work by Y. Hao et al., it was observed that the Full width at half maximum of the I_{2D} peak increases with increase in the number of layers [40]. Hence, the width of the 2D peak increases for

increase in the number of layers. Hence, *FHWM* of I_{2D} can be used to predict the number of layers in multi-layer graphene (more than 10 layers).

In a zero defect graphene membrane, the D peak should be non existant. However, it is next to impossible to achieve a defect-free graphene membrane. For the D peak to be visible, a charge carrier must be scattered by an incident photon followed by an elastic scattering by the defect in the lattice that forces the charge carrier to recombine. For example, an electron must be in-elastically scattered by an incident photon and then scattered elastically by the defects in the lattice. This caused the electron-hole pair to recombine. The ratio of intensities of the D peak to the G peak is used to estimate the defects in the graphene membrane. The trends in value of I_d/I_g can be analysed as follows. Initally, for low defects, the ratio I_d/I_g will increase for increase in defects due to elastic scattering. However, after a certain high-defect value, I_d/I_g will decrease accompanied by attenuation of all the peaks. This happens when the structure is similar to amorphous Carbon.

2.7. CVD growth of Graphene

Graphene is not readily available in nature. Hence, it has to be produced artificially. The early methods involved mechanical exfoliation of graphite. Here, graphite was mechanically separated until a single layer of graphene was got. In the later years, graphene was produced by reduction of graphite oxide. Recenltly, graphene has been produced through a Chemical Vapor Deposition process, where graphene layers are formed as bi-products of chemical reactions. This method is cost effective and the quality of graphene sheets are reasonably good.

The growth of graphene through a chemical vapor deposition process is achieved through a catalyst which is generally a transition metal. Transition metals are those with partially filled D orbitals. Metals like Rhuthenium (Ru), Nickel (Ni), Molybdenum (Mo) or Copper (Cu) can be used as catalysts. The formation of graphene and further growth occurs when these metals are exposed to hydrocarbons at high temperatures and low pressures. However, the kinetics behind the growth is dependent on the soulubility of Carbon in the transition metal. The cases are explained below.

2.7.1. Growth of graphene due to High Carbon Solubility.

Transition metals like Ni exhibit high Carbon solubility and hence the formation of graphene is influenced by it. The growth of graphene can be defined by two physical phenomena that occur between Carbon atoms and the transition metal. They are solubility and diffusion. Solubility is a process when a solute dissolves in a solvent. Here, Carbon atoms at temperatures above 900°C, become soluble in transition metals like Ni. Formation of steel, when Carbon dissolves in Iron, can be cited as an example. However, for interaction between Carbon and a transition metal, solubility becomes maximum at a specific temperature and pressure, and from there, solubility decreases with decrease in temperature. Diffusion is the movement of particles from a region of high concentration to a region of low concentration. Once the Carbon atoms get dissolved in the metal catalyst, they diffuse within the metal. Diffusion is a function of both concentration of Carbon atoms and the temperature. For graphene growth, a catalyst must be chosen on the basis of the type of graphene that needs to be grown and also, the type of substrate it must be integrated with.

When the catalyst in heated to temperatures of 1000°C, the hydrocarbons decompose to form Carbon and H_2 and the carbon atoms get dissolved in the metal catalyst. When the temperature is decreased, the solubility of Carbon in the catalyst reduces and some of the carbon atoms rise to the surface of the catalyst. These isolated islands of Carbon atoms form inter-atomic bonds and

form a hexagon structure. The hexagon structure can be seen as interleaving of two triangular lattices. Each atom in the hexagonal lattice has four bonds. Three in-plane σ bonds and one out of the plane π bond. Strong adhesion is seen between the substrate and the hexagonal lattice. This is attributed to the co-valent bonding between the π orbitals of graphene and the free electrons in the D orbital of the catalyst. As the solubility of Carbon decreases further, these islands converge to form poly-crystalline graphene. After the formation of the first layer, additional layers are added to the graphene mono-layer. The rate of growth depends on few variables like pressure, temperature and the rate of gas flow[41].

The below image (fig 2.10) represents the process flow of graphene formation on Ni substrate.

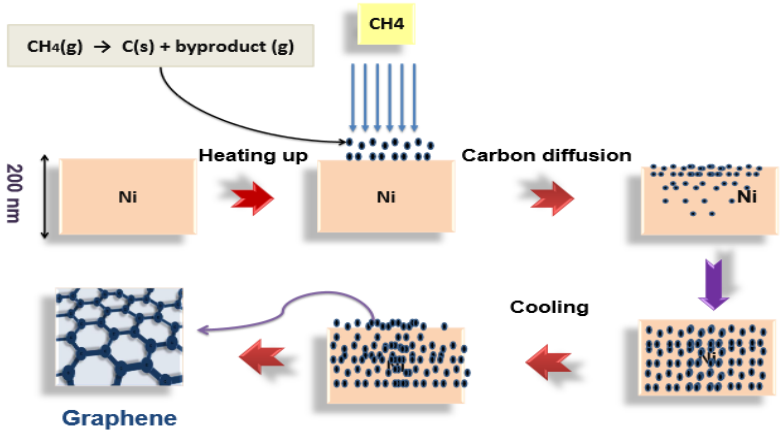

Figure 2.10: The growth of graphene on Ni catalyst, taken from [42].

2.7.2. Isothermal growth of graphene.

This phenomena is seen in transition metals with limited Carbon solubility like Cu. Here, the graphene growth occurs at a constant temperature rather than during the decrease in temperature for the case mentioned above.

When the catalyst is heated to around 950°C in the presence of Hydrocarbons, a thin layer of melted layer is formed at the surface of the catalyst. The hydrocarbon decomposes into hydrogen and Carbon at this temperature. The Carbon atoms start to converge on the meted layer, and when the concentration of Carbon is supersaturated, nucleation centers for graphene growth are formed. These centers act as grain boundaries or can also be points of defects.

A nucleation center gives rise to a small disc of Carbon atoms and these atoms prevent the further precipitation of the Carbon atoms into the molten metal layer. The Carbon atoms diffuse radially from these nucleation centers, giving rise to C-C structure. These discs cover the entire surface of the metal and the layer becomes thermodynamically stable.

Seen in the figure 2.11, ΔCu is the thickness of the molten Cu layer, N_d is the concentration of the Carbon atoms in the molten layer, D_{gr} is the diameter of the graphene ring and $\Delta\ I_{gr}$ is the separation between successive graphene rings in the molten layer[43].

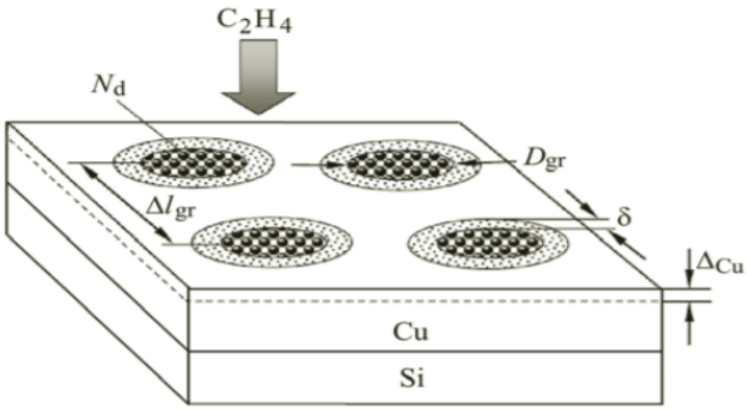

Figure 2.11: The growth of graphene on Cu catalyst, taken from [43]

2.8. Transfer Process of CVD Graphene

Most of the graphene based devices in the literature ([3],[1], [2]) make use of wafer to wafer transfer of CVD graphene.

In this process [44], a metal catalyst (generally Cu or Ni) is deposited on a Si wafer. Later, graphene is grown via a CVD process as mentioned in the earlier section 2.7. Later a polymer generlly PDMS (Polydimethylsiloxane) or PMMA (Ploy-methyl methacrylate) is spin coated on the wafer and is then cured. The wafer is now soaked in water and the polymer along with graphene and the metal peels away from the wafer. Then the metal is etched away in $FeCl_3$ solution. The polymer along with the graphene layer is now transferred to an actual substrate. The polymer is then dissolved using a polymer developer. The graphene membrane then lands on the substrate. This is shown in the figure 2.12.

2.8.1. Defects in Transferred CVD Graphene

Mechanically exfoliated flakes of graphene are generally single crystalline with no grain boundaries and therefore are thought to be more mechanically stable than CVD grown graphene. CVD-graphene iso-poly crystalline in nature with grain boundaries and defects which can act as centers for initiation of cracks when exposed to stress [45]. Hence, handling of CVD graphene is a delicte process, and there are chances of inducing damage to the membrane during the transfer process [2].

Also, the use of polymer during the transfer process is known to cause surface contamination of the graphene membrane [47]. Polymer residue might get absorbed by graphene and this might cause some changes to both the mechanical and electrical properties of the graphene membrane [9]. Further, strain induced on the graphene membrane during the transfer process might cause wrinkles in the membrane. These wrinkles might cause self heating in the membrane and can be a cause for device failure [48].As reported by Q. Wang et al. [2], the transfer process can also induce pin-holes in the graphene membrane and this could deteriorate the structural integrity of the membrane.

Hence, owing to these concerns, it would be ideal to avoid the transfer step completely. For graphene-based devices, it would be ideal to have graphene to be grown directly on the desired substrate. This process is reported by S. Vollebregt et al [11].

By streamlining graphene and semiconductor procssing together, devices with better reproducibility, better throughput, and scalability can be achieved. This is discussed in the succeeding section.

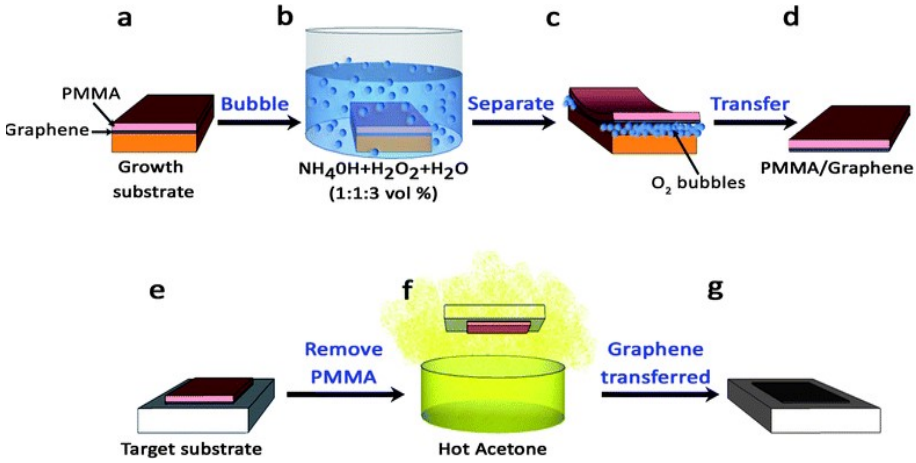

Figure 2.12: The various steps involved in the transferof CVD graphene, sourced from [46] .

2.9. Transfer-free Graphene Processing

To eliminate the evils of graphene transfer, we employ a transfer-free graphene processing method proposed by S. Vollebrebt et al [11]. The growth consists of two main steps. Firstly, the selection of a catalyst that is suitable for both cleanroom processing and graphene growth. This is followed by CVD growth of graphene on the catalyst. This has been briefly explained in the following subsections.

2.9.1. Selection of a Catalyst

To grow graphene through a CVD process, a catalyst on top of which gasesous product react to form graphene, is required. This has been researched heavily and many metals like Ru, Ir, Ni and Cu have been used for the purpose. Most of CVD grown graphene uses Cu as the catalyst. This method is suitable for transferred CVD graphene where graphene is transferred to another substrate after being grown. However, when it comes to wafer level manufacturing, that is, to grow graphene on a Si wafer, the use of Cu comes with a lot of drawbacks. Firstly, Cu is considered a contaminant in standard IC processing. Also, due to the variation in thermal expansion between Cu and Si wafer, strain is induced in Cu layer and so produced graphene will be wrinkled. Also, in most of the cases, graphene is grown at temperatures of more than 900°C, and this is close to the melting point of Cu. Hence, there are chances that Cu layer might get pitted during the process [49].

The work of Y. Grachova et al [49] focused on using different catalysts for graphene growth that could make wafer level fabrication of graphene feasible. Here, Mo was used as a catalyst. Mo has thermal expansion co-efficient that is very close to Si and hence chances of inducing strain in the Mo layer is reduced. The research used a 50 nm Mo layer as a catalyst and the resulting characterization of the graphene layer proved that Mo is a good substitute for Cu in wafer level graphene growth.

2.9.2. The Growth

The CVD of graphene using AIXTRON Black Magic Pro can be divided into the following steps. Initially, the Si wafer with Mo catalyst is brought to the temperature of 915°C in the presence of H_2 (1000 sccm) at 25 mbar of pressure.

The wafer is then annealed for 300 seconds. This is done to remove native metal oxide. Further, CH_4 is introduced in the chamber at 20 sccm. Hydrocarbons are unstable at this temperature and methane splits into Carbon and Hydrogen.

Then, Carbon atoms dissolve in Molybdenum and they further diffuse to form MoC_2. MoC_2 is the actual catalyst used in the formation of graphene. The chamber stays at this temperature for a specific amount of time and further, the chamber is cooled down slowly at the rate of 50°C/min. Here, the growth of graphene occurs due to isothermal process. As the temperature decreases, the solubility of C in Mo also decreases and hence, the diffused C atoms rise to the surface of the metal catalyst. These then form additional layers on the graphene layer on top. However, in this case, the growth is dominated by the isothermal process over solubility.

Over a period of slow cooling, the local islands of C-C atoms form larger crystals. After a complete growth cycle, a multi-layer graphene membrane is formed on top of the metal catalyst.

The 2p orbital of the C atoms form co-valent bonds with the 4d orbital of the Mo substrate. This explains the good adhesion between graphene and Mo. Later, Mo is etched away to release the graphene membranes.

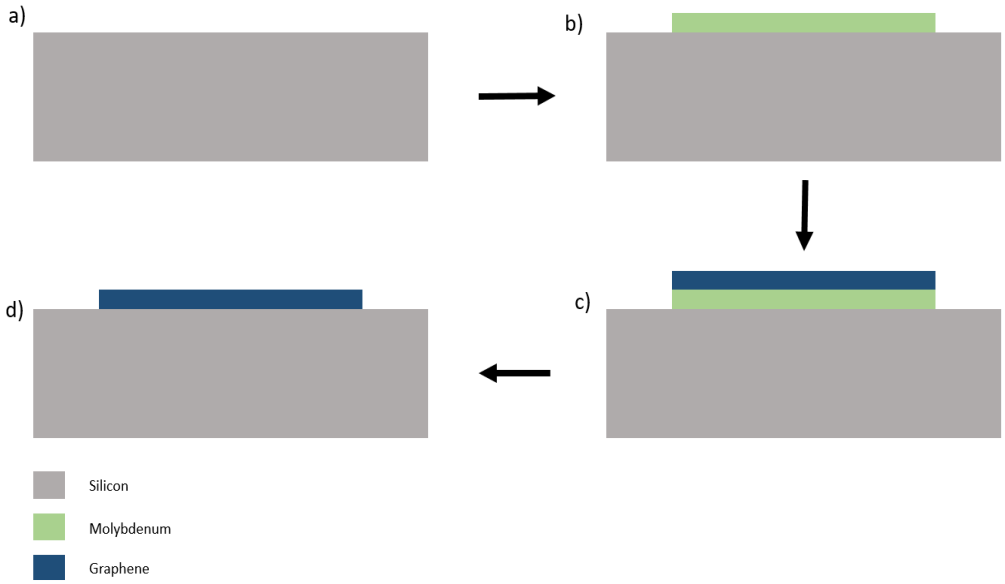

Figure 2.13: The various steps involved in transfer-free graphene processing .

2.10. Graphene based Pressure Sensors

2.10.1. Piezoresistance in Graphene

Many studies have been done in this regard and graphene has been proven to be an excellent piezresistive material. This makes graphene a good material choice to be used as a piezoresistor for pressure sensing applications. CVD Graphene has been reported to have piezoresistive guage factor somewhere in the region of 15000 [26].

In the study by X Zheng et al.,it was shown that the graphene type has an effect on piezoresistance. It was shown that the gauge factor of graphene decreased with increase in the number of layers. The study also focused on temperature coefficient of resistance of graphene and also, the change in

resistance due to the type of stress applied on the membrane [50]. The same in shown in the image 2.14.

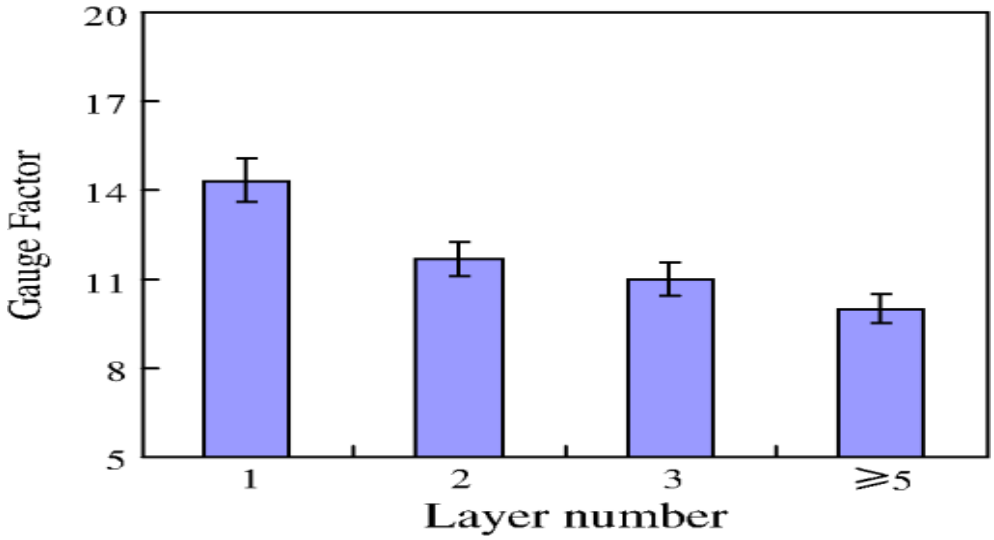

Figure 2.14: Variation in gauge factor as a function of graphene layers, taken from [50].

2.10.2. Graphene-based Piezoresistive Pressure Sensor: by S.E. Zhu et al.[1]

One of the early notable works in this regard was the research work of S. Zhu et al. This device was based on the piezoresistive effect of graphene. The sensor consisted of a 100 nm SiN_X supporting membrane on which meander shaped graphene resistors were transferred. The research work observed that the gauge factor of the device to be around 1.6 and had a sensing range from 0 to 700 mbar (70 kPa).

Through this work, it was shown that graphene based pressure sensors could offer performance that is comparable to metal based pressure sensors. In the figure2.15, the device and the final measurement results are shown.

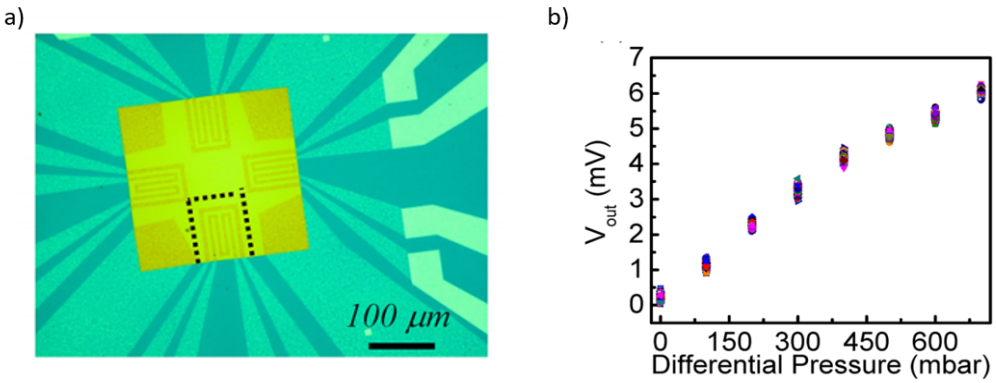

Figure 2.15: The final device b) The sensitivity measurements. Taken from [1]

2.10.3. Graphene "microdrums" on a freestanding perforated thin membrane for high sensitivity MEMS pressure sensors, work by Q Wang et al.[2]

, used graphene microdrums on a freestanding perforated SiN_X e membrane in their pressure sensor. The device consisted of a 490*490 μm^2, 200 nm thick SiN_X membrane, which was deposited through LPCVD on a silicon substrate. Later, 2.5 μm holes were patterned on this membrane. Graphene was grown using a CVD process and then transferred to the silicon substrate. The device had a gauge factor of 4.6 and had a sensitivity of 2.5* 10^{-5} $mbar^{-1}$.
The authors observed that the sensitivity of the device can be further increased by increasing the size of the suspended membrane, however, dimensions greater than 500 μm would weaken the membrane, thus increasing the chances of fracture. In the figure2.16, the final device and the measurement results are shown.

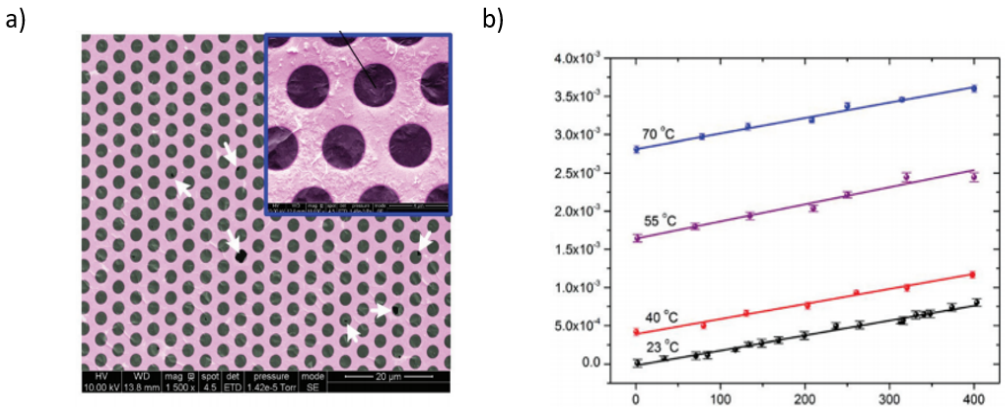

Figure 2.16: a) The final device b) The sensitivity measurements. Sourced from [2]

2.10.4. Electromechanical Piezoresistive Sensing in Suspended Graphene Membranes by A.D Smith et al.[3]

The works of A Smith et al. is also very substantial in the area of graphene based pressures sensors. In their work, they used free standing graphene membrane as the sensing element. The device was fabricated on p-doped silicon wafer which was then thermally oxidised to form a thin oxide layer on top. Then, circular and rectangular cavities were etched using reactive ion etching. Graphene was grown through a CVD process on copper foil. The graphene membrane was then transferred to the wafer using a polymer film as a transport vehicle. The measurement set up consisted of a wheat stone bridge network and the bride had the graphene membrane as one of the materials. The device had a gauge factor of 2.92. The sensitivity achieved was 3.95 uV/V/mmHg.

In this work, it was shown that piezoreisitive graphene sensors exhibited superior sensitivity in comparison to Silicon based sensors. The final device and the measurements can be seen in the figure 2.17

2.11. Conclusion

This chapter gave a background to pressure sensing and use of graphene for that purpose. Graphene has a high piezoresistance and combined with it's mechanical properties, it an ideal candidate for piezoresistive pressure sensors.

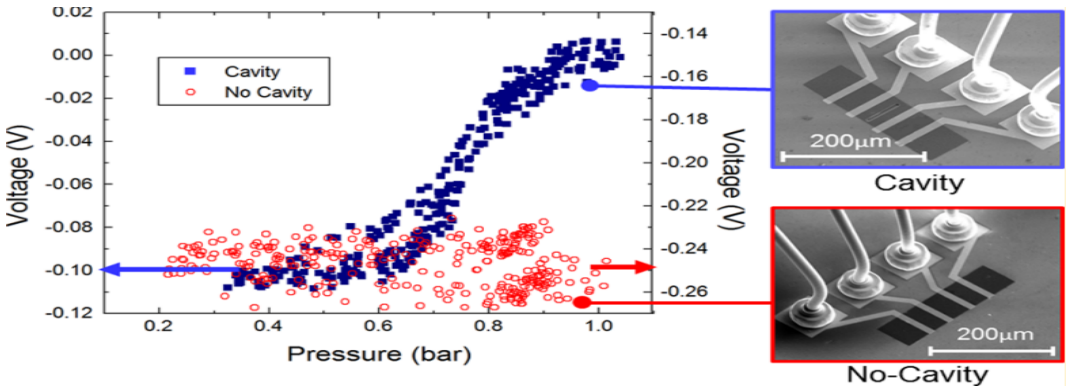

Figure 2.17: a) The sensitivity measurements b) The final Device. Sourced from [3].

Also, the transfer process of CVD graphene has some negative impacts on the graphene membrane. The polymer contamination can alter the properties of graphene and make them structurally weak [47]. The strain applied on graphene during the transfer process causes wrinkles on the surface of graphene [48]. These wrinkles are known to cause local heating in the membrane, which might lead to device failure. Transfer process of graphene can be considered as a bottleneck in increasing the scalability of graphene based devices.

It is certain from the literature that the use of Mo as a catalyst for graphene growth will result in fairly defect-free graphene while has no negative impact on the substrate.

By employing the transfer-free [11] graphene processing, graphene-based devices with high scalability factor and through-put can be achieved.

Hence, after an extensive literature search, it was devided to pursue transfer-free graphene membrane based piezoresistive pressure sensors.

3

Design and Simulation

After an extensive literature review, it was then decided to pursue the possibility of having a graphene membrane based differential pressure sensor. To start this Chapter, the theory behind the deflection of square membranes will be discussed, later followed by COMSOL Multiphysics simulations which further complimented the theory. These also aided in designing the test devices. Simulations were also performed to reproduce the results achieved by the current state of the art graphene membrane based pressure sensors. Further, conclusions were drawn from the simulations and the dimensions of the membrane were finalized.

3.1. Load Deflection of Square Membranes

The analytical solution to the out of plane deflection of a square membrane due to an applied load was reported by O Tabata et al. In their research work, they measured the deflection profile of a composite membrane as a function of the applied differential pressure. The relation is given by the equation [24],

$$p = C_1 \frac{t\sigma}{a^2}\delta + C_2(v)\frac{tE}{a^4}\delta^3; \tag{3.1}$$

Where, p is the differential pressure, C_1 and $C_2(v)$ are constants, t is the thickness, σ is the initial stress, a is the area, δ is the deflection, E is the Young's Modulus and v is the Poisson's ratio.

$C_2(v)$ can be expressed as

$$C_2(v) = \frac{C_2 * f(v)}{1-v} \tag{3.2}$$

Both C_1 and C_2 are dimensionless constants, derived from the geometry of the membrane. For a square membrane, C_1 is equal to 3.95 and C_2 is equal to 1.994 [51].Hence, if the parameters of the membrane are known, and for a differential pressure across the membrane, the out of plane deflection can be found out.

3.2. Overview on the State of the Art

Having looked at the literature, most of the current state of the art in this area make use of transferred graphene on to thin dielectric support membranes. S. Zhou et al. [1], and Q Wang et al. [2], have successfully fabricated pressure sensors with graphene membranes on top of SiN_X structural support membrane. With this aim in mind, firstly, we wanted to recreate the device environment on a simulation platform. The simulations were performed on *COMSOL Multiphysics*. After validating the results achieved in the literature through simulations, we further extended the model

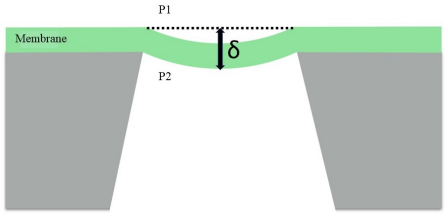

Figure 3.1: The deflection δ due to the difference in pressure P_1 and P_2

to design transfer-free graphene based (on a SiN_X support membrane) pressure sensors and free-standing transfer-free graphene based pressure sensors. Later, the parameters were finalized and comparisons were made with the state of the art.

3.2.1. Work by S.Zhou et al.

In this research work [1], SiN_X having a thickness of 100 nm , and a side length of 280 μm was used as a supporting membrane on top of which patterned graphene electrodes were transferred. Here, the mechanical properties are dominated by SiN_X. This is due to SiN_X layer being 100 nm thick and is much greater in thickness than the graphene electrode. Hence, in accordance with properties of the SiN_X membrane as mentioned in the literature, the simulation environment was set up.

Table 3.1: Device Properties, as in the literature [1]

Si_3N_4 Membrane	Value
Thickness (nm)	100
Length (μm)	280
Initial Stress(MPa)	50
C_1	3.45
C_2	1.994
Poissons's Ratio	0.22
Young's Modulus(GPa)	200

It can be seen in the image 3.2, that at a load of 70 kPa, the deflection is 7.9 μm and this matches with the value reported literature for the same applied pressure.

3.2.2. Work by Q Wang et al.

This research work [2] is also based on transferred graphene on a SiN_X support membrane, however, there are some minor differences. The thickness of the SiN_X membrane is 100 nm and the side length is 500 μm. Also, holes were etched in the SiN_X membrane over which graphene was transferred. These perforations in the SiN_X membrane formed local regions of strain in the overlaying graphene membrane. As mentioned in equation 2.2, greater strain in graphene corresponds to a higher Gauge Factor.

The composite membrane was simulated in *COMSOL Multiphysics* upto a differential pressure of 70 kPa. Due to meshing issues, the radius of the hole was increased to 8μm. As seen in the figure 3.3, but, the deviation from literature was very minimal. The membrane had a deflection of 14.1 μm at 40 kPa. This value matches to the one in the literature (14.1 μm) at the same load. The simulation results are shown in the figures 3.4 and 3.3.

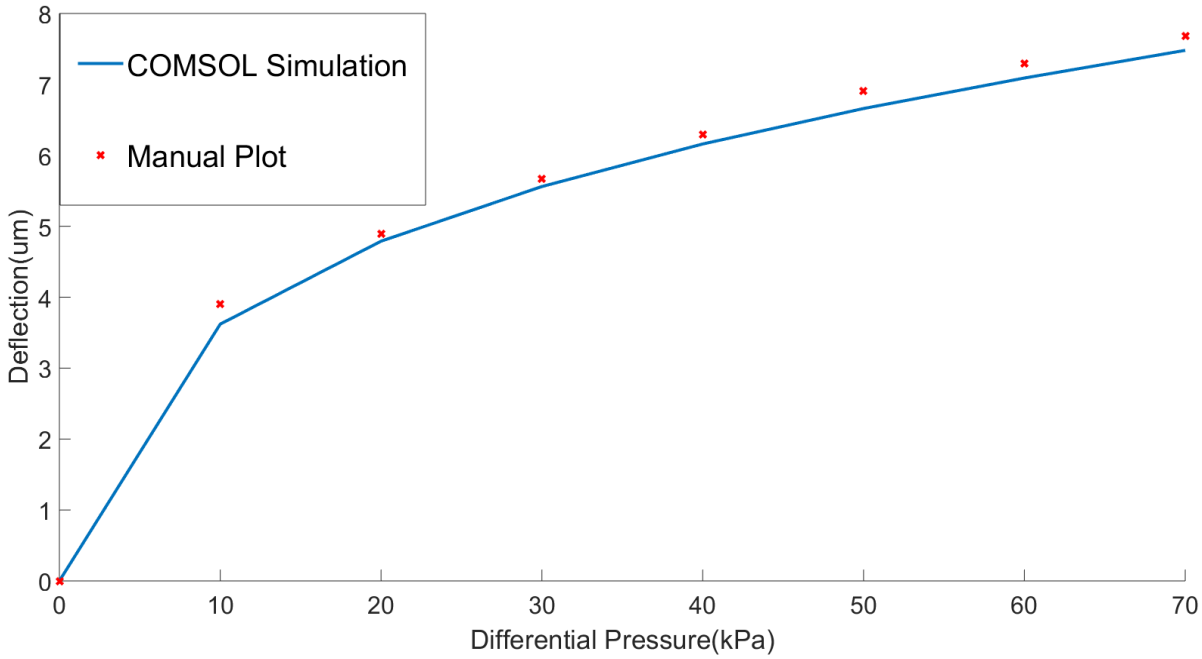

Figure 3.2: The deflection of the membrane as a function of applied pressure. Both simulation and manual values are plotted. The similarity between the two can be observed.

Table 3.2: Properties of perforated Si_3N_4 membrane [2]

Si_3N_4 Membrane	Value
Thickness (nm)	100
Length (μm)	500
Initial Stress(MPa)	50
C_1	3.45
C_2	1.994
Poissons's Ratio	0.22
Young's Modulus(GPa)	200
Hole Radius (μm)	2.5
Hole Periodicity (μm)	8

3.3. Transfer-free Graphene-based Differential Pressure Sensor

The simulations held true to theoretical analysis and from this, we could validate the simulation environment. As an initial aim, we decided to pursue a transfer-free graphene-based differential pressure sensor. Here, we are using a SiN_X as a support layer for graphene. Graphene will be grown via a CVD process on top of SiN_X thorough a transfer-free process [52].

From equation 3.1, we know that the deflection for a given pressure is directly proportional to the side length and inversely proportional to the thickness of the membrane, while all the remaining parameters are kept constant. Since SiN_X is a very well researched material, it's mechanical properties are known and are widely accepted. The table 3.3 lists the properties of SiN_X used in the simulation environment.

Keeping these properties in mind, simulations were performed by varying the design parameters. In the coming section, this will be explained in detail.

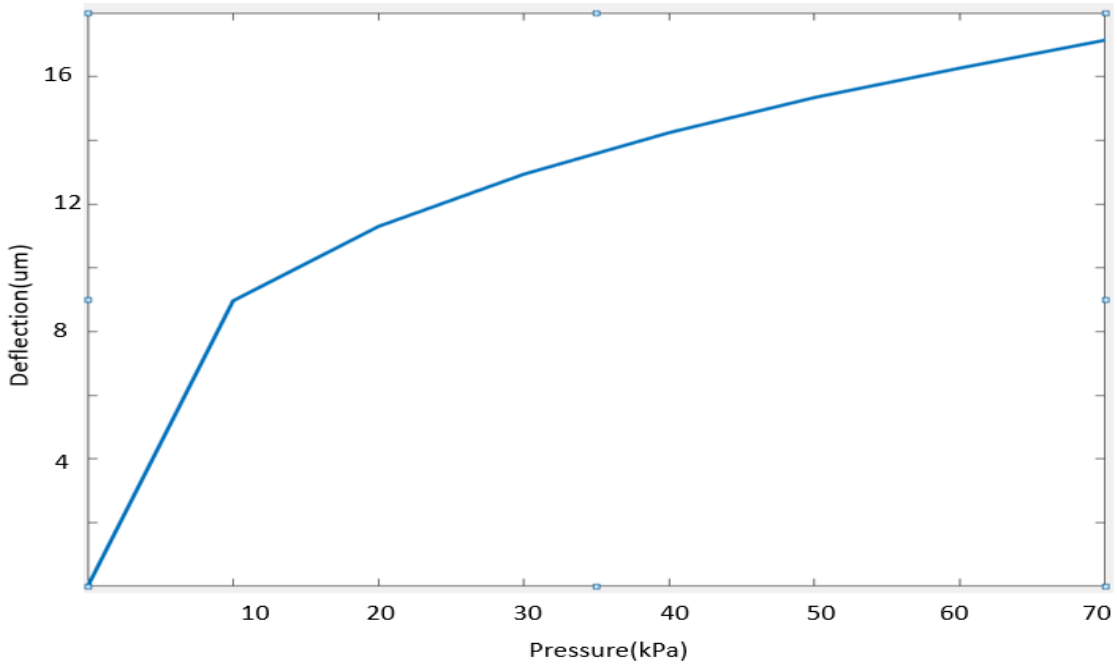

Figure 3.3: The deflection as a function of applied pressure, this is a recreation of the work by Q. Wang et al. The simualtio values match the values in the literature. [2]

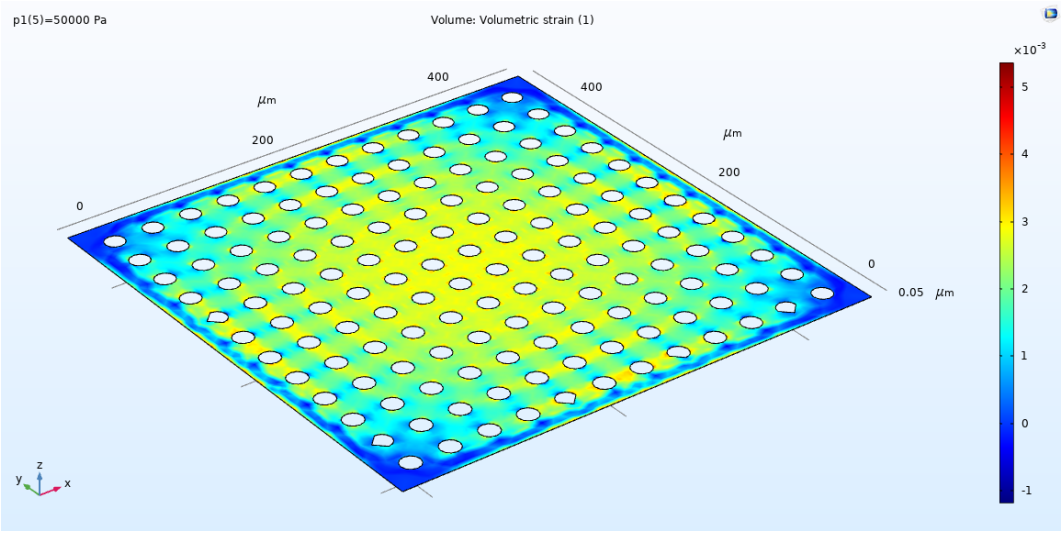

Figure 3.4: The volumeteric strain at an applied pressure of 50kPa. The value was equal to 0.00154. Recreated from reference. ([2])

Table 3.3: Properties of SiN_X used in the simulation model. The properties were referenced from [51].

Si_3N_4 Membrane	Value
C_1	3.45
C_2	1.994
Poissons's Ratio	0.22
Young's Modulus(GPa)	200

3.3.1. Side Length v/s Differential Pressure

The side length of the SiN_X membrane was varied from 200 μm to 600 μm in steps of 100 μm. The pressure applied was from 0 kPa to 70 kPa, increased at a step of 10 kPa. The properties of the simulation model are mentioned in the table 3.4.

Table 3.4: Simulation environment for varying side lengths.

Si_3N_4 Membrane	Value
Thickness	100 nm
Poissons's Ratio	0.22
Young's Modulus(GPa)	200

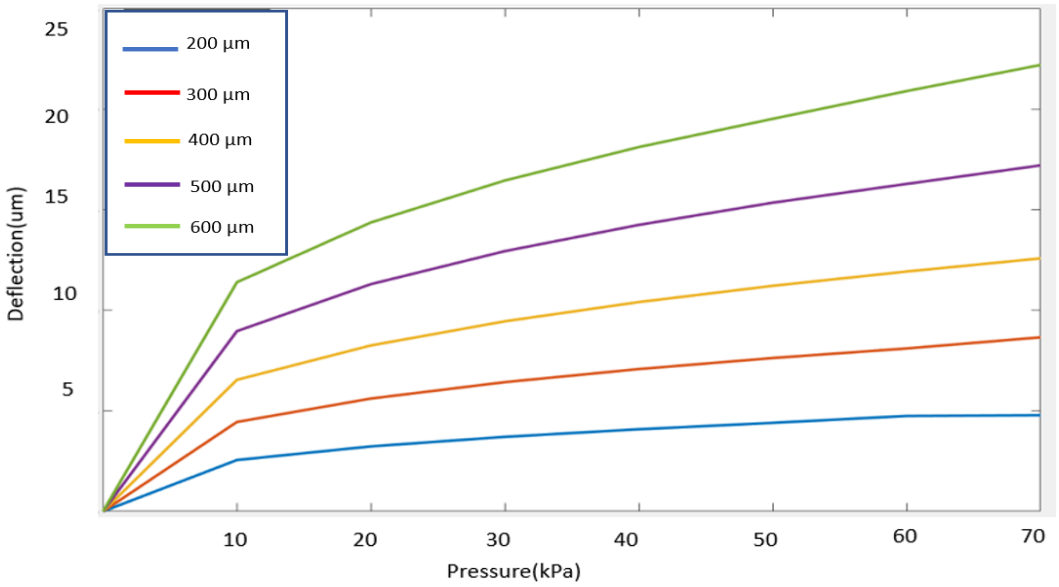

Figure 3.5: The variation in side length, versus differential pressure. The thickness of the membrane is 100 nm.

The membrane of side 600 μm has a deflection of 22.3 μm at a differential pressure of 70 kPa, and a membrane of side 200 μm has a deflection of 4.98 μm at the same applied load. From the above figure 3.5, it can be clearly seen that the deflection of the membrane increases for an applied pressure for increasing side lengths. Membranes with higher deflection will have higher strain levels and thus, increasing the gauge factor of the membrane (ref. equations 2.4, 2.5).

However, with the increase in dimension (for greater than 500 μm), there are chances of the inducing cracks in the membranes and also, the load handling capacity of the membrane can get reduced [2] . Hence a compromise has to be made between device integrity and performance.

3.3.2. Thickness v/s Differential Pressure

According to equation 3.1, deflection is inversely proportional to thickness. To achieve a higher strain in the membrane, the membrane should be as thin as possible. However, there are some limitations here. SiN_X membranes for dimensions under 100 nm, are extremely delicate and can fracture easily [53]. Hence, it is optimal to have to have 100 nm as the minimum thickness of the

membrane and this was varied till 300 nm in steps of 100 nm. Having membranes thicker than 300 nm is possible, but, we will be compromising on the device performance. Since a thicker membrane produces less deflection and hence the strain in the membrane will get reduced (ref, equation 2.2). Simulations were performed on *COMSOL Multiphysics* and the results matched with theoretical calculations. Also, having a thinner membrane compromises on the maximum load the membrane can handle [2]. The properties of the simulation model are mentioned in the table 3.5.

Table 3.5: Simulation environment for varying thickness of Si_X

Si_3N_4 Membrane	Value
Side length (μm)	500
Poissons's Ratio	0.22
Young's Modulus(GPa)	200

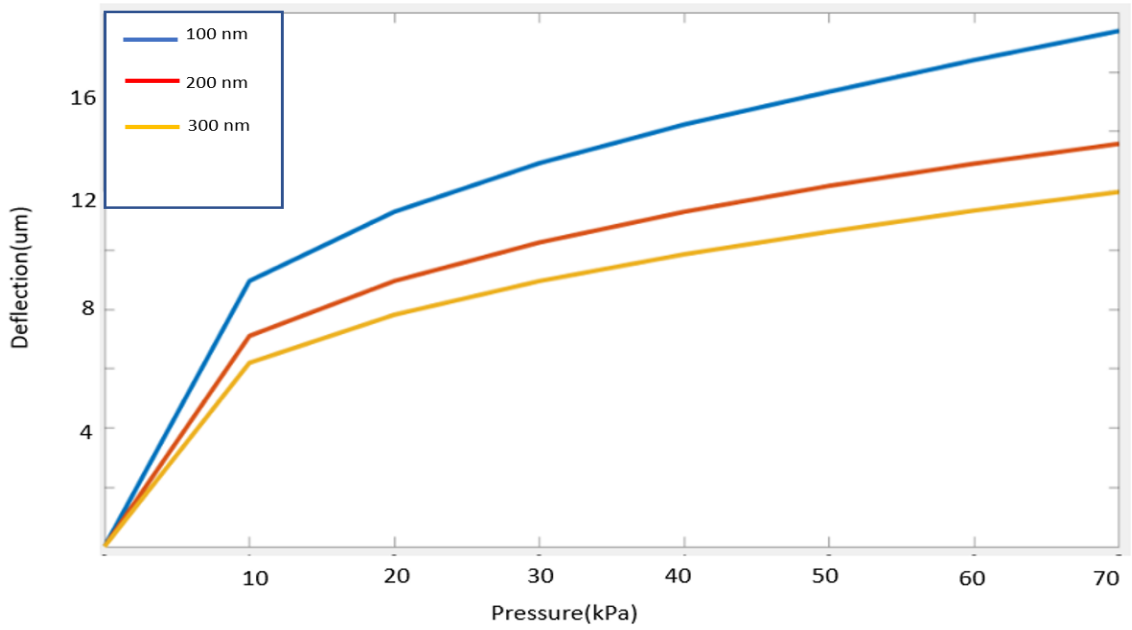

Figure 3.6: The variation of SiN_X thickness, versus differential pressure.

In figure 3.6, it is seen that the deflection increased from 9 μm to 16 μm as the thickness decreased from 300 nm to 100 nm. Hence, to have better performance, it would be ideal to have the membrane as thin as possible. Since, thinner membrane producces a higher deflection and hence a higher strain. Hence, the change of resistance in the graphene membrane will also be higher (ref eq 2.5, 2.4).

3.3.3. Hole Diameter v/s Differential Pressure

As noted by Q. Wang et al., perforations in the SiN_X effect the deflection of the membrane too and accordingly, the deflection is directly proportional to the diameter of the hole and that periodicity of the holes is insignificant. Having large holes means compromising the structural integrity of the membrane and while if the holes are too small, they are mostly insignificant. Hence, the diameter was varied from 6 μm to 10 μm in steps of 1 μm. The periodicity was constant at 20 μm. The properties used for the simulation environment are mentioned in the table 3.6.

Table 3.6: Simulation environment for varying radius if holes in Si_X

Si_3N_4 Membrane	Value
Side length (μm)	500
Thickness (nm)	100
Poissons's Ratio	0.22
Young's Modulus(GPa)	200

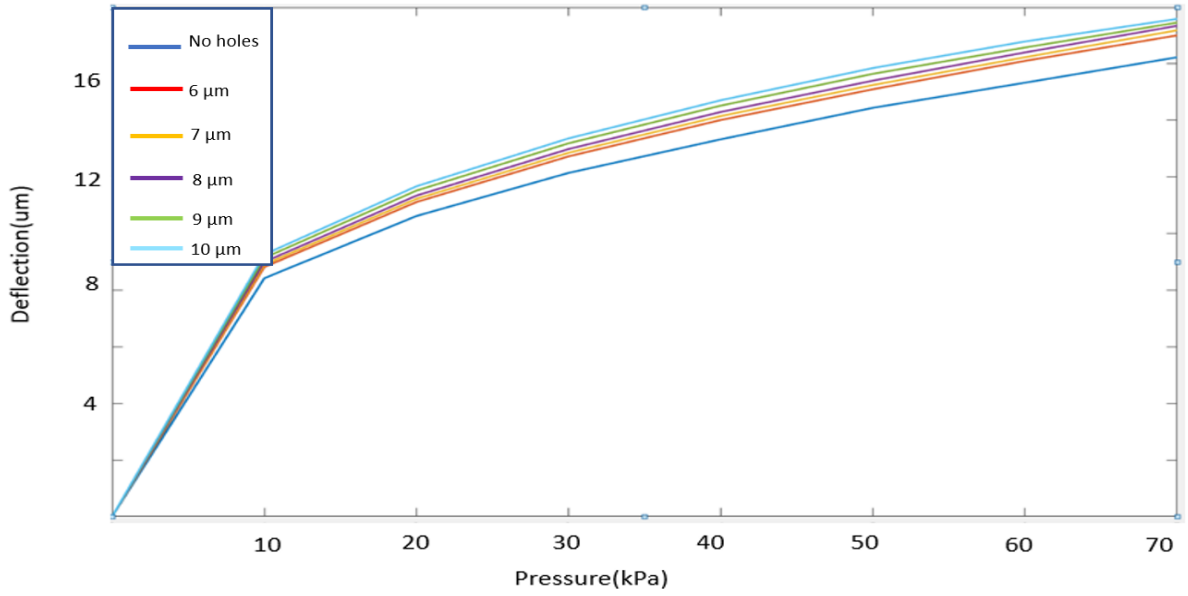

Figure 3.7: The change in deflection due variation in the radius of hole in SiN_X, as a function of the applied differential pressure.

It would be ideal to have holes with diameter of 4 to 6 μm as they offer a good balance between structural integrity and increased deflection. However, the processing had to performed using a contact aligner with backside alignment, and the critical dimension was limited to 8 μm. This meant that we invariably had to go for the radius of the hole near the critical dimension. Hence, the the hole radius was chosen to be 7.5 μm, 8 μm and 8.5 μm.

From the figure 3.7, the membrane with no perforations has a deflection of 16.3 μm at 70 kPa, while the membrane with perforations of radius 8μm has a deflection of 17.3 μm. The change between the two is minimal. Since the perforations have an impact on the integrity of the membrane, the perforations in the membrane can be avoided at a cost of minimal reduction in performance (ref eq 2.5, 2.4).

3.3.4. The Final Design

The details of the final design has been listed in the table below.
In the final design, parameters were chosen not only based on simulations, but, also due to fabrication conditions. The side length was restricted to a maximum of 575 μm due to the fact that the membranes are reported to be very delicate beyond 600 μm. The thickness was also chosen in a

Table 3.7: Design Parameters

Si_3N_4 Membrane	Value
Thickness (nm)	100,200,300
Side Length (μm)	100, 150, 425, 500, 575
Hole Radius (μm)	8, 9, 10
Hole Periodicity (μm)	20

way that the stresses on the membranes would not impact further fabrication processes.

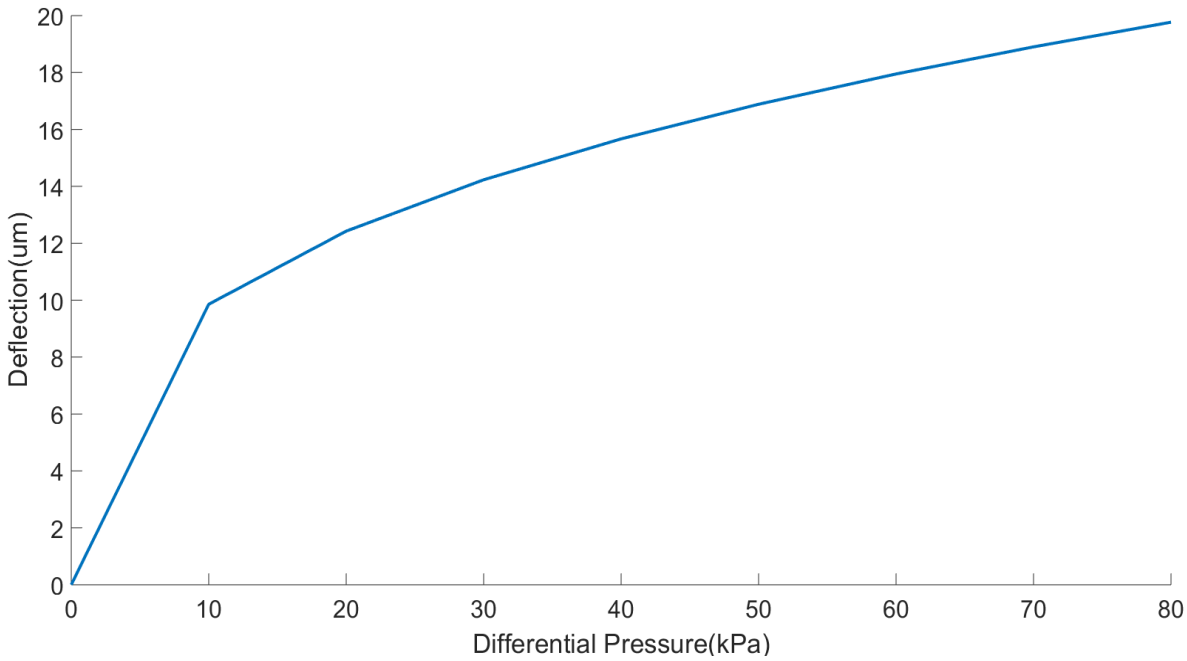

Figure 3.8: The deflection profile of the device.

In the figure 3.8, the device simulated has a side length of 575 μm, hole radius of 8 μm with a pitch of 20 μm. The membrane has a thickness of 100 nm. The properties of this simulation environment are shown in the table 3.8.

Table 3.8: Simulation parameters for the device shown in 3.8.

SiN_X Membrane	Value
Side length (μm)	575
Thickness (nm)	100
Poissons's Ratio	0.22
Young's Modulus(GPa)	200

The above figure 3.9 and the table 3.9 show the deflection profiles of the membranes derived from the literature and the membrane that has been designed in this work (shown in the figure 3.8). It is quite evident from the graph that the membrane designed in the previous section has higher deflection than the ones in the literature 3.8. This translates into a higher degree of strain and hence,

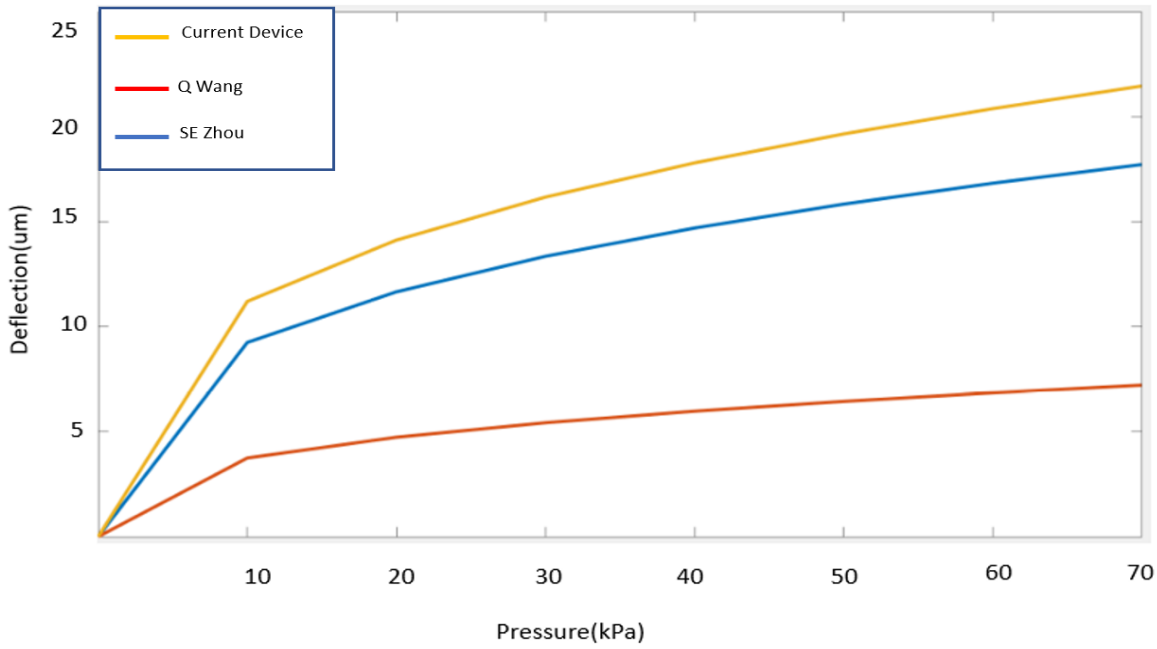

Figure 3.9: The comparison between the current design and the literature (Ref. [1] [2]).

a higher change in resistance and a corresponding change in the Gauge Factor (ref eq 2.5, 2.4)

Table 3.9: Comparison of the current device with literature at an applied pressure of 50 kPa.

Work	Thickness (nm)	Side length (μm)	Deflection (μm)	Avg. Strain
S. Zhu et al. [1]	100	280	6.6	0.0089
Q. Wang et al. [2]	100	500	14.1	0.00154
This work	100	575	16.2	0.00186

3.4. Free-standing Graphene-based Differential Pressure Sensor

As discussed in the earlier sections, the state of the art in graphene-based pressure sensors make use of transferred graphene on to a dielectric support layer, where the mechanical properties are completely dominated by the dielectric rather than graphene. Graphene being some atoms thick, can produce a deflection that is many times higher in terms of magnitude than a 100 nm thick Si_3N_4 for the membrane of same dimensions and applied load. This would be a way to realise devices with higher sensitivity. Also, for dimensions less than 50 µm [3], free-standing graphene membranes have been used. However, the sizes of the membranes are limited by the transfer process. Hence we are exploring the transfer-free graphene processing, as mentioned in the earlier section, to realize free-standing graphene membranes.

3.4.1. Mechanical Properties of Multi-layer Graphene

Graphene is an exceptionally strong 2D material. This is due to its planar covalent bond between the adjacent Carbon atoms. The mechanical properties of graphene also depend on the orientation. This planar structure also gives graphene its high Young's Modulus which is around 1 TPa for mono-layer graphene. However, process variation have an impact on the mechanical properties of graphene, and based on the number of layers and the type of graphene, the Young's Modulus was

found to vary from 0.6 TPa (multi-layer) to 1.2 TPa (mono-layer) while the Poisson's Ratio varied from 0.16 (multi-layer) to 0.45 (mono-layer). This has been reported by Reddy et al [35].

Since, we are using multi-layer graphene, the mechanical properties like Young's Modulus and Poisson's Ratio will be in-between that of graphite and mono-layer graphene, but weighted towards the later. Hence, in the simulation environment, we have considered the whole range of values with graphite at one extreme and mono-layer graphene as the other.

The deflection profile for *free-standing* graphene membranes is estimated by equation3.1. However, in case of multilayer graphene, comprssive stresses do exist, but for the simplicity of the calculation, it can be neglected. and hence the first term of the equation can be neglected. The modified equation for the applied load p is

$$p = C_2(\upsilon)\frac{tE}{a^4}\delta^3; \tag{3.3}$$

Where, $C_2(\upsilon)$ and constants, t is the thickness, a is the area, δ is the deflection, E is the Young's Modulus and υ is the Poisson's ratio.

From 3.2, C_2 is a constant derived from the geometry of the membrane. Since we are using a square membrane, here, the value of C_2 is taken from the literature and is equal to 1.994 [51]. Also, $f(\nu)$ can be expressed as [51],

$$f(\nu) = \frac{1-(0.271*\nu)}{1-\nu} \tag{3.4}$$

Hence, the value of $C_2(\nu)$ for ν = 0.28, is equal to 2.57 (from equations 3.2 and 3.4).
Here, ν is the Poisson's ratio of graphene.

3.4.2. Variation in Poisson's Ratio v/s Differential Pressure

Since there is a lot of variation in graphene processing, properties like Poisson's ratio is also impacted by the proceesing variations [35]. From equation 3.3, the deflection h is inversely proportional to $C_2(\upsilon)$, where υ is the Poisson's ratio. It is important to consider the variation in Poisson's ratio and it's impact on the deflection profile of the membrane. Below, simulations were performed by varying the Poisson's ratio from 0.19 to 0.40 [35], while the remaining parameters were kept constant.

Table 3.10: Simulation parameters for varying Poisson's Ratio

Multi-Layer Graphene Membrane	Value
Thickness (nm)	8
Side Length (μm)	500
Young's Modulus (TPa)	1
Pressure Applied (MPa)	0 to 60

From the figure 3.10, it is evident that for increase in Poisson's ratio decreases the deflection of the membrane. However, even at the extreme cases, for Poisson's ratio = 0.19 and 0.40, the difference in the deflection is significant for the extreme cases. Since, we use a multi-layer graphene, the Poisson's ratio would be somewhere around 0.2 to 0.3 . A value considered in this range should give an estimate of the device performance.

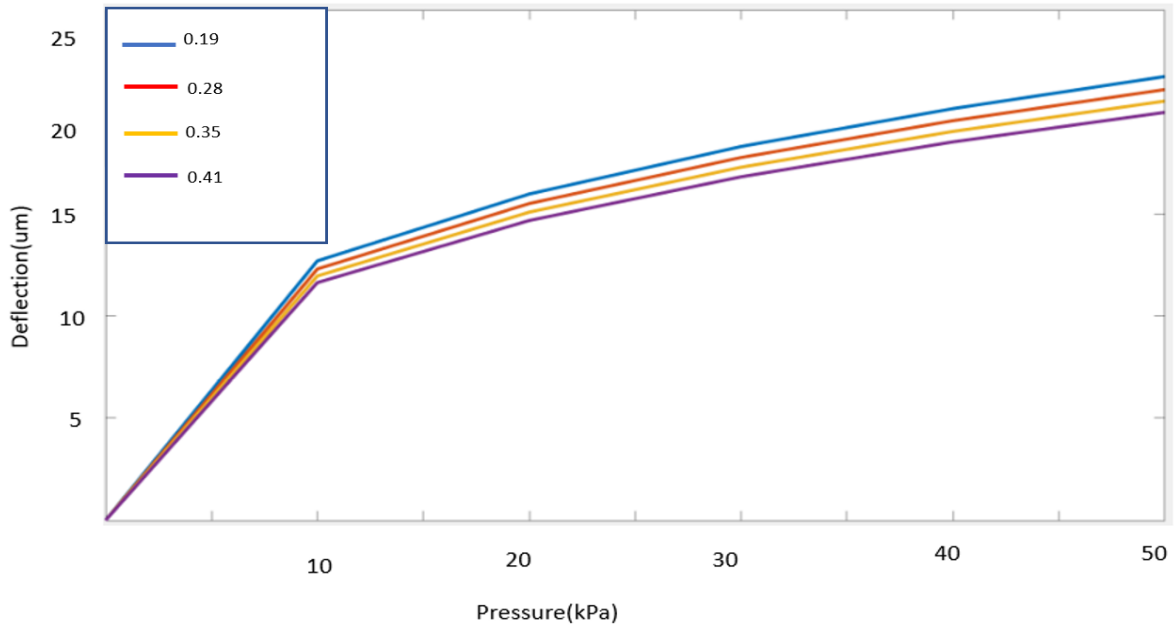

Figure 3.10: The deflection for variation in Poisson's ratio.

3.4.3. Variation in Young's Modulus v/s Differential Pressure

From Eq 3.3, the deflection of membrane is inversely proportional to the Young's modulus. In literature, the Young's Modulus of graphene varies from 0.5 TPa (graphite) to 1.2 TPa (Mono-layer graphene) [35]. In the below simulations, Young's modulus is varied from 0.5 to 1.3 TPa in steps of 0.2 TPa against an applied differential pressure from 0 to 50 kPa, while all the other parameters are constant. Since, we use a multi-layer graphene, the Young's modulus would be somewhere around 800 GPa to 1 TPa. A value considered in this range should give an estimate of the device performance.

Table 3.11: Simulation parameters for varying Young's Modulus

Multi-Layer Graphene Membrane	Value
Thickness (nm)	8
Side Length (μm)	500
Poisson's Ratio (TPa)	0.28
Pressure Applied (MPa)	0 to 60

From the figure 3.11, the deflection of the membrane increased as the Young's Modulus decreased. As mentioned in the literature, there will be a slight variation due different graphene growth techniques. However, even at the extreme ends, the variation is significant. A lower value of Young's modulus has a higher deflection and it's ability to handle the applied differential pressure will be limited.

3.4.4. Variation in Thickness v/s Differential Pressure

A monolayer graphene membrane has a thickness between 0.4 to 1 nm [54]. This is an estimation, but not an exact figure. When in comes to multilayer graphene where the membrane is made up of more than ten layers, the thickness can be estimated to be lesser than 10 nm. The thickness of the

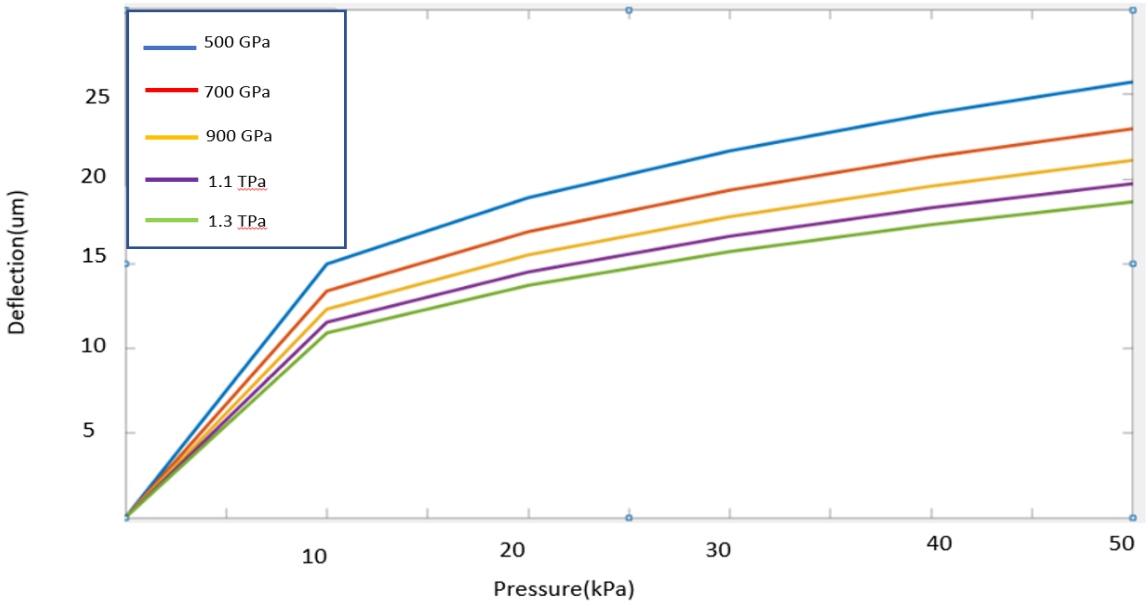

Figure 3.11: The variation in Young's Modulus, versus differential pressure.

graphene membrane depends of the number of individual layers. In CVD growth of graphene, the layers can be controlled by varying the growth time, however, we cannot have precise control over the thickness of the membrane as CVD graphene is not perfectly uniform. In the simulations, the thickness of the graphene membranes were varied from 2 nm to 12 nm while all the other parameters were kept constant. The output of the simulations matched the theoretical calculations and indeed the deflection increased for reduction in thickness.

Table 3.12: Simulation parameters for varying thickness.

Multi-Layer Graphene Membrane	Value
Young's Modulus (TPa)	1
Side Length (μm)	500
Poisson's Ratio (TPa)	0.28
Pressure Applied (MPa)	0 to 60

In the above figure 3.12, the deflection increases steeply as the thickness reduces from 12 nm to 2 nm. It would be very ideal to have a 2 nm graphene membrane, but, it has to be seen how mechanically strong the membrane is. CVD grown graphene generally has a few defects which can alter the mechanical properties [9]. However, as an alternative, it is better to have a thicker graphene membrane with multiple layers of graphene.

3.4.5. Variation in Side Length v/s Differential Pressure

From Eq. 3.3, it is evident that the deflection of the membrane is directly proportional to the side length A. Though it would be very desirable to have a membrane as large as possible, but in case of graphene, it is limited. The atomic defects, contaminants and pin-holes generally found in CVD graphene [2], make it extremely difficult to have membranes that large. In the simulation, the side length was varied from 100 μm to 575 μm and the other parameters were kept constant.

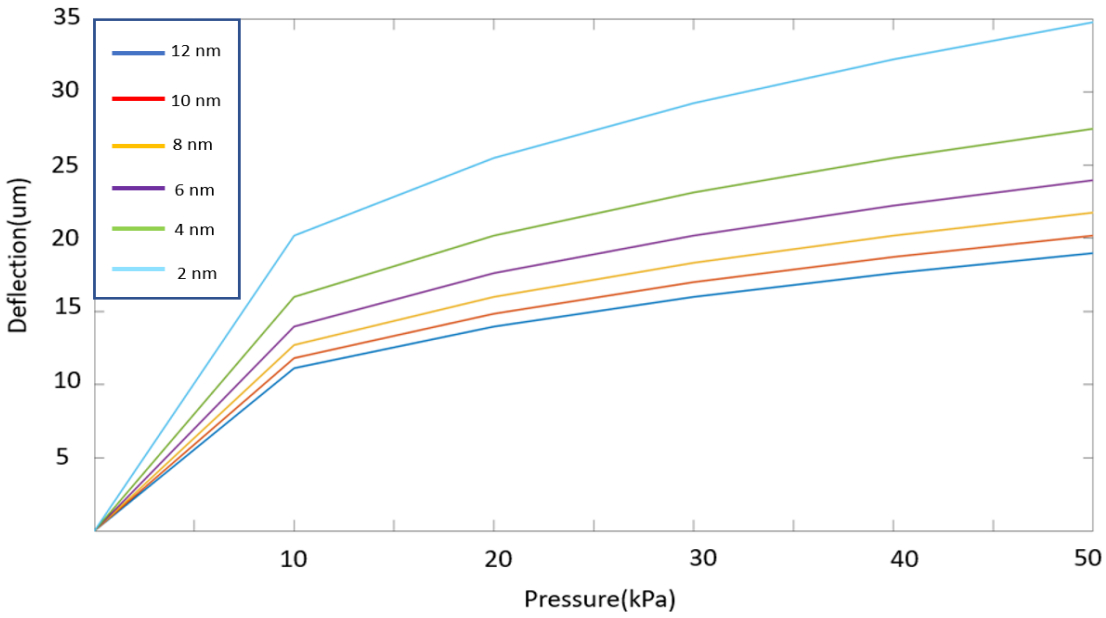

Figure 3.12: The variation in Thickness, versus differential pressure.

Table 3.13: Simulation parameters for varying side length.

Multi-Layer Graphene Membrane	Value
Young's Modulus (TPa)	1
Thickness (nm)	8
Poisson's Ratio (TPa)	0.28
Pressure Applied (MPa)	0 to 60

From the simulations and the theory, we can conclude that the deflection for an applied pressure increase with increase in the side length. However, for increased side length, the amount of differential pressure the membrane can handle also decreases. Hence a middle ground must be found between good performance (ref eq 2.5, 2.4) and structural integrity.

3.4.6. Final Design

With all the variables kept in mind, the final membranes had varying side length from 100 μm to 575 μm. Also, to achieve variation in thickness, the growth times were set at 10, 20, 30 and 40 minutes. The below table 3.14 lists the concluded design details.

Table 3.14: Final design parameters.

Free-Standing Graphene Membrane	Value
Growth Rate (min)	10, 20, 30, 40
Length (μm)	100, 200, 425, 500, 575
Pressure Applied (min)	0 to 50 kPa

Here, the growth rate is varied to achieve different thickness of graphene membrane. Based on the simulations, the side length was restricted to 575 μm as beyond this, the membranes are not structurally strong due to inherit defects and self buckling [55].

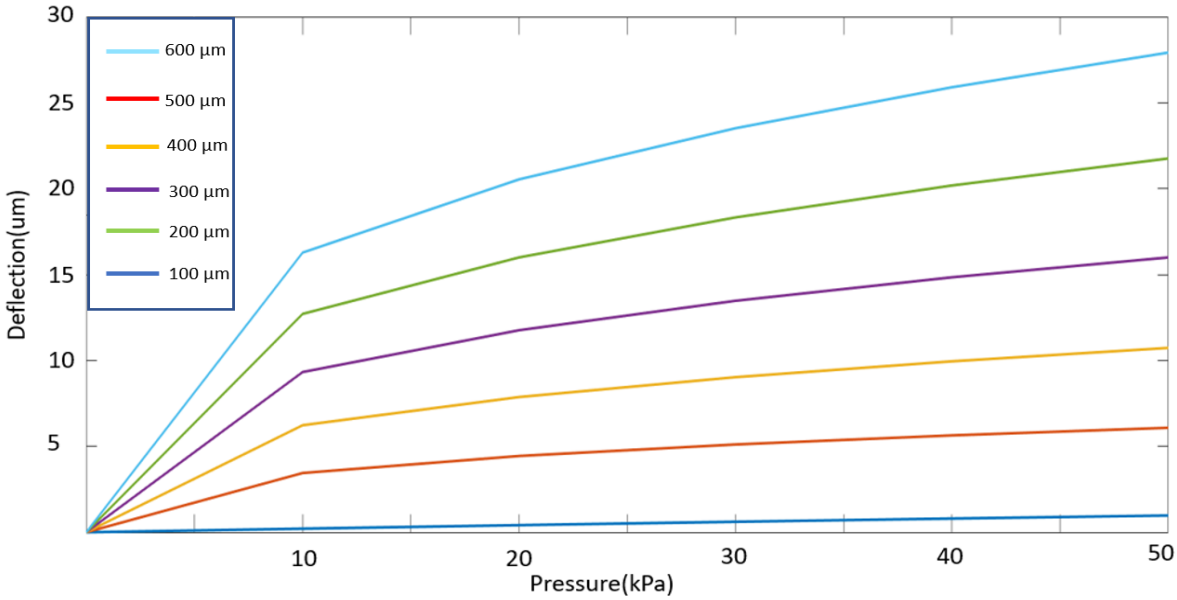

Figure 3.13: The variation in the length of the membrane, versus differential pressure.

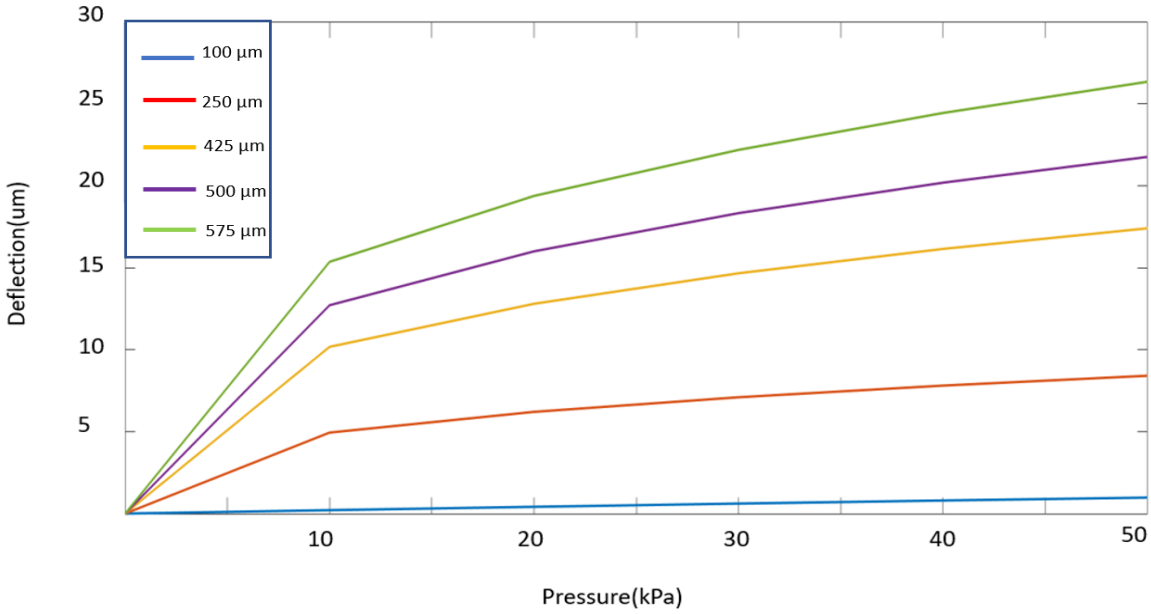

Figure 3.14: The final device dimension. Simulated at thickness= 8 nm.

3.5. Circular Membranes

Circular graphene membranes have been subjected to investigations recently. They have a number of potential applications [56] and hence, a transfer-free approach to procure them is of high importance.

Circular membranes of radius starting from 50 μm to 300 μm were simulated. The stress applied on the membrane is uniform and theoretically, it should have a better load handling capacity. However, during the simulations, the solution was never converged for the membrane of radius 300 μm. For membranes with smaller radii, the solutions did converge, but for a lesser degree of load. The figures show the results of the simulation.

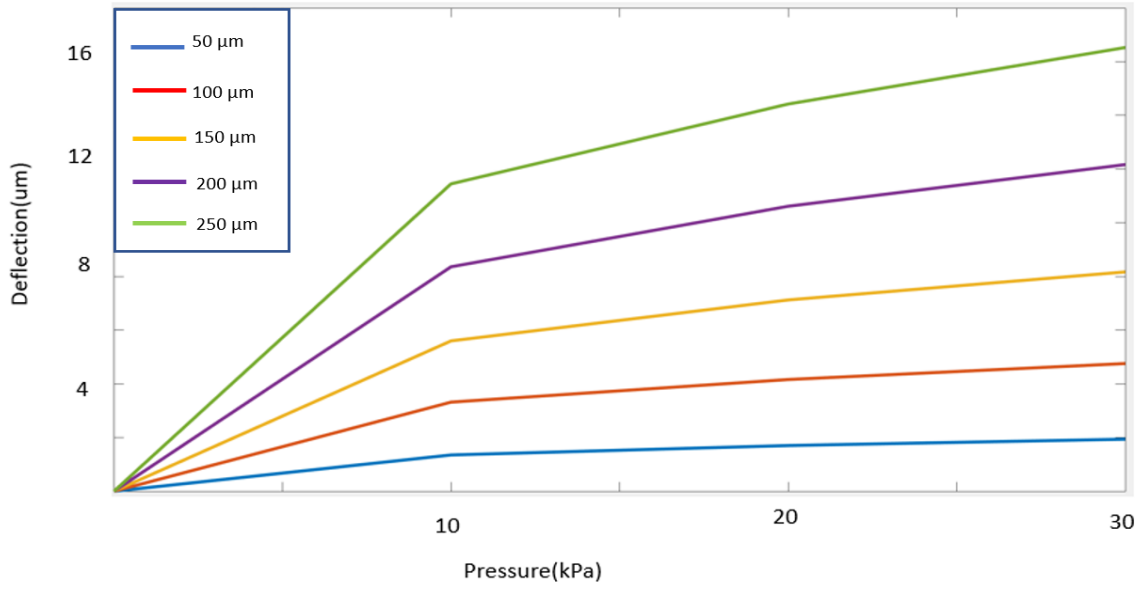

Figure 3.15: The deflection profile for membranes of varying radius.

From the figures 3.16, it is evident that the deflection increases for increase in the radius of the membrane. However, the constraints discussed in the previous sections are applicable here too. Mechanical parameters and the defects in the membrane play a huge role in the performance of the device. Any variation in any of those parameters will have a consequence on the device.

3.6. Conclusion

3.6.1. Graphene on SiN_X

From the table 3.9, it is clearly evident that the device designed here, has a higher out of plane deflection at 50 kPa than the current state of the art. Strain values were also calculated and the device designed with a 100 nm thick SiN_X support layer having a side length of 575 μm has higher strain levels than the state of the art. Higher strain corresponds to a non-linear increase in the resistance of graphene (2.4, 2.5) and hence, the Gauge Factor should also be higher.

3.6.2. Free-standing Graphene v/s Graphene on a Support Membrane

In the previous section, graphene membranes on SiN_X support layer and free-standing graphene membranes have been discussed. By looking at the simulations, free-standing graphene membranes have a deflection of 21 μm for a differential pressure of 500 mbar. While at the same pressure, a 100nm SiN_X has a deflection of 13.8 μm, while perforated SiN_X has a deflection of 14.1 μm. However, any variation in the assumed mechanical properties of graphene will alter the deflection

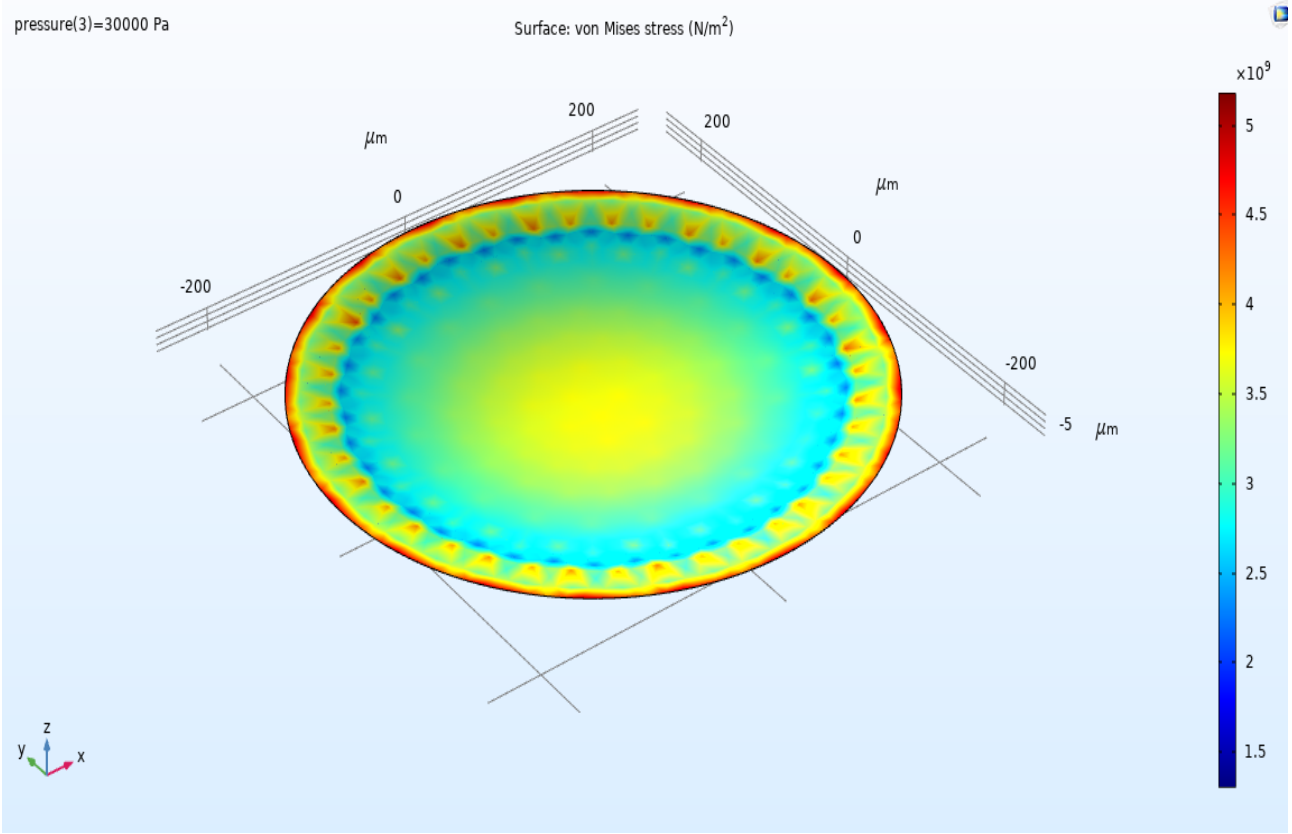

Figure 3.16: The volumetric strain of a membrane of radius 250μm at 10 kPa.

profile of the membrane. Also, we can conclude that graphene membrane is very delicate and the amount of differential pressure it can sustain is restricted when compared to SiN_X membranes.

Table 3.15: Comparison between different membranes.

Parameter	Free-Standing Graphene Membrane	Standard Si_3N_4	Perforated Si_3N_4
Pressure Applied (mbar)	50	50	50
Length (μm)	500	500	500
Thickness (nm)	8	100	100
Deflection (μm)	21	13.8	14.1
Average Strain	8	100	100
Maximum Pressure(kPa)	55	60	60
Average Strain	0.0025	0.0013	0.0015

The figure 3.17 and table 3.15 clearly indicates the performance of the membranes against the applied pressure. Free-standing graphene membrane has roughly 40% more deflection than perforated SiN_X membrane. Such a device will have a higher gauge factor than the other cases (2.2). However, from the simulations, the maximum pressure free-standing graphene membrane can handle is restricted in comparison to the SiN_X membranes. We can conclude that while it possible to have devices that produce more deflection for the same load applied than the current state of the art, considering the dedicate nature of the processing, it has to be seen how reachable the devices are.

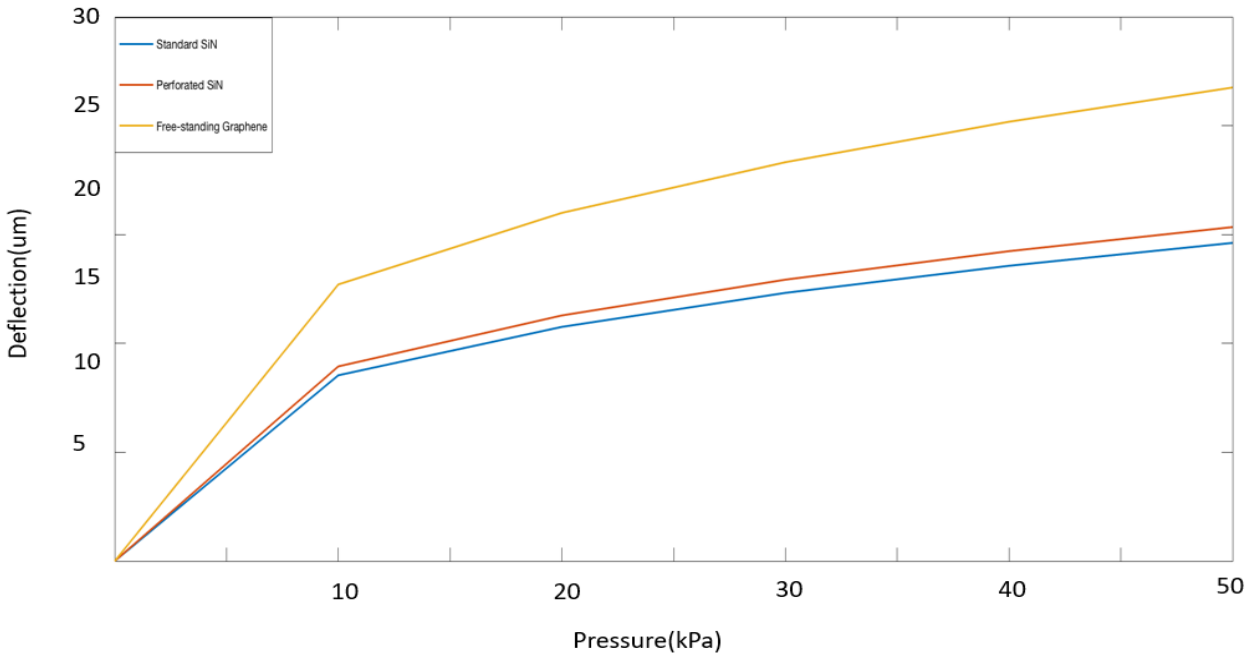

Figure 3.17: The final device dimension. Simulated at thickness= 8nm

Simulations generally indicate the maximum reachable potential of the design model, however, there is a lot of process variations that can take place during the actual processing of the devices. In the case of free-standing graphene for example, for the membranes to survive, the number of defects in the layer must be kept at minimum. Graphene being extremely delicate, can get fractured to the presence of defects and pinholes [2]. Hence, even though the simulation model predicts a better performance for free-standing graphene membranes, a lot depends on the process parameters and conditions.

4

Fabrication

In the previous chapters, the theory behind pressure sensing, the properties of corresponding materials and graphene in particular has been discussed. Further, simulations were performed in COMSOL Multiphysics and the dimensions of the devices were finalized. In the current Chapter, the process flow for each design will be discussed in detail, starting from the mask designs, to defining the flowchart and the processing in the cleanroom.

4.1. Mask Design

A *photomask* is generally a transparent plate with specific opaque regions, and when light is passed through it, forms patterns on the exposed substrate.
Based on the type of patterns, a photomask can be classified into *brightfield* or *darkfiled*.

- Brightfield Mask: In a brightfield mask, the pattern to be defined is opaque. This is shown in the figure 4.1. When the substrate is exposed to UV radiation through this mask, all the areas except the pattern that is to be defined will be exposed to the UV radiation.
- Darkfield Mask: In a darkfield mask, the pattern to be defined is transparent. This is shown in the figure 4.1. When the substrate is exposed to UV radiation through this mask, only the areas that define the pattern are exposed.

However, to create pattern on bare Silicon on exposure to UV radiation (excluding high density lasers) in not possible, hence, we use a photosensitive layer that can be coated on Silicon and make these pattern achievable. This photosensitive layer is called as photoresist. Photoresist is an organic polymer when exposed to UV radiation undergoes a structural change so that it either becomes insoluable to a photoresist developer or can be easily be soluable and then removed by a photoresist developer. The two types of photoresists are called are positive or negative photoresists. This is shown in the figure 4.2.

- Positive Photoresist: This is a type of photoresist when exposed to UV radiation, becomes soluble to photoresist developer.
- Negative Photoresist: This is a type of photoresist when exposed to UV radiation, becomes insouble to photoresist developer. The parts that are unexposed are soluble to photoresist developer.

Using the combination of the two different masks and the two different photoresisits, patterns on the substrate are defined. The patterns can be defined to remove some parts of the substrate or to add new layers to the substrate on specific regions.

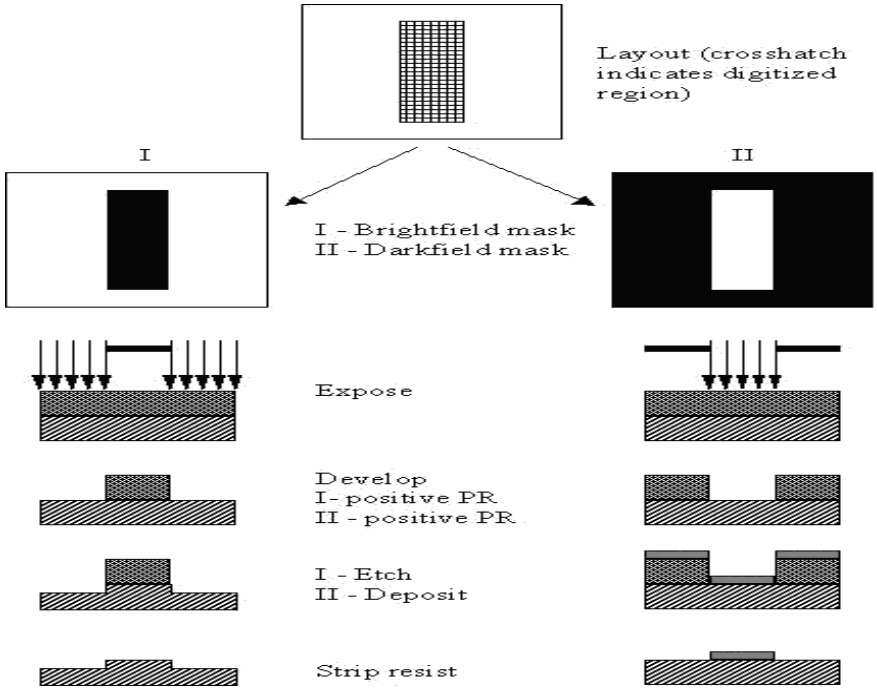

Figure 4.1: Illustration of Brightfield and Darkfield Photomasks on a positive photoresist, refereced from [57].

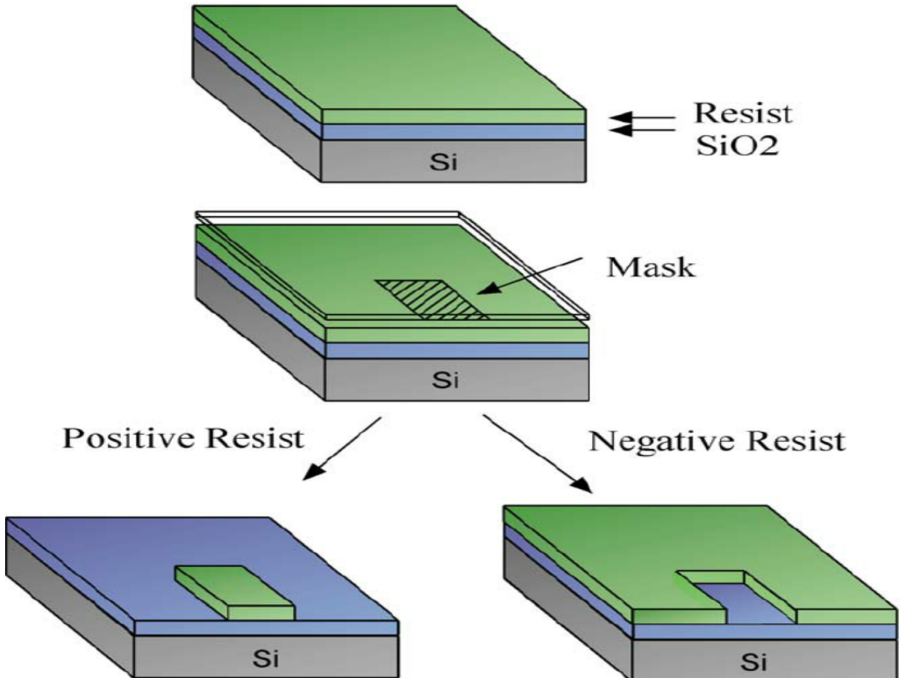

Figure 4.2: Photoresist types when exposed through a brightfield mask, referenced from [58]

4.1.1. Layers

To realize the devices we discussed in the earlier sections, multiple steps that involve both addition of new layers and removal of material in specific locations have to be performed. Based on the type of the layer, we define the type of mask and the corresponding photoresist. Looking at our device, we have divided the multiple layers as following.

- Layer 1- Back Etch: Opening of a window for etching. The SiN_X layer on the back will be

patterned through this mask. This is a dark-field mask.

- Layer 2- Mo Catalyst: The Mo catalyst used for graphene growth will be patterened. This is a brightfield mask. This is a bright-field mask.
- Layer 3 - Metal: The negative photoresist (for lift-off) will be patterened using the current mask. This is a bright-flied mask.
- Layer 4- Holes in SiN_X: This mask is used to pattern holes in the SiN_X membrane. This is a dark-field mask.
- Mask Layer 5: This is used to pattern the back-side of the wafer. This is a dark-field mask.

The different masks that are used to define the device are shown in the figure 4.3.

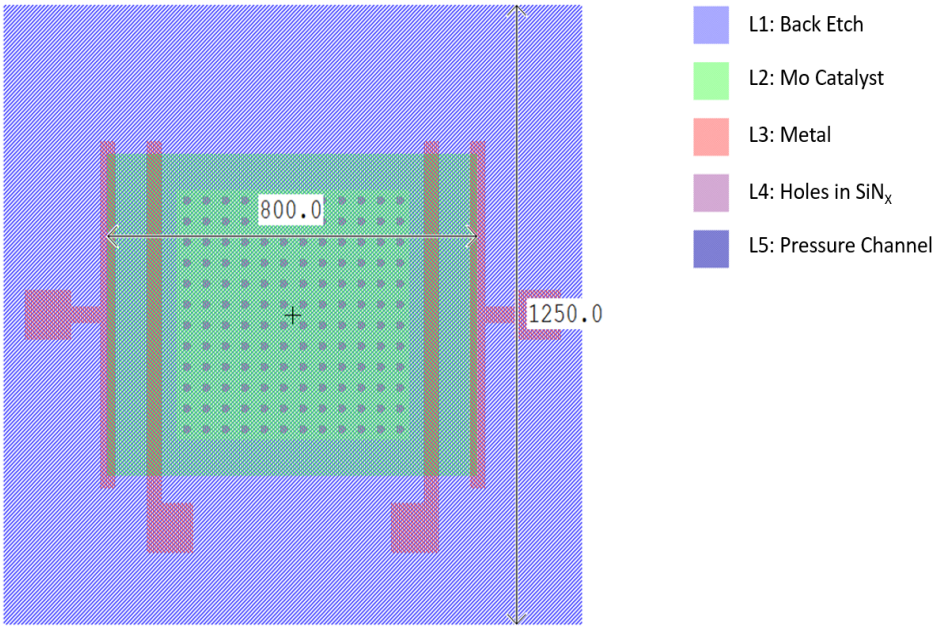

Figure 4.3: The different masks used in the process flow.

4.2. Layout

To translate the devices into different layers and it's constituent masks, we need to first describe the layout of the device first. The layout can be termed as the visual representation of the final device. The layout design comprises of various layers that are to be processed and will be then translated into corresponding masks.

The design parameters were derived from the previous Chapter (ref 3) and devices with different sizes and layers were implemented using the same mask set. In the section below, the layer-wise composition of each device will be explained.

4.2.1. Top View of the Devices

The figure 4.4 represents the top view of the device. This single unit is called as a cell and multiple instances of this are placed around a 4 inch Silicon wafer.

In the figure, we can see a square of length 1250 μm, this represents the window in the backside of the wafer, which is later used as a hard mask for bulk etching of Si (in KOH or TMAH). The green square of side equal to 800 μm, represents the Mo catalyst for graphene growth. Th four electrodes are placed in contact with the Mo catalyst (Structures in Red).

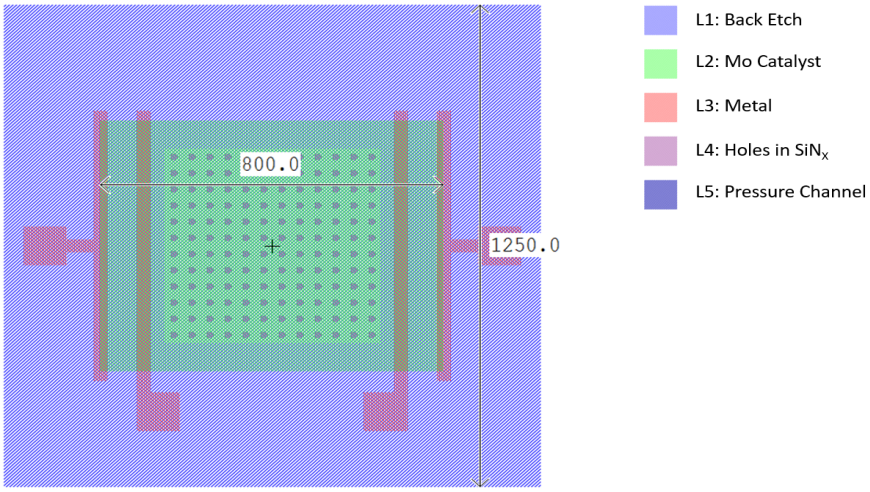

Figure 4.4: The top view of the device with square membrane.

The figure 4.5 represents the topview of the device with a circular hole. Here, the circle of radius 250 μm represents the hole in the substrate.

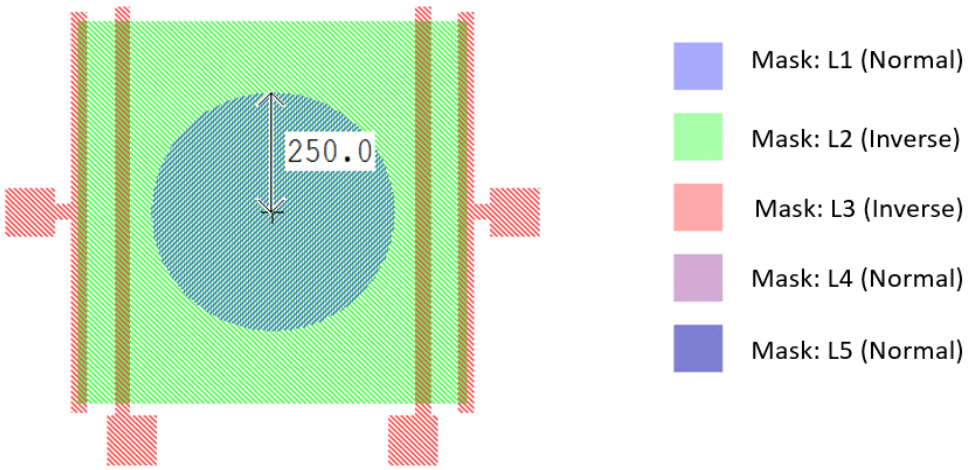

Figure 4.5: The top view of the device with circular hole.

4.2.2. Calculation for the backside opening

The rate of etching of Silicon depends on it's orientation. Hence, during wet etching, we see high anisotropy. For <100> Silicon, the etching occurs along the <111> plane, which is at 54.7° to the <100> plane. This is shown in the figure 4.6.
Hence, to have a 500 μm square hole on the front of the wafer, we need a much larger opening on the backside. This is calculated by some simple trigonometric equations given below.

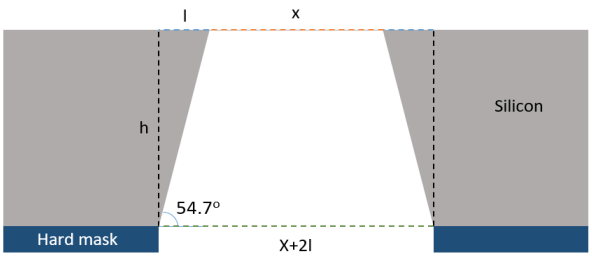

Figure 4.6: The wet etching profile of <100> Silicon in alkaline solution.

$$l = h/tan(54.7) \tag{4.1}$$

$$l = 525\mu m/1.41 \tag{4.2}$$

$$l = 371.72\mu m \tag{4.3}$$

$$x + 2l = x + 743\mu m \tag{4.4}$$

Where x is the opening in the front and h is the thickness of the wafer.

From this, we derived the side lengths for the back etch window for corresponding hole size on the front.

Table 4.1: The side length of the window opening for alkaline etching.

Size of Front Opening (μm)	Corresponding Value of Back-etch Window (μm)
125	868
250	993
425	1168
500	1243
575	1318

4.2.3. Membranes Suspended Over Radial Holes

In our design, we also included membranes that were suspended over radial holes. Since we cannot achieve circular geometries through wet etching, we opted for a dry etching method for this purpose. Dry etching is anisotropic and hence the orientation of Si does not matter. Hence, the exact radius of the holes were described in the Mask Layer 1-Back Etch. The below table represents the same.

Table 4.2: The different radii of the circular holes.

Radius of the hole (μm)
50
100
150
200
250
300

4.3. Process Flow

In this section, the process steps of all the different devices and designs will be discussed. We start with bare Silicon wafers, and after series of addition and removal processes, we end up with our final device. Below are the process flows for different designs.

4.3.1. Graphene on Silicon-nitride

In these devices, the graphene membrane is suspended on a SiN_X mechanical support layer.

Step 1

We start our processing with 4 inch dual side polished p-type doped Si wafers. The initial step is to inscribe the wafers with alignment markers. These markers help in aligning different layers of the mask to the wafers.

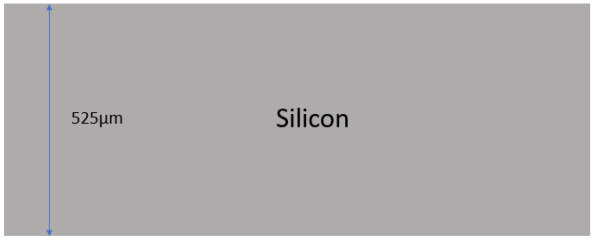

Figure 4.7: 4 inch Dual Side Polised wafer with alignment markers.

Step 2

Then the wafers undergo a wet oxidation process and roughly 600 nm of oxide is grown on the wafer. The process happens in a furnace at a temperature of 1100°C and for a time of 53 minutes. The figure below represents the state of the wafer. The thickness of the layer was measured using a refelectometer and it was found to be 599.40nm. The stress of the membrane was measured using a laser stress analyser, and it was 223 MPa of compressive stress.

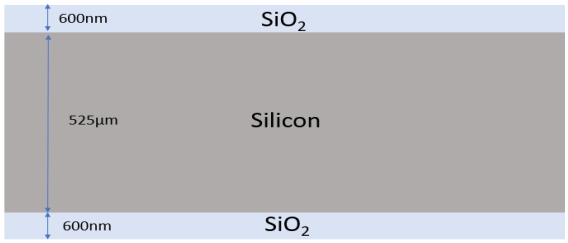

Figure 4.8: Device after Step 2.

Step 3

Following this, SiN_X is deposited through an LPCVD process. The thickness of the membrane depends on the duration of deposition and the same is shown in the table 4.3. An LPCVD deposition is uniform and we get SiN_X on both the front and the back. SiN_X on the front acts as a support layer for the graphene membrane, while, it acts as a hardmask on the back.

The thickness of the layer was modeled and measured on VASE Eplisolemter and the resultant thicknesses are tabulated below with corresponding stress measurements.

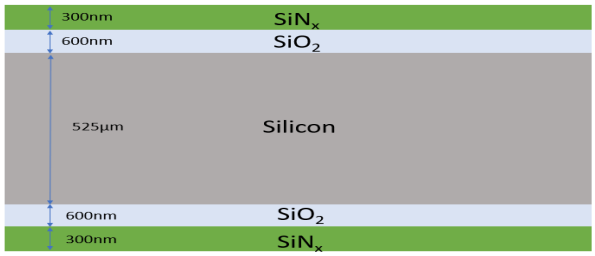

Figure 4.9: Device after Step 3.

Table 4.3: Measured thickness and stress of LPCVD Si_3N_4

Expected Thickness(nm)	Measures Thickness(nm)	Stress(MPa)
100	95	272
200	217	263
300	330	281
500	510	267

Step 4

The SiN_X on the back is etched through mask Layer 1-Back Etch with a positive photoresist and windows are formed in the SiN_X membrane. The etch time depends on the thickness of the layer and it is mentioned in the table 4.4. These windows act as a hard mask for KOH etching of Si. The etching was performed by as plasma etcher.

Table 4.4: Etch times for different SiN_X membranes.

Thickness(nm)	Etching Time(Seconds)
100	30
200	60
300	90
500	140

The wafers are then cleaned to remove any debris from the etching process.

Step 5

Further, a 50 nm thick layer of Mo was sputtered on top of the wafer. The deposition happened at 50°C. Later, Mo was patterned using a reactive ion etcher for 30 seconds. Mask layer 2 - Mo catalyst was used with a positive photoresist for this purpose.

Step 6

Later, graphene was grown on top of the Mo substrate using AIXTRON BLACKMAGIC at 915°C. Since graphene is optically transparent, it is very hard to confirm its existance on Mo. Hence, we performed a series of Raman Spectroscopy measurements to affirm the same. Graphene was grown for 10, 20, 30 and 40 minutes respectively. This stage of processing is represented by the image 4.10.

Step 7

Later, the front side of the wafers were coated by a negative photoresist (nLOF 2020) and then exposed through the mask Layer 3 - Metal to form patterns for the electrodes. 10 nm of Cr was evap-

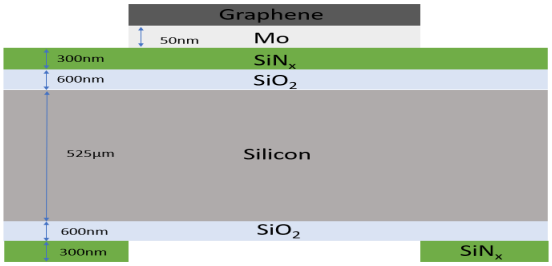

Figure 4.10: The device after the graowth of graphen on the Mo catalyst.

orated followed by 100 nm of Au. Cr is an adhesion layer between SiN_X and Au. A liftoff was performed by dipping the wafers in NMP at 70°C. By this process, the four electrodes were defined on the graphene membrane (fig 4.11).

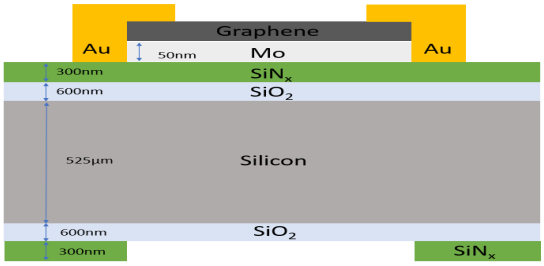

Figure 4.11: The device after performing a gold lift-off.

The front side of the wafer was coated by a 3 μm thick positive photoresist(AZ 3027) and further baked at 100°C for 2 minutes. This was an additional proctective layer for the structures on the front side for alkaline etching of Silicon.

Step 8

In order to release the piezoresisitive membrane, the 600 nm thick oxide on the back is removed. This is done by wet etching of the wafers in a buffered hexa-flourine (BHF or BOE 1:7) solution for approximately 10 minutes and then we land on Silicon. This is followed by etching of Si in KOH solution. For this purpose, 30 percent KOH is used at a temperature of 85°C for roughly 5 hours. The etch rates for KOH are shown in the image 4.12.

The oxide on the top is removed by BHF solution for 10 minutes. This is followed by removal of the photoresist in acetone and followed by the removal of Mo in H_2O_2 solution. After this, the process flow is complete and the finised devices are represented by the figure 4.13.

4.3.2. Graphene on Silicon-carbide

The initial steps till the growth of oxide are similar to the earlier designs. It is shown in the section 4.3.1.

Step 3

Following 600 nm of wet oxidation, SiC is deposited through a PECVD process. A 500nm thick SiC layer was deposited on the front of the wafer for a time of 30 seconds. The thickness of the layer was

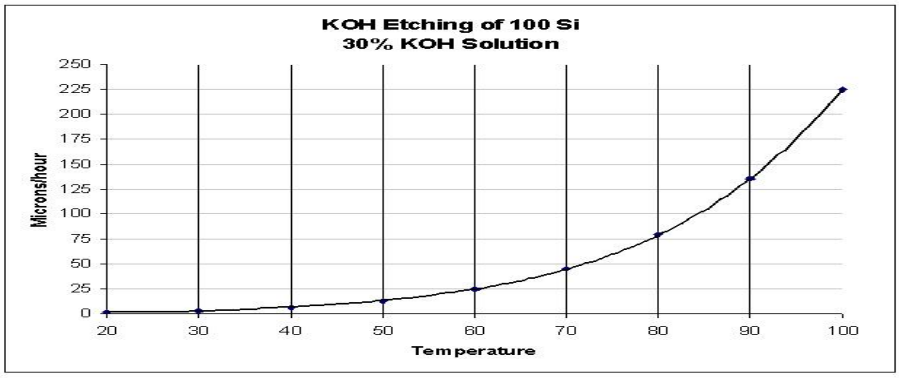

Figure 4.12: Etch rates for <100> Silicon in 30 percent KOH, sourced from [59].

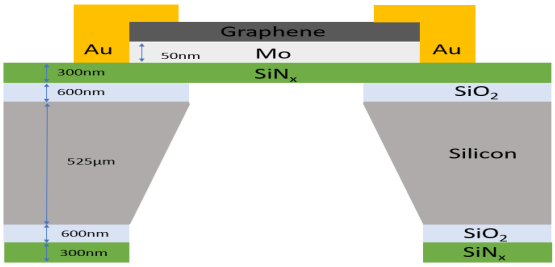

Figure 4.13: The device after complete fabrication.

modeled and measured on Woollam Eplisolemter and the resultant thicknesses was 525 nm.

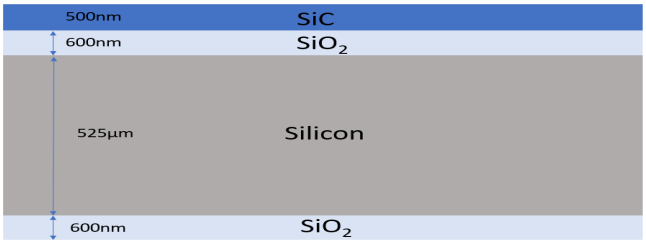

Figure 4.14: PECVD deposition of SiC on the front side of the wafer.

The oxide on the back is etched through mask Layer 1 - Back etch with positive photoresist for 70 seconds on a plamsa etcher. Windows are formed in the oxide membrane and these act as hard-masks for TMAH etching. This is shown in 4.15.

The subsequent steps that involve sputtering of Mo to performing lift-off are mentioned in section 4.3.1.

Step 7

The wafers are etched in TMAH solution. For this purpose, 10 percent TMAH is used at a temperature of 85°C for roughly 14.5 hours. The etch rates for TMAH are shown in the image 4.16.

The oxide on the top is removed by BHF solution for 10 minutes. This is followed by removal of the photoresist in acetone and followed by the removal of Mo in H_2O_2 solution. The etch of oxide in

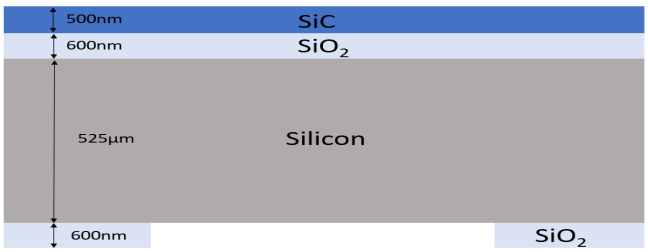

Figure 4.15: The oxide is etched on the back using a plasma etcher.

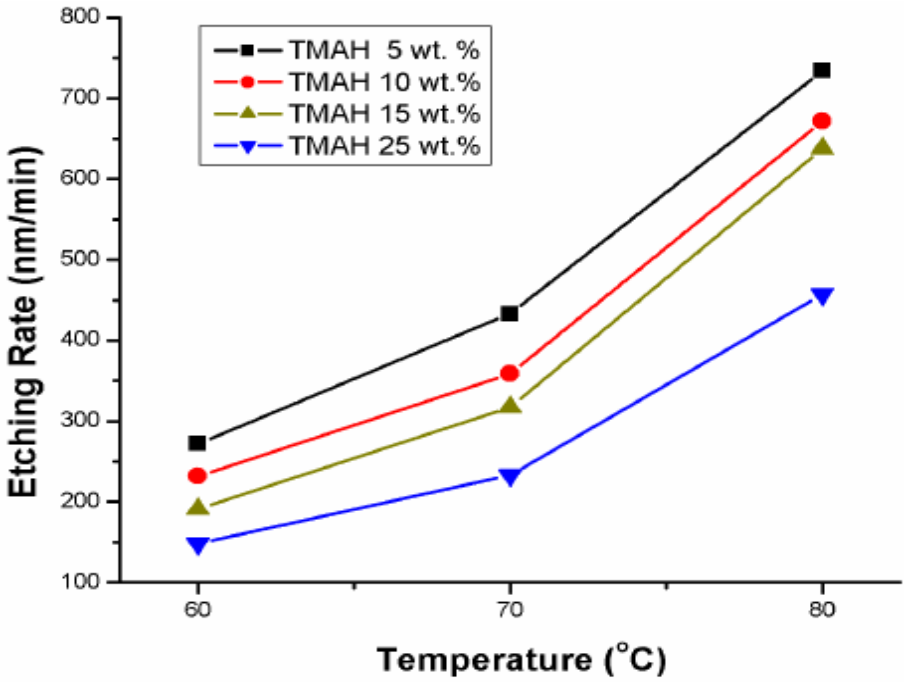

Figure 4.16: The oxide is etched on the back using a plasma etcher, sourced from [60]

BHF, also removes the oxide hard-mask on the back. The final device is shown in the figure 4.17

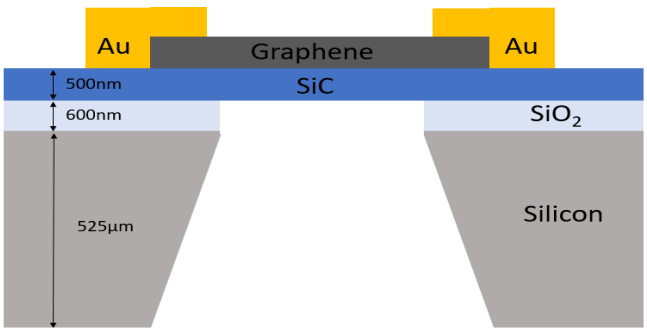

Figure 4.17: The device after complete fabrication.

4.3.3. Free Standing Graphene on Circular Holes

In order to achieve radial holes in the Silicon substrate, we had to opt for dry etching methods instead of bulk etching. As discussed earlier, wet etching of Si is anisotropic and will only result in square holes. Hence, the process was modified to suit the needs of DRI Etching. The process flow is explained in the section below.

Step 1

We start our processing with 4 inch dual side polished p type doped Si wafers. The initial step is to inscribe the wafers with alignment markers. These markers help in aligning different layers of the mask to the wafers.

Step 2

SiO was deposited on both the front and the back of the wafer through a PECVD process. A 6 μm thick oxide layer was deposited at a time of 1 minute. The thickness of the layer was modeled and measured on Woollam Epsilometer and the resultant thicknesses are tabulated below (table 4.5). The process stage is represented by the figure below. The oxide on the front acts as a stopping layer for DRIE, while oxide on the back is the hard mask for the etching process.

Table 4.5: The thickness of PECVD oxide and it's corresponding stress

Orientation	Expected Thickness(μm)	Measures Thickness(μm))
Front	6	5.94
Back	6	5.99

Step 3

Later, a 300nm thick PECVD Si_3N_4 was deposited on the front. The device is shown in the figure 4.18.

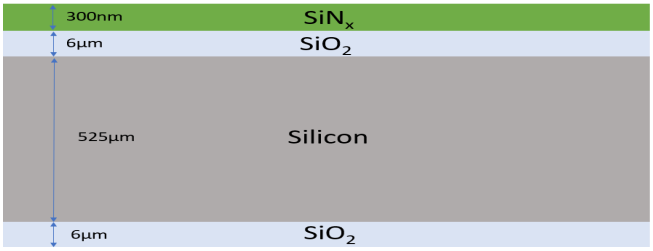

Figure 4.18: A PECVD deposition of SiN_X is performed on a 6 μm thick PECVD oxide.

Step 4

Patterns were formed on the back through Mask: Layer 1- Back etch and a positive photoresist. The oxide layer was etched in a plasma etcher for a time of 13 minutes. This is shown in the figure 4.19. Circular windows were formed on the back oxide after this process step.

The further processing from depositing Mo to the lift-off performed are similar to section 4.3.1.

Step 6

DRIE (Deep-Reactive-Ion-Etching) was performed to etch the bulk Si in circular patterns. Si was completely removed and we landed on the 6 μm thick oxide on the front. The device is represented by the figure 4.20.

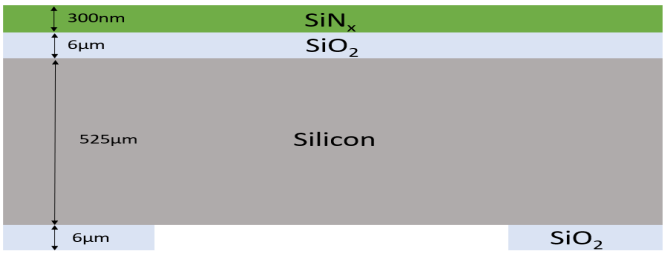

Figure 4.19: Windows are etched in the back oxide. This acts as a hard mask for DRIE.

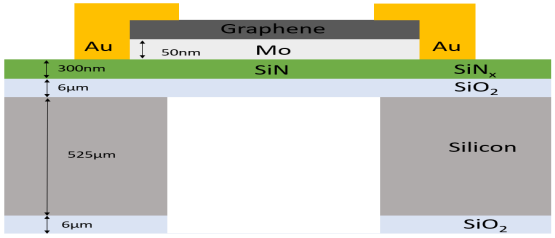

Figure 4.20: The device after DRIE removal of Si.

Step 5

Mo was removed from the front of the wafer using H_2O_2 for 5 minutes. Further, the wafers were etched from the back using a Vapour HF Etcher to remove the Oxide layer and the PECVD SiN_X. Etch etch cycle was timed for 3 minutes and inspection was performed before proceeding to the next cycle.

The completed device is shown in the figure 4.21.

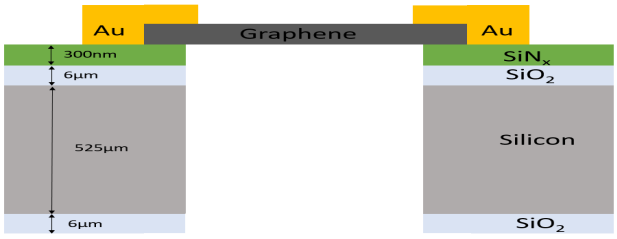

Figure 4.21: The device after complete fabrication.

4.3.4. Free-Standing Graphene Membranes

The steps 1 to 3 of the processing are similar to the initial processing steps for devices with graphene on SiN_X (refer 4.3.1).

Step 4

The SiN_X on the back is etched through mask layer 1 - Back Etch with positive photoresist and windows are formed in the SiN_X membrane. The etch time depends on the thickness of the layer and it is mentioned in the table 4.3.

Step 5

The front of the wafer is coated with a negative photoresist and exposed with Mask Layer 2- Mo Catalyst. After developing, the photoresist is removed from certain areas which define patterns on the front SiN_X layer. After plasma etching, we get openings in the SiN_X membrane on the front. This is represented by the image 4.22.

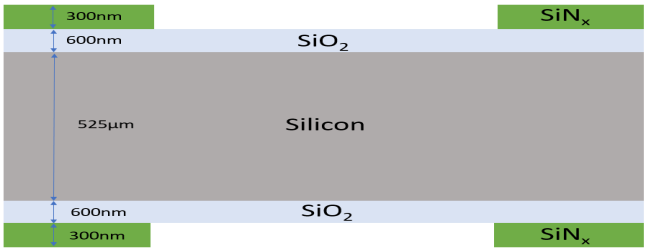

Figure 4.22: The Si_3N_4 is etched from both front and the back of the wafer.

The subsequent steps involve sputtering and patterning of Mo. This is followed by graphene growth and then a lift-off is performed to define the metal contacts (4.3.1) .

Step 6

After performing lift-off, the oxide on the back is removed by wet-etching in BHF (for 10 minutes). This is followed by wet etching of bulk Si in 10 percent TMAH at 80 °C for 14.5 hours. The resulting structure resembles the figure 4.23. After the etching is complete, the bulk Si is completely removed and we land on the oxide layer on the top.

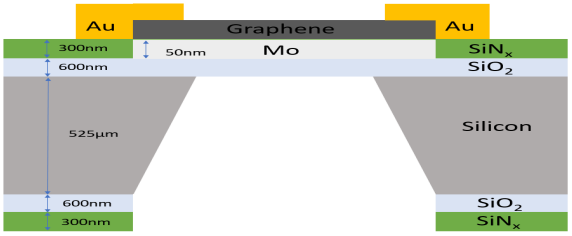

Figure 4.23: The device after etching of bulk Si.

Step 7

The front side of the wafer is then then treated with H_2O_2 to remove Mo. Graphene now lands on the oxide membrane. This is seen in the figure 4.24.

Step 8

The oxide is then etched in vapor HF. The SiN_X on the back acts as the hard mask during the process. The etch cycle is define for 1 minute. In between, visual inspections are performed to determine the rate of etching. Vapor HF has an oxide etch rate of 100 nm/ minute.

After the removal of the oxide layer, the graphene membrane is freely suspended. This is seen in the figure 4.25.

4.3.5. Graphene on Silicon-oxide

In this device, the structural support membrane for graphene was replaced by Silicon-oxide. The processing is similar to the steps mentioned in the section 4.3.4 starting from thermal oxidation to

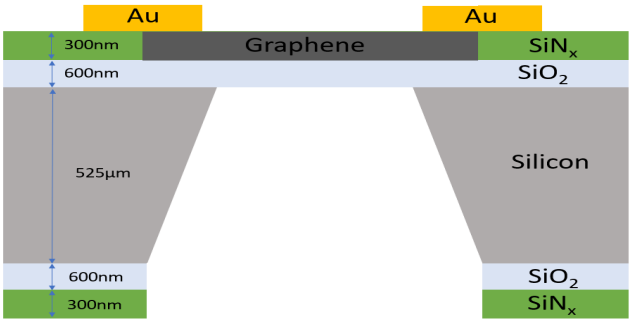

Figure 4.24: The device after complete fabrication.

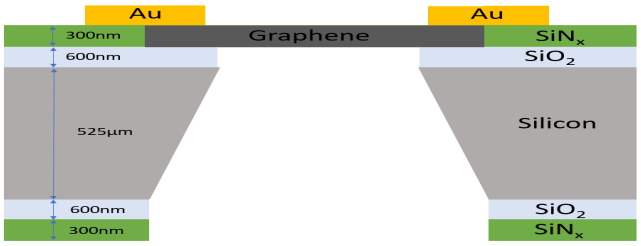

Figure 4.25: The device ethcing of SiO on the top.

the lift-off.

Slight variation is seen in the bulk etching though. At first the 600 nm oxide of the back is removed by wet etching in BHF for 10 minutes. This is followed by wet etching of Si in 10 percent TMAH at 80 °C for 14.5 hours. The process can be done in KOH too, but KOH has reduced selectivity to oxide than TMAH. So the risk of etching the top oxide is high in the case of KOH.

The bulk Si is removed by TMAH and we land on the oxide layer on top. The final step in the processing involves the removal of Mo on top by H_2O_2. The device is shown in the picture 4.26.

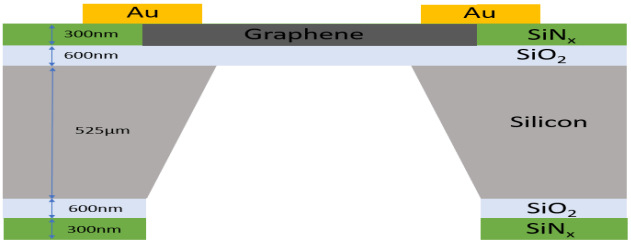

Figure 4.26: Graphene on a 600nm thick oxide structural membrane.

4.4. Measurement Structures

Specific structures were used to measure static electrical measurements. Kelvin-Cross structures were used to measure the contact resistance between graphene and Au and also, for the sheet resistance of graphene. These have been explained in the section below.

4.4.1. Kelvin Cross Structure for Contact Resistance

This structure resembles a cross with two of it's arms made up of Au and the other two made of graphene. They have the same length and width, hence, the area of contact is a square. Current is passed through arms I1 and I2 while the voltage is measured across V1 and V2 [61]. This is shown in the figure 4.28.

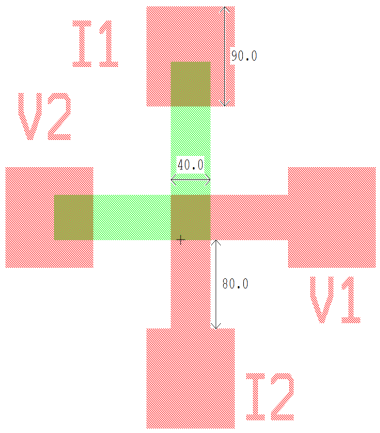

Figure 4.27: Kelvin Cross Structure for Contact Resistance.

The resistance R is given by

$$R = \frac{V_{1,2}}{I} \tag{4.5}$$

The specific contact resistance R_C between graphene and the metal is generally represented as $R * w$ or $R * A$. Where w is the width of the channel and A is the area of the channel. In the research work by K. Nagashio et al. [62], it was found that the value of $R_C * A$ increases for increase in area, while $R_C * w$ remains constant even for any variation in the area of contact. Hence, it can be assumed that the specific resistivity of graphene and metal contact ρ_c is a function of w. Hence, the specific contact resistance can be represented as

$$R_C = R * 4w(\Omega\mu m) \tag{4.6}$$

Where w is the width of the channel. In the above case, 4.28, w is $40\mu m$. In the above case, the conduction of current between graphene and the metal could occur at all the four edges. Hence, the width considered is $4w$.

4.4.2. Kelvin Cross Structure for Sheet Resistance

This sturcture resembles a cross with all of the arms of graphene. Current I is passed through arms I1 and I2 while the voltage is measured across V1 and V2.

The resistance R is given by

$$R = \frac{V_{1,2}}{I} \tag{4.7}$$

The sheet resistance R_S is given by

$$R_S = \frac{R\pi}{ln2} \tag{4.8}$$

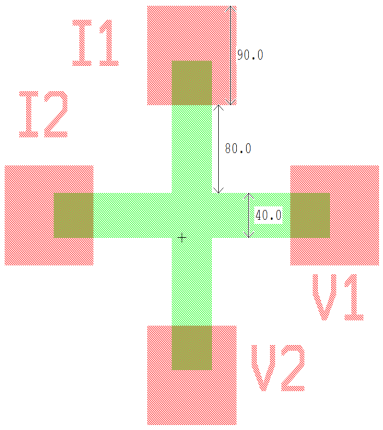

Figure 4.28: Kelvin Cross Structure for Contact Resistance.

4.4.3. TLM Structures for Sheet Resistance Measurement

This consists of a series of graphene structures with the same width but increasing length. Since for the same area and resitivity,the resistance R is directly proportional to the length of the graphene conductor. Hence a linear increase in the resistance is seen when the length also increases linearly. The structure is shown in the picture 4.29.

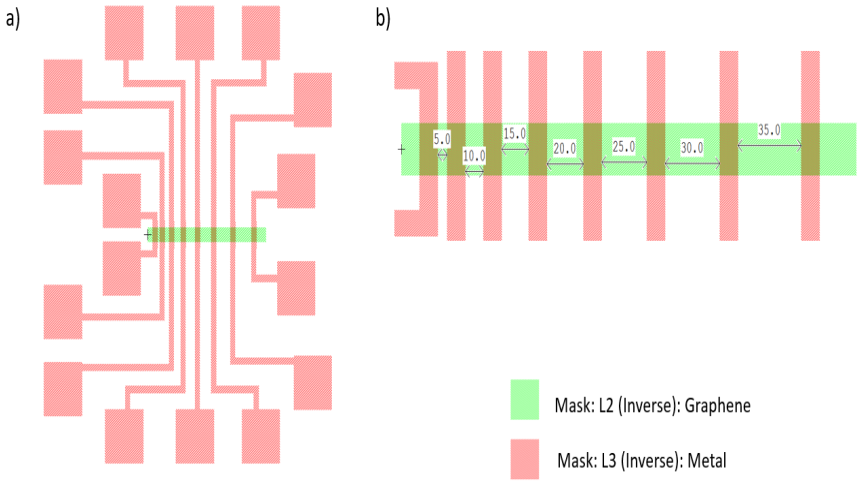

Figure 4.29: a) TLM Structure with the contact pads. b) The variation in length of the conductor.

The figure 4.30, shows the plot of the resistance as a function of the length. The slope of the line, is a function of the sheet resistance (R_S) of the graphene conductor. While the Y-intercept is a function of the specific contact resistance (R_C) of graphene and the metal interface.

The specific contact resistance R_C is expressed as

$$R_C = \frac{Y - intercept * w}{2} (\Omega \mu m) \tag{4.9}$$

Where, w is the width of the graphene conductor. Here, it is $30 \mu m$.

Likewise, the sheet resistance R_S is expressed as

$$R_S = Slope * w (\Omega / \square) \tag{4.10}$$

Where, w is the width of the graphene conductor. Here, it is $30 \mu m$.

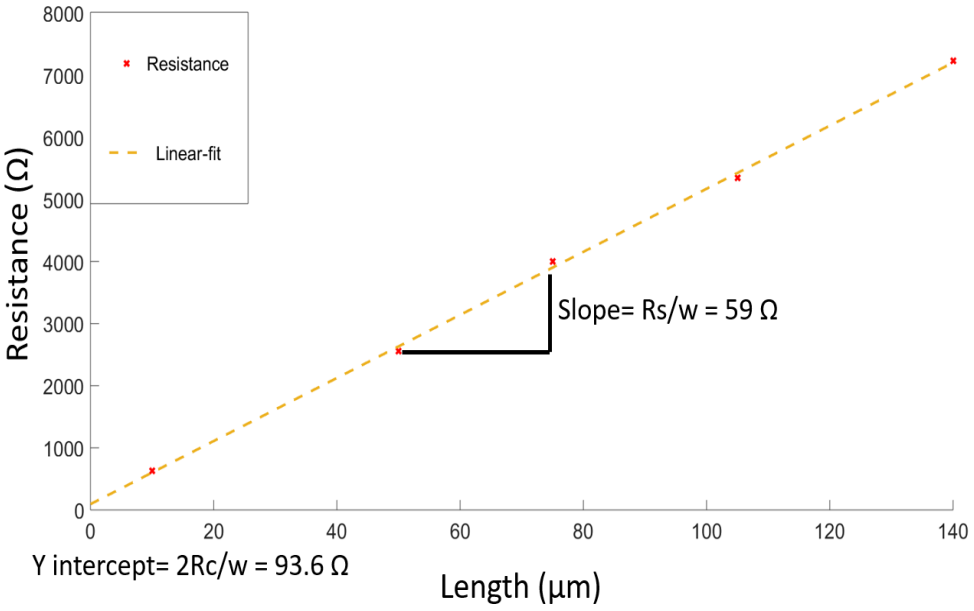

Figure 4.30: Plot of the Resitance as the function of the length of the graphene conductor.

4.5. Observations

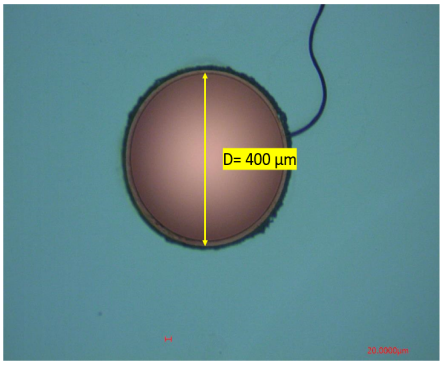

Figure 4.31: A hole in the bulk Si after DRIE.

In the above figure 4.31, the hole in the PECVD oxide is visible. Bulk Si was etched for 1.5 hours, and 6 μm of Si was removed (Section 4.3.3). The cracks in the oxide layer are also visible (due to thermal

stress during graphene growth).

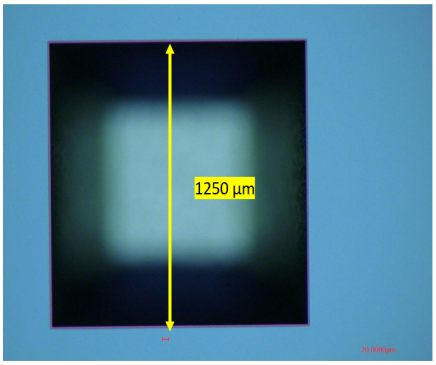

Figure 4.32: The back etch window opening in SiN_X.

In the above figure 4.32, the back opening in 500 nm thick SiN_X is visible (Section 4.3.1). This was later etched in KOH and landed on SiN_X on the front.

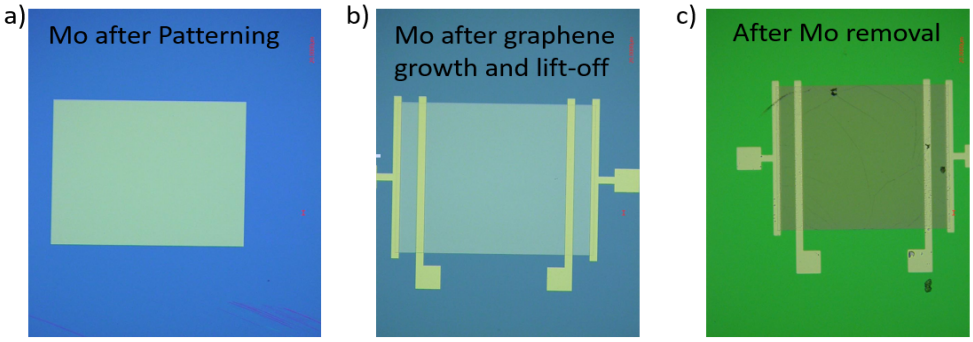

Figure 4.33: Different stages of processing.

The figure 4.33 represents a few of the processing stages. Figure 4.33 a shows the patterened Mo before graphene growth.Figure 4.33 b shows the device after graphne growth and lift-off. Figure 4.33 c shows the device after complete fabrication. After the removal of Mo, the membrane loses it's metallic color (seen in figure 4.33c).

4.6. Conclusions

Following the complete fabrication flow, a few observations were noted. The membranes are extremely delicate and can fracture easily. Also, the adhesion between Au electrodes and graphene is weak and it has to be made sure that some parts of the Au electrodes are in contact with the oxide or SiN_X underneath.

Also, while etching the hardmask from the back (Si_3N_4), a $3\mu m$ of photoresisit must be used. With $1.4\mu m$ photoresist, the etching was uneven.

In section 4.3.4, we make use of PECVD SiO of 6 μm thickness. After the growth of graphene, cracks were seen in the oxide layer and Mo layer. This indicates that there is a difference in the thermal co-efficient of expansion between Si and PECVD SiO.

Also, for the process step 4.3.3, the etch rate of PECVD SiN_X in vapor HF is very slow. Hence, it would be better to skip deposition of PECVD SiN_X completely as the $6\mu m$ on oxide on the top is quite sufficient as a stopping layer for DRIE.

Also, care must be taken to make sure that Mo is not contaminated before the growth of graphene. Photoresist or polymer residues on Mo can hamper the growth of graphene D.

Owing to many processing difficulties and time constraints, the process could only be completed for graphene with SiN_X (4.3.1).

5

Device Characterization

In this chapter, the Raman Spectroscopy of the graphene membranes will be discussed. The spectral data will be analyzed to assess the crystallinity of the graphene membranes. Further, TLM measurements were performed to determine the sheet resistance of graphene and the contact resistance between graphene and Au contact. Pressure dependent electrical measurements were performed and values were tabulated. Further, the Gauge Factor (G.F) of the devices were determined.

5.1. Raman Spectroscopy

To obtain the Raman Spectra of the graphene samples, we used a Renishaw inVia Reflex Spectrometer. A 633nm laser with back scattering was used. The laser power was kept at 5 mW and this was done to avoid damages to the graphene membrane.

A number of measurements were taken and to confirm the existance of graphene and also define it's quality [38]. This will be explained in detail in the following section

5.1.1. Different Graphene Growth Rates

The figure 5.1 shows the Raman Spectrum for graphene membranes grown at different times. Slight variation can be seen in the intensities of the peaks. Three measurements were done for each growth time and the mean value with deviation has been represented in the table 5.1.

Table 5.1: Analysis of Raman peaks for different growth rates.

Time (minutes)	I_D/I_G	I_{2D}/I_G	FWHM of I_{2D} (cm^{-1})
40	0.34(±0.09)	0.43(±0.03)	58.63(±5.07)
30	0.56(±0.04)	0.60(±0.03)	68.12(±2.89)
20	0.56(±0.06)	0.54(±0.06)	59.64(±1.81)
10	0.46(±0.03)	0.47(±0.02)	57.92(±5.61)

The ratio of intensities of peaks indicate the quality and also gives a rough estimate on the number of constituent layers. The ratio I_D/I_G refers to the disorder in the graphene layer. The disorder is due to atomic defects in the graphene layer that causes a deviation from the hexagonal structure and is also due to presence of contaminants like polymer residue [47]. In the above table 5.1, it can be seen that I_D/I_G varies between 0.34 (40 minutes) to 0.56 (30 minutes). While the value of 0.34 can be considered as a low defect membrane, the value of 0.56 is on the higher side of disorder. It

can also be seen that the growth time has no systemic influence on the disorder value.

The value I_{2D}/I_G can be seen as an rough estimate to the number of constituent layers in the graphene membrane. I_{2D}/I_G has a value greater than 1 for FLG (few-layer graphene) and has a value lesser than 1 for multi-layer graphene [39]. Howevever, as the number of layers increase, the intensity of the 2D peak (I_{2D}) decreases and becomes saturated beyond a certain number of layers and hence, multi-layer graphene cannot be characterized using I_{2D}/I_G.

However, in the work by Y. Hao et al., it was observed that the Full width at half maximum of the I_{2D} peak increases with increase in the number of layers [40]. Hence, the width of the 2D peak increases for increase in the number of layers. In their work, a 5 layer graphene had a FWHM of 66.1 ± 1.4. By comparison, the values mentioned in table 5.1 can represent a multi-layer graphene membrane.The slight variation in FWHM could be due to the smaller spot size of the laser than the area under measurement and also, slight non-uniformities could be present in the graphene membrane.

The figure 5.1 shows the graphical representation of the Raman Spectroscopy of one of the points.

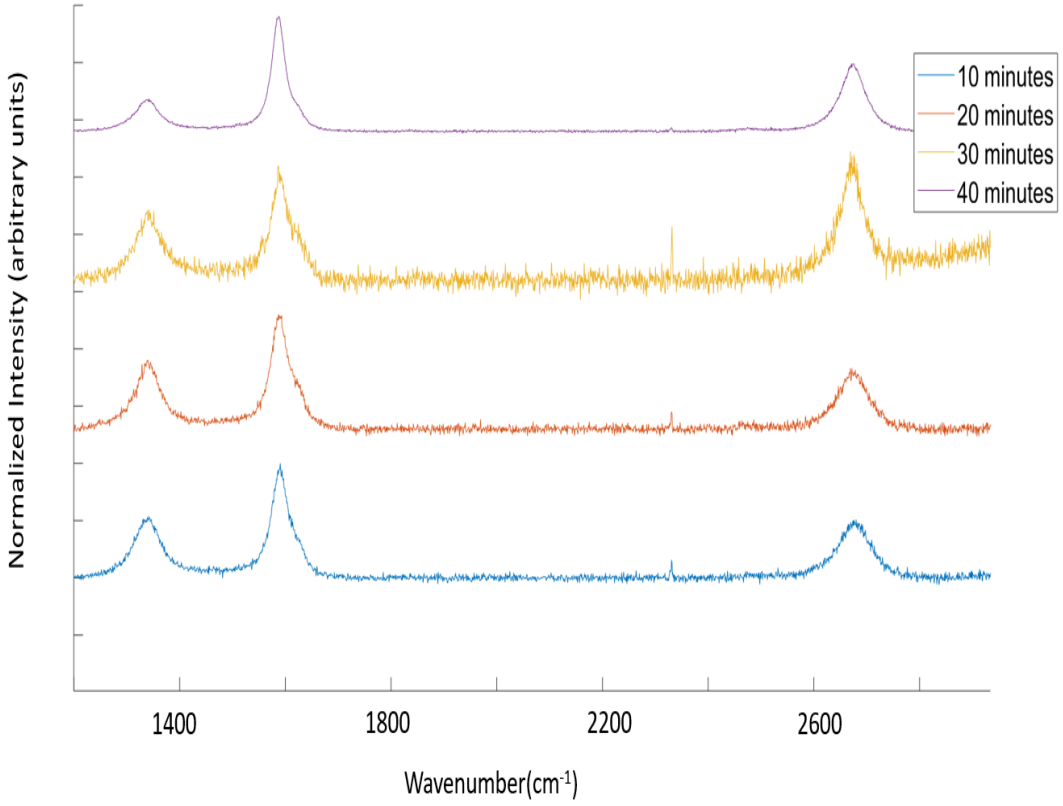

Figure 5.1: Raman Spectroscopy of graphene grown at different rates.

5.1.2. Analysis of the membrane quality after complete processing

The table 5.2 and the figure 5.3 represent the Raman spectra of the membranes as grown and after complete fabrication. Measurements were made at two distinct points and the mean value with deviation have been tabulated.

Table 5.2: Analysis of Raman peaks during processing.

Process Step	I_D/I_G	I_{2D}/I_G	FWHM of I_{2D} (cm^{-1})
As grown	0.45 (±0.005)	0.56 (±0.01)	67.18 (±6.43)
After complete fabrication	0.715 (±0.04)	0.60 (±0.03)	68.12 (±2.89)

It can be clearly seen that the disorder value (I_D/I_G) increases from 0.45 (as grown) to 0.715 (after complete fabrication) [47].

Since in our process flow, graphene undergoes a number of post processing steps with photoresist, there are high chances of contamination of the graphene membranes by photoresist. This can be a cause for increase in the value of disorder.

Also, graphite like substances are known to react with strong oxidizing agents like acids and H_2O_2. Due to the reaction, graphite-oxide is not only formed at the edges, but also at the graphitic planes [63]. in our process flow, H_2O_2 is used to remove Mo and during the process, graphene, in a few regions might have got oxidized and hence, we see a slight increase in the disorder value.

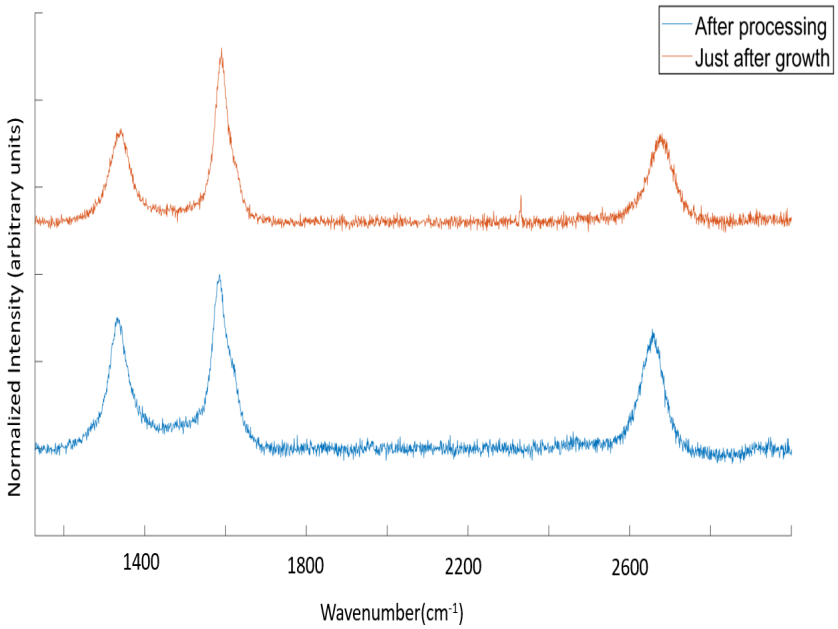

Figure 5.2: Raman spectra of the graphene membrane just after growth(red) and after complete fabrication(blue).

5.1.3. Uniformity of Growth

The figure 5.3 and the table 5.3 represent the Raman Spectra of the graphene membrane on different zones of the wafer.

The wafer was split into four quarters and measurements were performed at each of the quarter. The measurements performed as after grown. From the table 5.3, we can observe the disorder value i.e I_D/I_G to estimate the quality of the membrane at different parts of the wafer. The value is compara-

Table 5.3: Analysis of Raman peaks at different parts on the wafer.

Quarter	I_D/I_G	I_{2D}/I_G	FWHM of I_{2D} (cm^{-1})
1	0.54	0.55	76.25
2	0.52	0.54	83.60
3	0.49	0.53	81.26
4	0.52	0.97	67.23

tively even with mean of 0.54 and a deviation of 0.02. This means that the quality of the membrane is very similar through out the wafer.

The value of I_{2D}/I_G is lesser than 1 for all the measurements and this indicates the presence of multi-layer graphene. FWHM of I_{2D} has a mean value of 77.08 with a deviation of 6.27. This indicates that the graphene membrane is quite uniform in thickness across the whole wafer.

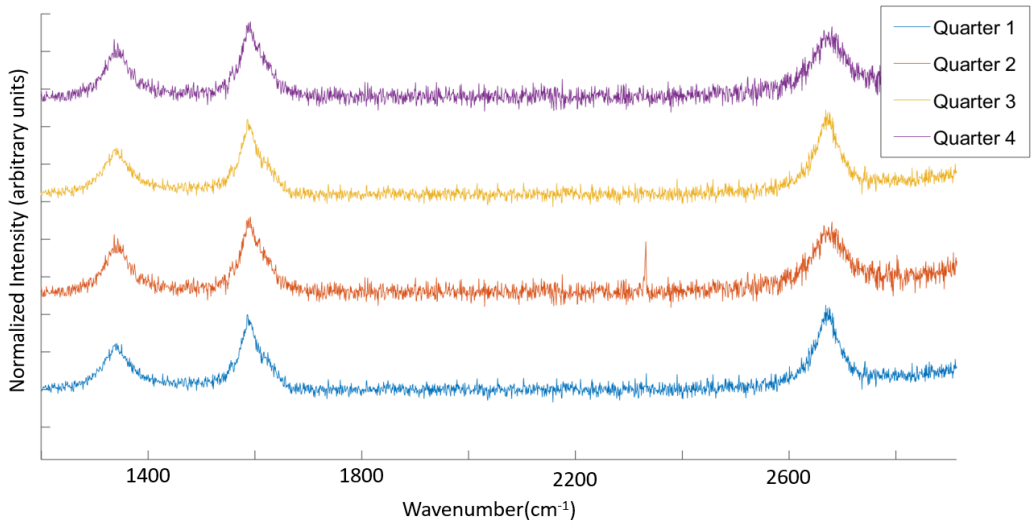

Figure 5.3: Raman Spectroscopy of different locations of graphene on the same wafer .

5.2. Pressure Measurement Setup

In order to test the membranes against a differential pressure, a custom-made setup was used . The setup consisted of a pressure redistribution chuck (designed by Dr. Jia Wei), vacuum pump and a pressure controller. The setup is shown in the figure 5.4.

The vacuum pump was connected to the sub-pressure controller. The pressure controller was used to set the amount of vacuum applied to the vacuum redistribution chuck. Using the vacuum redistribution chuck, we could apply vacuum to the backside of the devices leading to a maximum differential pressure of 90 kPa. The pressure at the membranes was indicated by the pressure controller.

The input vacuum was varied using the pressure controller and the electrical output was measured using a four-point probe.

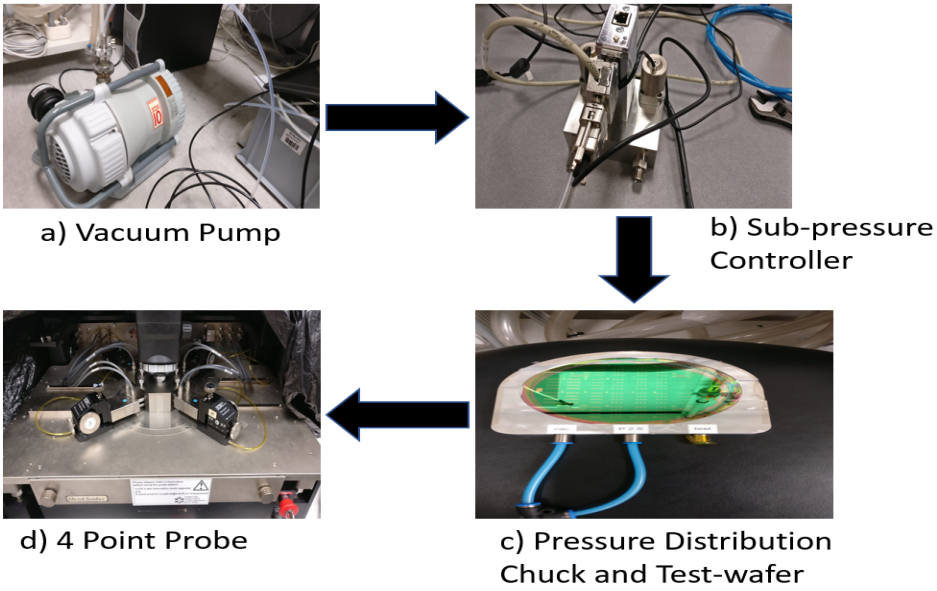

Figure 5.4: Graphical representation of the setup.

5.3. Optical Measurements

Optical characterization was performed using a KEYENCE laser scanning conformal microscope. The membranes were actuated by the pressure setup (fig 5.4) mentioned in the earlier section and 3-D analysis was performed on the actuated membranes. The profile of the membrane was reconstructed and the deflection for the applied differential pressure was measured. This will be explained in the section below.

5.3.1. Top-View of the Final Device

The figure 5.5 shows the top-view of the final device. The black square is the suspended membrane. The Au electrodes and the graphene layer are visible.

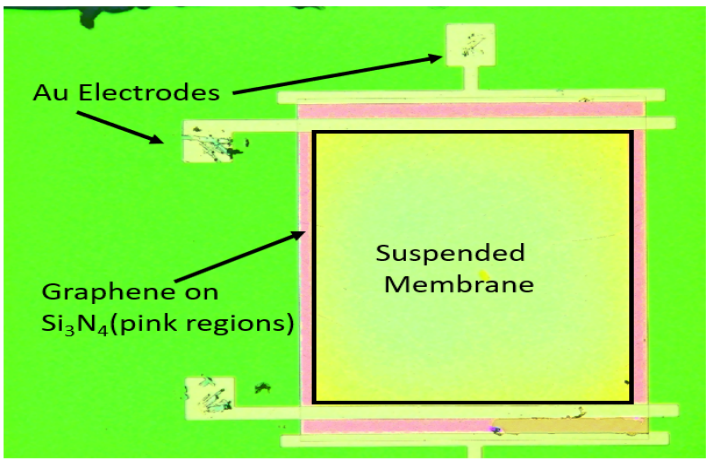

Figure 5.5: The top view of the device.

5.3.2. Profile Characterization

The membranes were actuated by the pressure controller and the pressure below the membranes was decreased from 100 kPa (atmospheric) to 20 kPa in steps of 10 kPa. Profile measurements were made at each pressure step and the corresponding deflections are noted. This is shown in the figure 5.6.

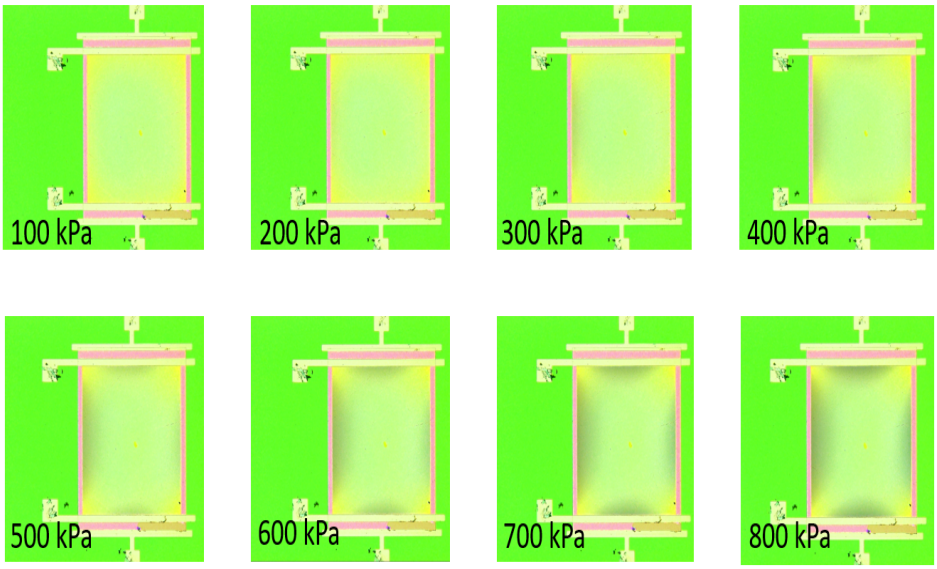

Figure 5.6: Visual changes in the membrane for different differential pressures.

In the figure 5.6, as the differential pressure across the membrane increases, certain regions of the membrane get deformed and hence are slightly out of focus and it causes a color shift. The color shift is easily seen for the increase in differential pressure.

5.3.3. Deflection of the Membranes

The deflection of the membrane increased with the increase in differential pressure. The same has been tabulated below (table 5.4). The measurements were performed on membranes having a side length of 575μm and the thickness of Si_3N_4 was 300 nm.

Table 5.4: Measured deflection of the membrane as a function of the applied pressure.

Applied Pressure (kPa)	Deflection (μm)
10	4.142
20	7.018
30	8.882
40	10.605
50	12.146
60	13.468
70	14.379
80	15.275

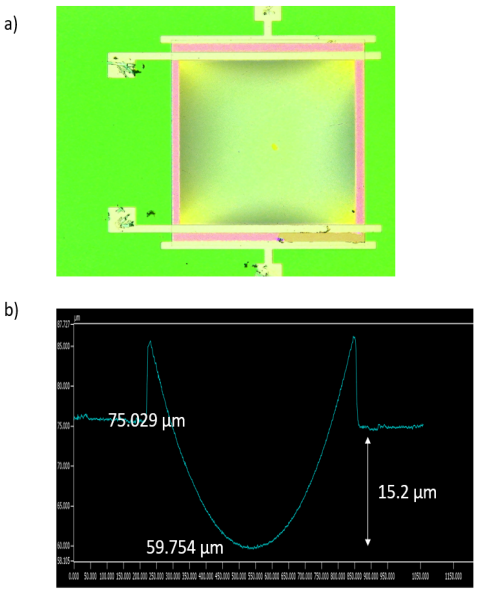

Figure 5.7: The optical and graphical presentation of the profile of the membrane at a differential pressure of 80 kPa.

Figure 5.7 represents the optical and the graphical profile of the deflected membrane for an applied pressure of 80 kPa. In the graph, 5.7b, we can see that the out of plane deflection (centre of the membrane) is 15.275 μm.

5.3.4. Data-fit using Comsol

In order to determine the average strain of the membrane due to the out of plane deflection, we used a *Comsol* model with similar deflection profile. However, the simulation performed with the assumed parameters of the membrane produced less deviation for the same value of applied pressure than the one that was measured. Hence, by taking references from previous work done at EKL on Si_XN_X membranes [53], new values for *Young's Modulus* and *Poisson's Ratio* were chosen.

However, we see a slight deviation of values between the simulation model and the actual measurement below an applied differential pressure of 40 kPa. This is due to the offset due to initial stress in the Si_XN_X membrane. At a differential pressure of 80 kPa, the deflection profile of model fits the measured data perfectly and hence, the strain used for further calculation, is referred to the value of strain achieved at 80 kPa in the simulation model.

The modified properties are mention in the table 5.5.

Table 5.5: Variation in the properties of the material to fit the measured deflection profile.

Property	Assumed Value	New Value
Young's Modulus	200 GPa	190 GPa
Thickness	300 nm	280 nm
Poisson's Ratio	0.22	0.20

Using the simulation environment, the average strain across the whole range of the applied differential pressure was calculated. At a differential pressure of 80 kPa, the membrane has an average strain of 0.00162. The measurements are tabulated below (table 5.6).

Table 5.6: Average strain of the membrane as a function of the applied differential pressure.

Pressure (kPa)	Average Strain
10	0.000383
20	0.000625
30	0.000829
40	0.00101
50	0.00117
60	0.00133
70	0.00148
80	0.00162

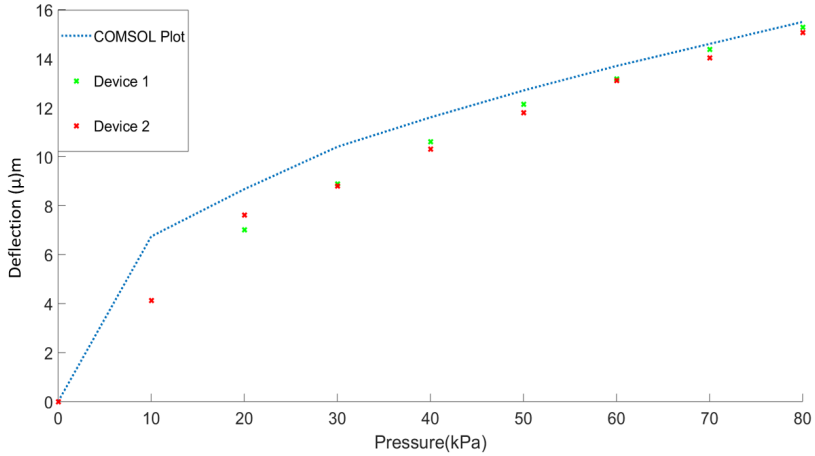

Figure 5.8: Comsol model built using the deflection profile of the membranes.

5.4. TLM Measurements

TLM measurements are used to map the sheet resistance of graphene and the contact resistance of Au and graphene. The measurements are performed as a function of length and since resistance is a linear function of length, a liner-fit is then performed on the plot. The slope gives the sheet resistance and the Y intercept gives the contact resistance R_C [64].

5.4.1. Calculation of R_C and R_S from the plot.

The length v/s resistance plot is shown in the figure 5.9. For *measurement a*, the the slope is 59 $\Omega/\mu m$ and the Y intercept is 94 Ω.
Solving this, we get

$$R_S = slope * w(\Omega/\square) \tag{5.1}$$

Where w is the width of the channel = $30\mu m$

$$R_S = 59 * 30\mu m = 1770\Omega/\square \tag{5.2}$$

Similarly,

$$R_C = 94/2 = 47\Omega \tag{5.3}$$

Also, R_C can be expressed as

$$R_C = 47\Omega * 30\mu m = 1410\Omega\mu m \tag{5.4}$$

Where w is the width of the channel and is equal to $30\mu m$.
By applying equation 5.1 and 5.4 to the data from measurements *b* and *c*, the values of R_C and R_S are calculated. The same has been tabulated below (5.7).

Table 5.7: Contact and Sheet Resistance from TLM measurement.

Measurement	Slope (k$\Omega/\mu m$)	Y-Intercept (Ω)	R_S (Ω/sq)	R_C (Ω)
1	59	93.6	1.77	47 Ω (1.41 k$\Omega\mu m$)
2	130	567	3.9	283.5 (8.50 k$\Omega\mu m$)
3	47.61	979	1.42	489.5 (14.68 k$\Omega\mu m$)

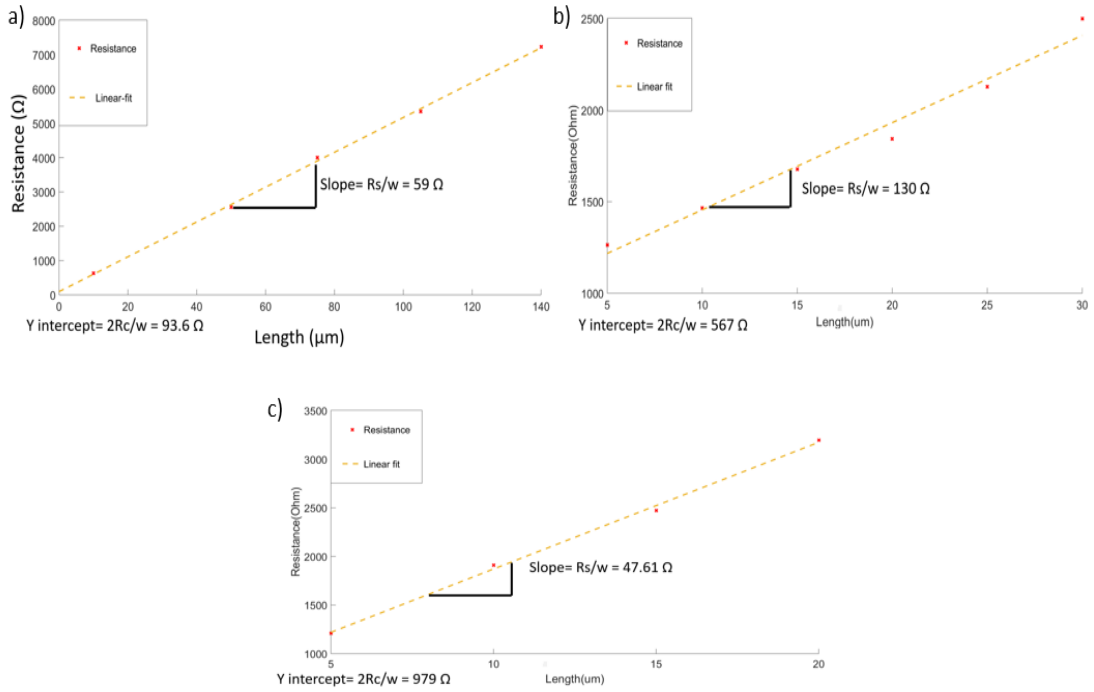

Figure 5.9: Resistance as a function of the varying length of the graphene conductor.

- Measurement A: The plot is shown in figure 5.9 and the values are tabulated in table 5.7. The value of R_C and R_S are similar to the values reported in literature [65].
- Measurement B: Here, the values of both R_C and R_S are on the higher side. The higher value of sheet resistance could be due to defects in the graphene membrane or can also be due to an improper contact with the electrodes due to defects [48].
- Measurement C: The value of both R_C is on the higher side. This might be due to improper contact between the electrode and graphene. Also, the type of deposition (evaporation) might have an impact on the contact resistance [64].

5.5. Pressure Dependent Measurements

Since our aim is to develop a graphene based differential pressure sensor, we need to measure the change in the electrical properties of the membrane as a function of the applied differential pressure. In earlier chapters, we have mentioned about the piezoresistive properties of graphene and how it's resistance changes due to strain. In our device, the applied differential pressure causes the membrane to deflect away from the plane. This causes strain in the membrane and hence, we see a change in the resistance.

To achieve this, the pressure actuation setup was used and the four-point measurement was performed using the wafer probing tool by Cascade Microtech. The membranes were actuated by the pressure controller and the pressure below the membranes was decreased from 100 kPa (atmospheric) to 20 kPa in steps of 10 kPa. At each step, a four-point measurement was performed and the voltage drop across the membrane and the current through the membrane was noted. The values were then plotted, followed by a linear fit which gave the values of the corresponding resistances.

Table 5.8: Design parameters of measured devices

Property	Value
Side length	575 μm
Thickness of SiN_X	300 nm
Graphene growth time	20 minutes
Temperature	Room (23 °C)

5.5.1. Measurement Results

The measurement was performed on four functional devices from -1.5 V to 1.5 V with 51 steps in between. The membranes were actuated by the pressure controller and the pressure below the membranes was decreased from 100 kPa(atmospheric) to 20 kPa in steps of 10 kPa. Hence, the dynamic range was from 0 kPa to 80 kPa of differential pressure. However, for device 2, the measurement was done for a dynamic range of 0 - 70 kPa of differential pressure.

The figure 5.10 shows the value of the resistance as a function of the applied pressure. The corresponding have been tabulated in the table 5.9.

Device 1

In the current device, the resistance changes from 1491Ω at 0 kPa of differential pressure to 1497 Ω at a differential pressure of 80 kPa. Hence, the change is resistance is 6 Ω. Also, ΔR/R is equal to 0.00402.

Also, the response of the device is linear as a function of the applied pressure. This gives us a sensitivity of $0.075\Omega/kPa$.

Device 2

The resistance of the membrane changes from 1.354 $k\Omega$ to 1.3588 $k\Omega$. This gives a change in resistance of 4.4Ω for a dynamic pressure range of 80 kPa. The sensitivity is 0.062 Ω/kPa. The change in resistance for the device is linear as a function of the applied differential pressure.

Device 3

This device shows a very steep change in the value of resistance for the extreme value of the applied differential pressure, i.e for 0 kPa and 80 kPa of differential pressure respectively. For a differential

Table 5.9: The resistance values of the devices for corresponding differential pressure across them.

Pressure (kPa)	Device 1 (Resistance Ω)	Device 2 (Resistance Ω)	Device 3 (Resistance Ω)	Device 4 (Resistance Ω)
0	1491	1354.4	1458.2	1463
10	1491	1355.6	1459.5	1463.6
20	1491.4	1356.2	1463	1464
30	1492.8	1357.0	1463.5	1464
40	1493.5	1357.6	1464	1466
50	1493.5	1357.6	1464.4	1465.8
60	1494.2	1358.6	1464.6	1467.2
70	1496.3	1359.0	1464.9	1467.8
80	1497	-	1467.8	1468.2

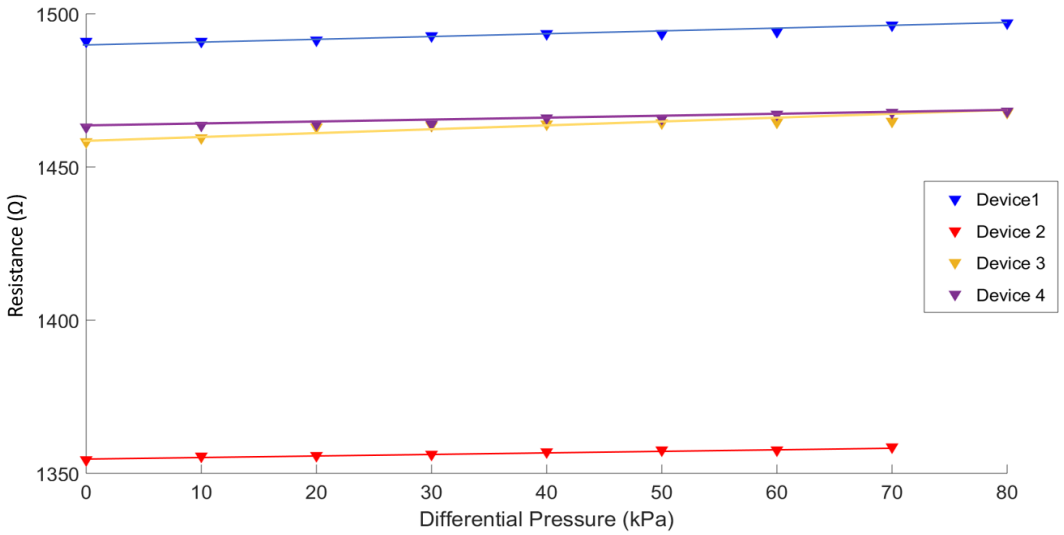

Figure 5.10: Resistance as a function of the applied differential pressure.

pressure of 10 kPa, the device has a resistance of 1459.5 Ω, while at 30 kPa, the resistance changes to 1463 Ω. This is a very large change in the value of resistance considering the change in the applied differential pressure. Also, for the change in the differential pressure from 30 kPa to 70 kPa, the resistance only changes by 1.9 Ω. This behaviour is non-linear and would not be suitable as an effective pressure sensor. This non-linearity could be due to oscillations in the membrane which could be caused by improper application of vacuum. The first eigen value of resonance is at 44 kHz, with a displacement of 4.5 μm.
Since, the electrical properties of graphene and the properties of graphene-Au contact are effected by variations in temperature, humidity and absorbance of gases [66], these could also be the cause for this non-linear behaviour . However, the device has a change in resistance of 9.6 Ω for the change in applied deifferential pressure from 0 to 80 kPa. This gives us a sensitivity of 0.12 Ω/kPa.

Device 4

This change in resistance of the device as function of the applied differential pressure was linear. The resistance was 1463 Ω at 0 kPa and at 80 kPa, the resistance increased to 1468.2 Ω. The sensitivity of the device is 0.065 Ω/kPa.

5.6. Gauge Factor

Gauge Factor (GF) is the ratio of normalized change in resistance to strain.

$$GF = \frac{\Delta R/R}{\epsilon} \tag{5.5}$$

Where ϵ is the strain.

From the section, 5.3.4 and 5.5, we can calculate the gauge factor for the devices. For this calculation, we have considered the maximum change in resistance to the corresponding value of average strain. The same has been tabulated below for different devices.

Table 5.10: Calculation of Gauge Factor.

Device	Average Strain	Normalized change in Resistance (ΔR/R)	Gauge Factor (GF)
1	0.00162	$4.024 * 10^{-3}$	2.48
2	0.00148	$3.54 * 10^{-3}$	2.39
3	0.00162	$6.5 * 10^{-3}$	4.06
4	0.00162	$3.54 * 10^{-3}$	2.19

5.6.1. Comparison with State of the Art

As mentioned in Chapter 2, the state of the art in graphene-based piezoresistive pressure sensor uses transferred graphene on thin dielectric substrates which are used as the mechanical support layer. In our device, we have eliminated the transfer process and graphene is grown directly on the mechanical support layer. However, after growth, graphene underwent multiple post-processing steps which could cause potential contaminants in the membrane and could hamper the properties of the device. After the characterization of the device, even though there was an increase in disorder of the graphene membrane, it's effect on the device performance was minimal. The gauge factor derived was in line with the simulations and theory. Also, the gauge factor is comparable to the ones reported in the literature. The same has been tabulated below (5.11).

Table 5.11: Comparison of the device with the state of the art.

Device	Thickness of Support Layer (nm)	Device Dimensions (μm)	Gauge Factor	Dynamic Range (kPa)
Transferred graphene on SiN_X [1]	100	280	1.6	0 - 70
Transferred graphene on perforated SiN_X [2]	200	490	4.4	0 - 60
Our Device	300	575	Max of 4.06 Mean of 2.80	0 - 80

From table 5.11, we can see that our device has a a better gauge factor than transferred graphene on SiN_X and has the maximum dynamic range. The the gauge factor of the device can be increased by decreasing the thickness of the mechanical support layer. In our research we had included devices with thinner mechanical support layer (100 nm), but unfortunately, due to processing hardships,

the devices were never realized.

5.6.2. Self-Heating of Membranes

Wrinkles and grain boundaries in CVD graphene are known to cause localize heating. Also, doping of graphene from contacts can lead to non uniform resistance and hence can be a cause for localized heating too [48].

In the figure 5.11, the resistance plotted against three input voltages. We can observe that for input voltage V_{in}, (-1 V < V_{in} < 1 V), the resistance remains fairly constant. For input voltage V_in greater than |2.5 V|, the resistance slightly decreases. This can be explained due to Joule Heating of the membrane. According to Joule's law, the power dissipated in a resistor is proportional to I^2, where I is the current flowing in the conductor.

In graphene, the rise in temperature is directly proportional to V_{in}^2 where V_{in} is the applied voltage. Hence, at higher input voltages, the temperature of the graphene film increases [67]. This is due to increase in phonon scattering of electrons. Graphene is known to have a negative temperature co-efficient of resistance [68]. Hence, at higher voltages, the temperature of the film increases and due to the negative temperature co-efficient, the value of the resistance decreases.

Keeping this in mind, the input voltage applied to the membrane must be lesser than 2 V to minimize the effects of self-heating. However, if the if the voltage is kept too low, SNR will also get reduced and it will be very difficult to separate the main signal from noise. Hence, the devices were tested till an input voltage of 1.5 V.

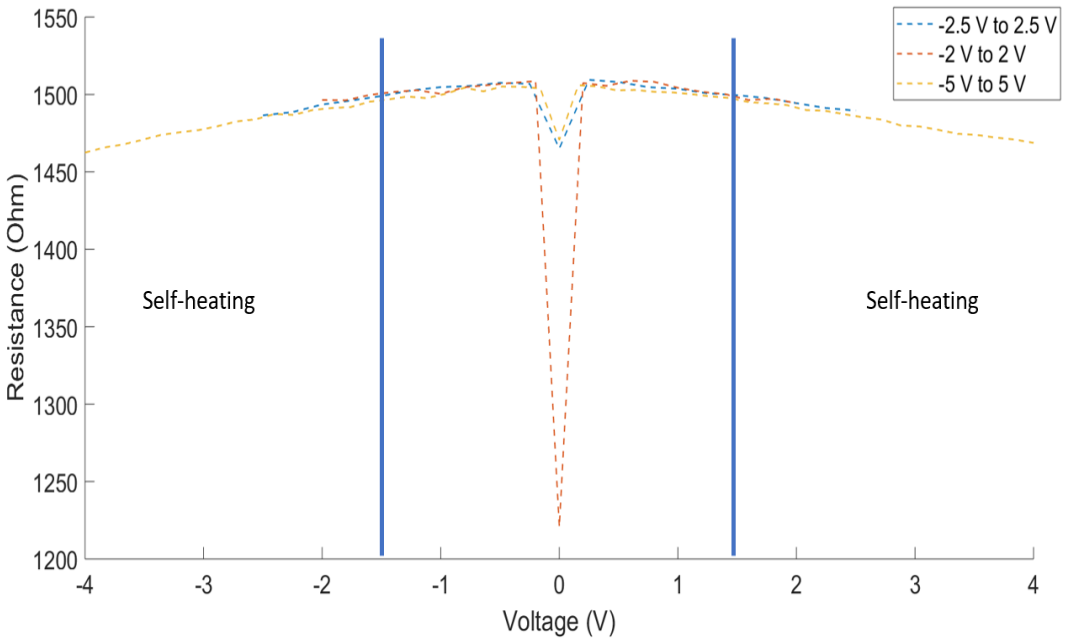

Figure 5.11: Self-heating in graphene membranes.

5.6.3. Schottky Like Contact Behaviour

An ideal ohmic contact has a linear I-V behaviour and this means that the resistance remains constant for the whole range of the applied voltage. Generally, a conductor to a conductor contact is Ohmic, where as a semiconductor to a metal (n^+ to metal) is non-ohmic or Schottky.

Graphene is known to behave like a semi-metal. When a metal is deposited on graphene, due to the differences in their work function, a charge transfer happens between them. This causes slight electrical doping of graphene. The direction of the charge transfer depends on the differences in the work function between graphene and the metal contact. Also, at the metal graphene interface, the Fermi level E_F is fixed by the metal and for graphene away from the metal, E_F would be at Dirac point. Hence, a slight charge transfer occurs between the two graphene regions and this gives rise to band bending [64]. Also, graphene being a 2-D material, can be very sensitive to changes in the environment and this can give rise to changes in the electrical property [64].

These characteristics might make graphene-metal contact behave slightly non-linear. In this case (figure 5.12), the I-V curve is not linear for V (-0.5 < 0.5).

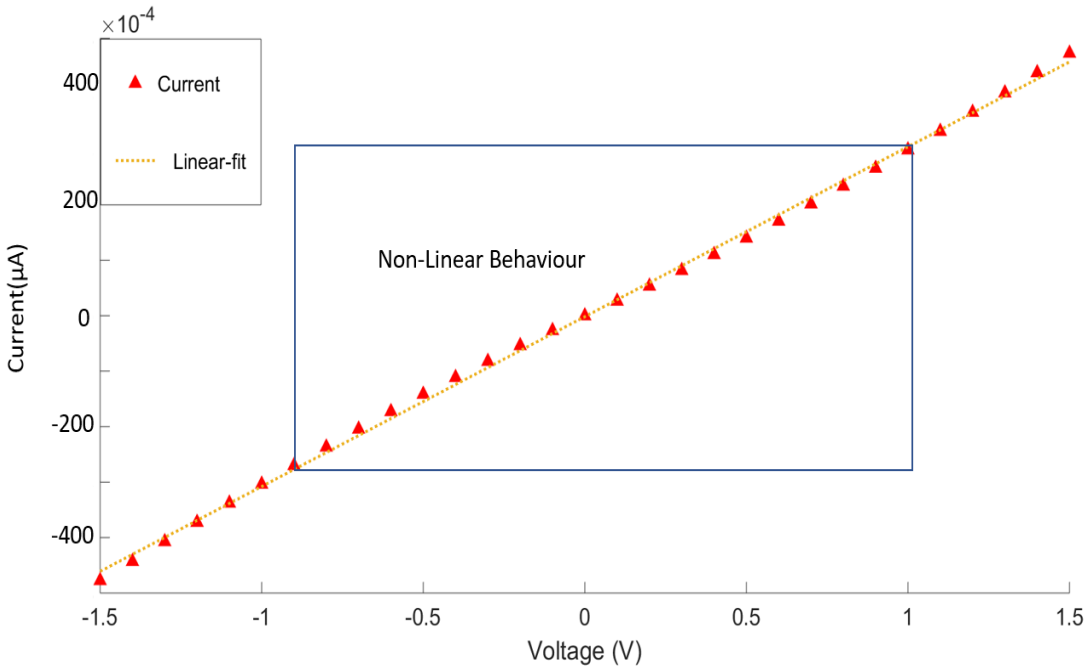

Figure 5.12: Non-linear I-V behaviour of graphene-Au contact.

5.7. Conclusion

In the previous sections, Raman spectroscopy, optical and electrical characterization of the transfer-free graphene-based pressure sensors are discussed in detail. From the measurement results, we can concur that the devices are indeed responding to the change in differential pressure applied across them.

5.7.1. Raman Spectral Analysis

Multiple Raman spectrscopy for graphene was performed and we saw a minimal rise in the disorder value, I_D/I_G for Raman spectra done on graphene as on growth and after complete fabrication (an increase of 0.3).

5.7.2. Contact and Sheet Resistance

Also, from the TLM measurements, the contact resistance R_C and the sheet resistance of graphene, R_S was calculated. The same has been tablulated below (table 5.12).

Table 5.12: Sheet Resistance and Contact Resistance measured from TLM structures.

Device	Slope	Y intercept	Sheet Resistance R_S (kΩ/sq)	Contact Resistance R_C (Ω)
1	59	93.6	1.770	46.8 Ω or 1.4 kΩμm
2	130	567	3.99	283.5 Ω or 8.5 kΩμm
3	47.61	979	1.428	489.5 Ω or 14.68 kΩμm

The first measurement has R_C and R_S similar to the values reported in literature [64]. However, in the other two cases, the values are on the higher side. This could be due to the sensitivities of graphene-Au contact on parameters like temperature and humidity, or also can be due to an improper contact between graphene and Au.

From the measurement results, the contact also exhibited Schottky like behaviour (non-ohmic) for low applied voltages and could be due to doping of graphene by impurities or also could be due to an improper contact between Au and graphene.

Graphene membrane exhibited self-heating at high applied voltages (v > 1.5 V) and this causes reduction in resistance at those values. Due to this, the I-V behaviour can be described as non-linear. This can be minimized by restricting the applied voltage to a maximum of 1 V, but, the signal-to-noise ratio will be low and it would be very difficult to distinguish the signal from actual noise. Hence, as a compromise between non-linearity and low SNR, an input voltage range of maximum of 1.5 V was chosen. The response of the device was almost linear and there was minimal noise.

5.7.3. Gauge Factor

The average gauge factor of the devices was 2.80, with a deviation of 0.7. The maximum Gauge Factor achieved was 4.06 and this comparable to the values in the literature. The dynamic range of 0 - 80 kPa is the highest in comparison to the literature 5.11.

The table (5.11) shows that transfer-free graphene processing can be employed to make graphene-based pressure sensors with similar performance to transferred graphene pressure sensors.

6

Conclusion

In this section, a complete overview of the this research work will be discussed, followed by future work and recommendations.

6.1. Summary of the research work

- Firstly, a literature review was performed to assess the possibility of having graphene-based pressure sensors. Graphene has a high potential piezoresistive Gauge Factor of 15000 [26], and combined with it's mechanical properties, it is an ideal candidate for pressure sensing. Owing to issues like polymer contamination and strain induced wrinkles caused by the transfer-process, we decided to employ a novel transfer-free [11] approach to realize the devices.

- A simulation model was built for the device after taking cues from the literature. The model was validated by comparing the results of the simulation to manual calculations and the literature. In the simulation, the transfer-free graphene on 100 nm SiN_X showed better performance than the state of the art 3.8. Free-standing graphene membranes produce 40% more strain than graphene on a SiN_X support membrane. Hence, devices with free-standing graphene membranes will have far superior performance (3.17).

- This was followed by Mask design and formulating the flow-chart. Due to time constraints and other processing difficulties, only devices with transfer-free graphene on SiN_X could be realized.

- Further, Raman Spectral analysis showed minimal effects of post processing on the graphene membranes (ref table5.2). Using TLM, the specific contact resistance was found to be 1.5 k$\Omega\mu m$ and the sheet resistance was 1.7 k$\Omega/\square$. This was in line with the values mentioned in the literature ([64], [33]). The gauge was calculated to be 2.8 (with a maximum of 4.06).

6.2. Research Objectives Achieved

In this research work, we have successfully integrated transfer-free graphene processing into semiconductor bulk micromachining and through this, we have fabricated world's first transfer-free graphene based differential pressure sensor.

Further, the devices were characterized through Raman spectroscopy and pressure dependent electrical characterisation. The analysis of the Raman shift revealed that graphene membrane under-

went minimal changes during the post growth processing steps.

Pressure dependent electrical characterization was performed on the device over a dynamic range of 0 to 80 kPa. The devices have an average **Gauge Factor (G.F) of 2.8**, with a deviation of 0.7. The value is better than most reported in the literature, however, one device achieved a **Gauge Factor 0f 4.06** which is very close to the highest value (4.4) of G.F reported in the literature 5.11.

The devices have a dynamic range of **0 to 80 kPa**, which is the **highest** amongst the values reported in the literature 5.11.

With this, we have resolved our problem statement and have reached most of our research goals, but unfortunately, we couldn't realize free-standing graphene-based differential pressure sensor. Even though, the design parameters were derived keeping the restraints that free-standing graphene carries, we were not able to complete the processing. Free-standing graphene membranes are extermely delicate and in CVD graphene, due to the presence of inherit defects, it is very difficult for the membranes to survive the standard processing steps.

6.3. Recommendations and Future Work

- The Mo catalyst must be kept free from oxidation before graphene growth. Oxidation could result in surface unevenness and graphene so grown will be high in defects and the properties would resemble amorphous Carbon than graphene. This could be due to surface unevenness of Mo due to oxidation (ref D).

- Also, while using plasma etching for the opening of the backside window in SiN_X, the minimum thickness of photoresist should be 3.1μm. Else, it will result in uneven etching.

- The Cr/Au depositon must be done under stable vacuum conditions. Else, the depositon will be uneven and may cause adhesion issues with graphene.

- In the section 4.3.3, cracks were seen on the PECVD SiO (and on Mo) after graphene growth. This might be due to variations in thermal expansion between Si and the PECVD Sio. To prevent this, parameters (pressure, tempreature and reactant gases) of the PECVD should be varied to achieve a layer with a thermal co-efficient of expansion similar to Si.

- In the section 4.3.3, the PECVD deposition of SiN_X can be skipped. The 6 μm of SiO is sufficient as a stopping layer for DRIE.

- Thinner SiN_X (<100 nm) support membranes can be used to achieve devices with higher Gauge Factor.

- The work can be extended further to achieve graphene-based differential pressure sensors having *SiC* support membranes. *SiC* is known be very stable at elevated temperatures and this can give way to transfer-free graphene-based sensors for applications in high temperatures.

- During the measurements, substantial reduction in the resistance of graphene was seen at high input voltages. This is due to Joule heating and negative TCR of graphene. Hence, the potential of having a transfer-free graphene based temperature sensor can be explored.
- This work can be further extended to realize transfer-free free-standing graphene-based differential pressure sensors.

A

Process Flows

A.1. Transfer-free Graphene on SiN_X

1. Start with 4-inch DSP wafer.
2. Creatio of Zero Layers (with alignment markers).
   (a) Spincoat 1.4 μm of SPR 3012, and perform a bake.
   (b) Expose the wafers on PAS 5500/80 automatic waferstepper. Use recipe "ZEFWAM" and set the exposure energy to 120 mj/cm^2. Mask: COMURK.
   (c) Develop the wafers on EVG 122. Use MF322 developer. Recipe: DEV-1SP
   (d) Performan inspection and check for the line width.
   (e) Plasma Etch the wafer using Trikon Omega 201 Plasma etcher. Run the recipe URK_NPD.
3. Cleaning of the wafers
   (a) Use the Tepla plasma system to remove the photoresist in an oxygen plasma.
   (b) 10 minutes in 100% nitric acid.
   (c) Rinse in the Quick Dump Rinser with the standard program until the resistivity is 5 MΩ.
   (d) 10 minutes in fumng nitric acid (65%) at 110°C.
   (e) Rinse in the Quick Dump Rinser with the standard program until the resistivity is 5 MΩ.
   (f) Dry the wafers.
4. Oxidation
   (a) Oxidation: for 600 nm of oxide, Use wet oxidation at 1100°C for 42 minutes.
   (b) Measure the oxide thickness using Leitz MPV-SP.
5. LPCVD Nitride
   (a) For 300 nm of SiN_X,use the recipe *4inchst* and set the time to 42 minutes.
   (b) Model the layer thickness using Woollam Ellipsometer.
6. Opening of windows in the SiN_X on the back side
   (a) Spincoat 3.1 μm of SPR 3012, and perform a bake.

(b) Perform the exposure on the EVG 420. Expose for a time equivalent to 240 mj/cm^2. Use the mask layer-1: Back-etch.

(c) Develop the wafers on EVG 122. Use MF322 developer. Recipe: DEV-1SP

(d) Perform an inspection and check for the line width.

(e) Plasma Etch the wafer using DRYTEK. Run the recipe *Stdsin* for 75 seconds.

7. Clean the wafers. As mentioned in step 3.

8. Catalyst depostion and patterning

(a) Use the *Trikon Sigma* sputter coater for the deposition of the catalyst Mo layer on the process wafers.Use the recipe *Mo_50nm_50c*.

(b) Coat the wafer with 1.4 μm of SPR 3012.

(c) Expose it on EVG 420 for a time equivalent of 55 mj/cm^2. Use the mask, Layer: Mo catalyst.

(d) Develop the wafers an inspect for the structures.

(e) Plasma Etch the wafer using Trikon Omega 201 Plasma etcher. Run the recipe *MO_test2*

9. Strip the photoresist on Tepla. Use program 1.

10. Graphene Growth

(a) Grow graphene on the wafer using AIXTRON Blackmagic. Use the reipe *Mo_NEW_915C_20min*. Also, run the recipe for 10, 30 and40 minutes.

(b) Perform a Raman Spectroscopy to analyze the quality or graphene.

11. Metal Evaporation

(a) Perform a manual coating of nLOF 2020. Deposit a layer of 3 μm..

(b) Expose the wafers using EVG 420. Expose for a time equivalent of 55 mj/cm^2. Use the mask, Layer: Metal.

(c) Develop the wafers manually. Use MF 322 developer.

(d) Inspect the wafers for line width.

(e) Use CHA to evaporate the metal on the wafer. First evaporate 10nm of Cr followed by 100 nm of Au.

12. Lift-off

(a) Use NMP at 70 °C in an ultrasonic bath for 5 minutes.

(b) Rinse in water and dry the wafers.

13. Wet Etching of bulk Silicon

(a) Wet etch the oxide on back using BOE (1:7) for 10 minutes and use the holder for front side protection.

(b) Set the KOH bath to 90°C and etch he wafers for 5 hours. Do inspections in between to check the rate of etching.

(c) Wet etch the oxide on front using BOE (1:7) for 10 minutes.

(d) Etch the Mo on the front side using H_2O_2.

A.2. Transfer-free Free-Standing Graphene

1. Start with 4-inch DSP wafer.
2. Creatio of Zero Layers (with alignment markers).
   (a) Spincoat 1.4 μm of SPR 3012, and perform a bake.
   (b) Expose the wafers on PAS 5500/80 automatic waferstepper. Use recipe "ZEFWAM" and set the exposure energy to 120 mj/cm^2. Mask: COMURK.
   (c) Develop the wafers on EVG 122. Use MF322 developer. Recipe: DEV-1SP
   (d) Performan inspection and check for the line width.
   (e) Plasma Etch the wafer using Trikon Omega 201 Plasma etcher. Run the recipe URK_NPD.
3. Cleaning of the wafers
   (a) Use the Tepla plasma system to remove the photoresist in an oxygen plasma.
   (b) 10 minutes in 100% nitric acid.
   (c) Rinse in the Quick Dump Rinser with the standard program until the resistivity is 5 MΩ.
   (d) 10 minutes in fumng nitric acid (65%) at 110°C.
   (e) Rinse in the Quick Dump Rinser with the standard program until the resistivity is 5 MΩ.
   (f) Dry the wafers.
4. Oxidation
   (a) Oxidation: for 600 nm of oxide, Use wet oxidation at 1100°C for 42 minutes.
   (b) Measure the oxide thickness using Leitz MPV-SP.
5. LPCVD Nitride
   (a) For 300 nm of SiN_X,use the recipe *4inchst* and set the time to 42 minutes.
   (b) Model the layer thickness using Woollam Ellipsometer.
6. Opening of windows in the SiN_X on the back side
   (a) Spincoat 3.1 μm of SPR 3012, and perform a bake.
   (b) Perform the exposure on the EVG 420. Expose for a time equivalent to 240 mj/cm^2. Use the mask layer-1: Back-etch.
   (c) Develop the wafers on EVG 122. Use MF322 developer. Recipe: DEV-1SP
   (d) Performan inspection and check for the line width.
   (e) Plasma Etch the wafer using DRYTEK. Run the recipe *Stdsin* for 75 seconds.
7. Clean the wafers. As mentioned in step 3.
8. Opening of windows in the SiN_X on the front side
   (a) Spincoat 3.1 μm of SPR 3012, and perform a bake.
   (b) Perform the exposure on the EVG 420. Expose for a time equivalent to 240 mj/cm^2. Use the mask layer-1: Catalyst.
   (c) Develop the wafers on EVG 122. Use MF322 developer. Recipe: DEV-1SP
   (d) Performan inspection and check for the line width.

(e) Plasma Etch the wafer using DRYTEK. Run the recipe *Stdsin* for 75 seconds.

9. Catalyst depostion and patterning

   (a) Use the *Trikon Sigma* sputter coater for the deposition of the catalyst Mo layer on the process wafers.Use the recipe *Mo_50nm_50c*.

   (b) Coat the wafer with 1.4 μm of SPR 3012.

   (c) Expose it on EVG 420 for a time equivalent of 55 mj/cm^2. Use the mask, Layer: Mo catalyst.

   (d) Develop the wafers an inspect for the structures.

   (e) Plasma Etch the wafer using Trikon Omega 201 Plasma etcher. Run the recipe *MO_test2*

10. Strip the photoresist on Tepla. Use program 1.

11. Graphene Growth

   (a) Grow graphene on the wafer using AIXTRON Blackmagic. Use the reipe *Mo_NEW_915C_20min*. Also, run the recipe for 10, 30 and40 minutes.

   (b) Perform a Raman Spectroscopy to analyze the quality or graphene.

12. Metal Evaporation

   (a) Perform a manual coating of nLOF 2020. Deposit a layer of 3 μm..

   (b) Expose the wafers using EVG 420. Expose for a time equivalent of 55 mj/cm^2. Use the mask, Layer: Metal.

   (c) Develop the wafers manually. Use MF 322 developer.

   (d) Inspect the wafers for line width.

   (e) Use CHA to evaporate the metal on the wafer. First evaporate 10nm of Cr followed by 100 nm of Au.

13. Lift-off

   (a) Use NMP at 70 °C in an ultrasonic bath for 5 minutes.

   (b) Rinse in water and dry the wafers.

14. Wet Etching of bulk Silicon

   (a) Wet etch the oxide on back using BOE (1:7) for 10 minutes and use the holder for front side protection.

   (b) Set the TMAH bath to 80°C and etch he wafers for 14.5 hours. Do inspections in between to check the rate of etching. Land on the oxide layer.

   (c) Etch the Mo on the front side using H_2O_2.

   (d) Etch the oxide on the top using Vapor HF. Perform a cycle of etching for a time of 1 minute and then inspect. Perform the next etching cycle if graphene membranes are not released.

A.3. Transfer-free Graphene over radial holes

1. Start with 4-inch DSP wafer.
2. Creatio of Zero Layers (with alignment markers).
   (a) Spincoat 1.4 μm of SPR 3012, and perform a bake.
   (b) Expose the wafers on PAS 5500/80 automatic waferstepper. Use recipe "ZEFWAM" and set the exposure energy to 120 mj/cm^2. Mask: COMURK.
   (c) Develop the wafers on EVG 122. Use MF322 developer. Recipe: DEV-1SP
   (d) Performan inspection and check for the line width.
   (e) Plasma Etch the wafer using Trikon Omega 201 Plasma etcher. Run the recipe URK_NPD.
3. Cleaning of the wafers
   (a) Use the Tepla plasma system to remove the photoresist in an oxygen plasma.
   (b) 10 minutes in 100% nitric acid.
   (c) Rinse in the Quick Dump Rinser with the standard program until the resistivity is 5 MΩ.
   (d) 10 minutes in fumng nitric acid (65%) at 110°C.
   (e) Rinse in the Quick Dump Rinser with the standard program until the resistivity is 5 MΩ.
   (f) Dry the wafers.
4. PECVD Oxide Deposition on front and back
   (a) Use Novellus Concept 1 to deposit deposit standard oxide of 6 μm thick. Use the recipe *xxstdsio* for 1 minute.
   (b) Repeat the process for the other side of the wafer.
5. PECVD Nitride
   (a) Use Novellus Concept 1 to deposit deposit $Si N_X$ of 300 nm thick. Use the recipe *xxstdsin* for 30 seconds.
   (b) Model the layer thickness using Woollam Ellipsometer.
6. Opening of windows in the SiO on the back side
   (a) Spincoat 3.1 μm of SPR 3012, and perform a bake.
   (b) Perform the exposure on the EVG 420. Expose for a time equivalent to 240 mj/cm^2. Use the mask layer-1: Back-etch.
   (c) Develop the wafers on EVG 122. Use MF322 developer. Recipe: DEV-1SP
   (d) Perform an inspection and check for the line width.
   (e) Plasma Etch the wafer using DRYTEK. Run the recipe *Stdsio* for 13 minutes.
7. Clean the wafers. As mentioned in step 3.
8. Catalyst depostion and patterning
   (a) Use the *Trikon Sigma* sputter coater for the deposition of the catalyst Mo layer on the process wafers.Use the recipe *Mo_50nm_50c*.
   (b) Coat the wafer with 1.4 μm of SPR 3012.

(c) Expose it on EVG 420 for a time equivalent of 55 mj/cm^2. Use the mask, Layer: Mo catalyst.

(d) Develop the wafers an inspect for the structures.

(e) Plasma Etch the wafer using Trikon Omega 201 Plasma etcher. Run the recipe *MO_test2*

9. Strip the photoresist on Tepla. Use program 1.

10. Graphene Growth

(a) Grow graphene on the wafer using AIXTRON Blackmagic. Use the reipe *Mo_NEW_915C_20min*. Also, run the recipe for 10, 30 and40 minutes.

(b) Perform a Raman Spectroscopy to analyze the quality or graphene.

11. Metal Evaporation

(a) Perform a manual coating of nLOF 2020. Deposit a layer of 3 μm.

(b) Expose the wafers using EVG 420. Expose for a time equivalent of 55 mj/cm^2. Use the mask, Layer: Metal.

(c) Develop the wafers manually. Use MF 322 developer.

(d) Inspect the wafers for line width.

(e) Use CHA to evaporate the metal on the wafer. First evaporate 10nm of Cr followed by 100 nm of Au.

12. Lift-off

(a) Use NMP at 70 °C in an ultrasonic bath for 5 minutes.

(b) Rinse in water and dry the wafers.

13. DRI Etching of bulk Silicon

(a) Etch the wafers from the backside using *Omega i2L Rapier*.

(b) inspections in between to check the rate of etching. Land on the oxide layer.

(c) Etch the Mo on the front side using H_2O_2.

(d) Etch the oxide and SiN_X on the top using Vapor HF. Perform a cycle of etching for a time of 1 minute and then inspect. Perform the next etching cycle if graphene membranes are not released.

A.4. Transfer-free Graphene on SiC Support Membrane

1. Start with 4-inch DSP wafer.

2. Creatio of Zero Layers (with alignment markers).

(a) Spincoat 1.4 μm of SPR 3012, and perform a bake.

(b) Expose the wafers on PAS 5500/80 automatic waferstepper. Use recipe "ZEFWAM" and set the exposure energy to 120 mj/cm^2. Mask: COMURK.

(c) Develop the wafers on EVG 122. Use MF322 developer. Recipe: DEV-1SP

(d) Performan inspection and check for the line width.

(e) Plasma Etch the wafer using Trikon Omega 201 Plasma etcher. Run the recipe URK_NPD.

3. Cleaning of the wafers
   (a) Use the Tepla plasma system to remove the photoresist in an oxygen plasma.
   (b) 10 minutes in 100% nitric acid.
   (c) Rinse in the Quick Dump Rinser with the standard program until the resistivity is 5 MΩ.
   (d) 10 minutes in fumng nitric acid (65%) at 110°C.
   (e) Rinse in the Quick Dump Rinser with the standard program until the resistivity is 5 MΩ.
   (f) Dry the wafers.
4. Oxidation
   (a) Oxidation: for 600 nm of oxide, Use wet oxidation at 1100°C for 42 minutes.
   (b) Measure the oxide thickness using Leitz MPV-SP.
5. Opening of windows in the SiO on the back side
   (a) Spincoat 3.1 μm of SPR 3012, and perform a bake.
   (b) Perform the exposure on the EVG 420. Expose for a time equivalent to 240 mj/cm^2. Use the mask layer-1: Back-etch.
   (c) Develop the wafers on EVG 122. Use MF322 developer. Recipe: DEV-1SP
   (d) Perform an inspection and check for the line width.
   (e) Plasma Etch the wafer using DRYTEK. Run the recipe *Stdsio* for 70 seconds.
6. Clean the wafers. As mentioned in step 3.
7. PECVD SiC
   (a) Use Novellus Concept 1 to deposit deposit SiC of 500 nm thick. Use the recipe $ls800nm_2$ for 1 minute.
   (b) Model the layer thickness using Woollam Ellipsometer.
8. Catalyst depostion and patterning
   (a) Use the *Trikon Sigma* sputter coater for the deposition of the catalyst Mo layer on the process wafers.Use the recipe *Mo_50nm_50c*.
   (b) Coat the wafer with 1.4 μm of SPR 3012.
   (c) Expose it on EVG 420 for a time equivalent of 55 mj/cm^2. Use the mask, Layer: Mo catalyst.
   (d) Develop the wafers an inspect for the structures.
   (e) Plasma Etch the wafer using Trikon Omega 201 Plasma etcher. Run the recipe *MO_test2*
9. Strip the photoresist on Tepla. Use program 1.
10. Graphene Growth
    (a) Grow graphene on the wafer using AIXTRON Blackmagic. Use the reipe *Mo_NEW_915C_20min*. Also, run the recipe for 10, 30 and40 minutes.
    (b) Perform a Raman Spectroscopy to analyze the quality or graphene.
11. Metal Evaporation

(a) Perform a manual coating of nLOF 2020. Deposit a layer of 3 μm.

(b) Expose the wafers using EVG 420. Expose for a time equivalent of 55 mj/cm^2. Use the mask, Layer: Metal.

(c) Develop the wafers manually. Use MF 322 developer.

(d) Inspect the wafers for line width.

(e) Use CHA to evaporate the metal on the wafer. First evaporate 10nm of Cr followed by 100 nm of Au.

12. Lift-off

(a) Use NMP at 70 °C in an ultrasonic bath for 5 minutes.

(b) Rinse in water and dry the wafers.

13. Wet Etching of bulk Silicon

(a) Wet etch the oxide on back using BOE (1:7) for 10 minutes and use the holder for front side protection.

(b) Set the TMAH bath to 80°C and etch he wafers for 14.5 hours. Do inspections in between to check the rate of etching.

(c) Wet etch the oxide on back using BOE (1:7) for 10 minutes

(d) Etch the Mo on the front side using H_2O_2.

B

Deep Reactive Ion Etching

This process is used to achieve trenches with his aspect ratios. The etching consists of a series of etching and passivisation steps.

First, the substrate (generally Si with SiO as the hardmask) is etched with a Flourine based etchant. This is followed by a passivisation (based on CF_2) coating of the etched. The whole etched region is protected by the coating. Further the trench is further exposed to the highly directional etchant ions, which attack the passivisation layer on the bottom of the trench, while it doesn't disturb the passivisation layer on the side walls. This is repeated for a number of times and trenches of high aspect ratios are got.

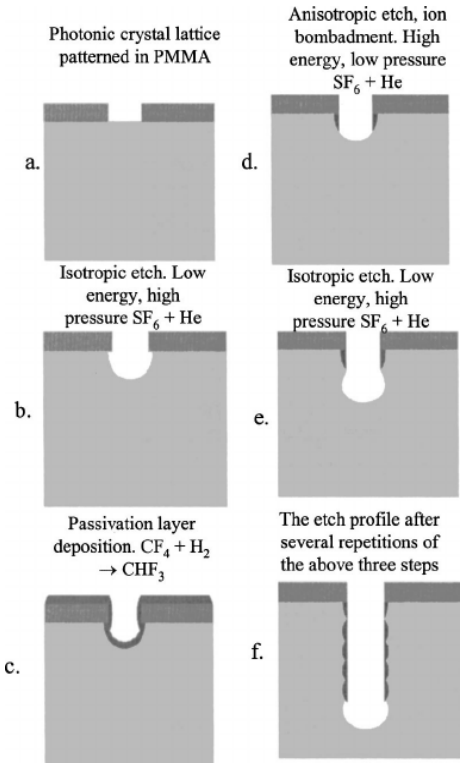

Figure B.1: Deep reactive ion etching through Bosch process. Sourced from [69]

C

Layout

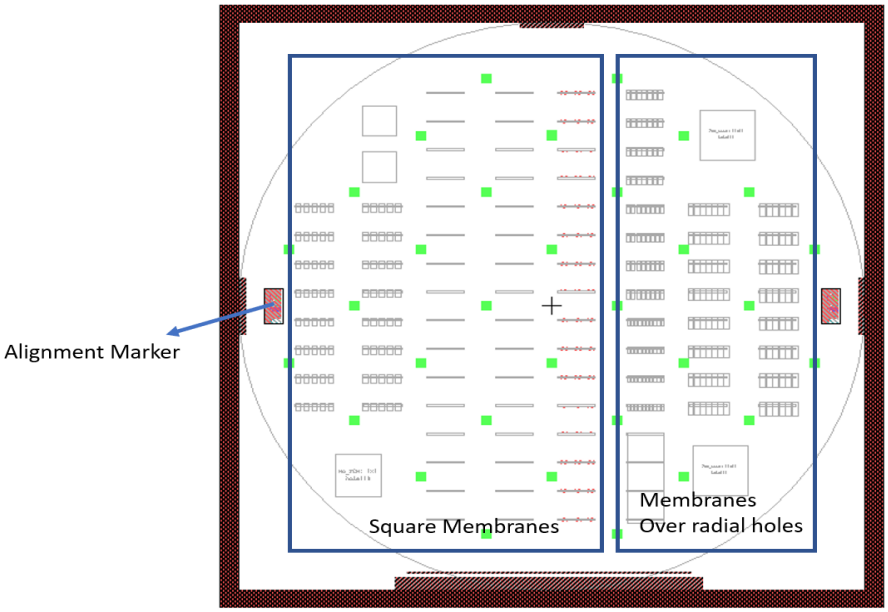

Figure C.1: The layout of the complete wafer.

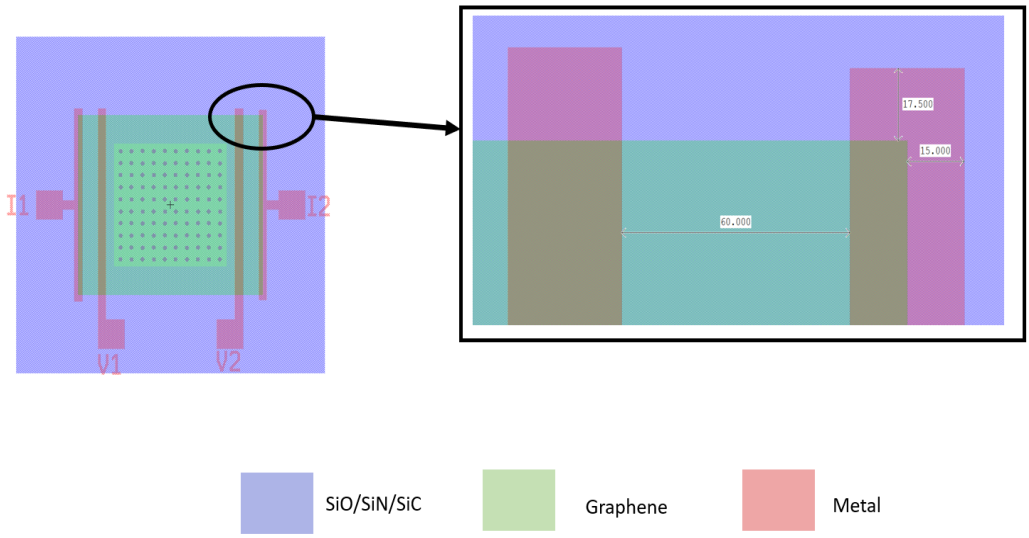

Figure C.2: Overhangs of the metal contacts on the substrate.

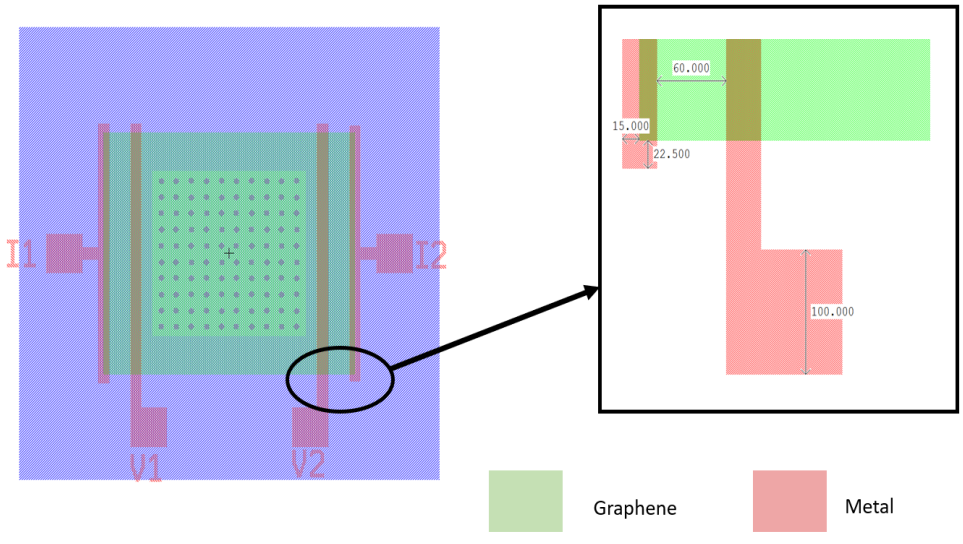

Figure C.3: Spacing and the pad area of the contacts.

D

Raman Data

D.1. For Different Growth Rates

D.1.1. 40 minutes

Table D.1: Raman spectrum analysis

Measurement	I_D	I_G	I_{2D}	I_D/I_G	I_2D/I_G	FHWM (cm^{-1})
1	0.24	0.95	0.43	0.25	0.45	51.57
2	0.31	1	0.39	0.31	0.39	61.02
3	0.42	0.89	0.41	0.47	0.46	63.30

D.1.2. 30 Minutes

Table D.2: Raman spectrum analysis

Measurement	I_D	I_G	I_{2D}	I_D/I_G	I_2D/I_G	FHWM (cm^{-1})
1	0.47	0.86	0.48	0.54	0.55	72.32
2	0.43	0.82	0.52	0.52	0.63	68.30
3	0.51	0.82	0.52	0.62	0.63	65.25

D.1.3. 20 Minutes

Table D.3: Raman spectrum analysis

Measurement	I_D	I_G	I_{2D}	I_D/I_G	I_2D/I_G	FHWM (cm^{-1})
1	0.46	0.97	0.46	0.47	0.47	61.53
2	0.49	0.82	0.57	0.59	0.62	57.20
3	0.57	0.91	0.52	0.62	0.54	60.21

D.1.4. 10 Minutes

Table D.4: Raman spectrum analysis

Measurement	I_D	I_G	I_{2D}	I_D/I_G	I_2D/I_G	FHWM (cm^{-1})
1	0.46	1	0.39	0.46	0.39	65.51
2	0.49	0.96	0.43	0.51	0.44	52.10
3	0.42	0.98	0.42	0.42	0.42	56.15

D.2. Analysis of graphene quality

D.2.1. As Grown

Table D.5: Raman spectrum analysis, as grown.

Measurement	I_D	I_G	I_{2D}	I_D/I_G	I_2D/I_G	FHWM (cm^{-1})
1	0.46	1	0.47	0.46	0.47	62.30
2	0.42	0.93	0.51	0.45	0.54	61.25

D.2.2. After complete fabrication

Table D.6: Raman spectrum analysis, after complete fabrication.

Measurement	I_D	I_G	I_{2D}	I_D/I_G	I_2D/I_G	FHWM (cm^{-1})
1	0.70	0.92	0.50	0.76	0.54	74.21
2	0.63	0.94	0.53	0.67	0.56	61.35

D.3. Raman analysis of oxidized Mo and Subsequent Graphene Growth

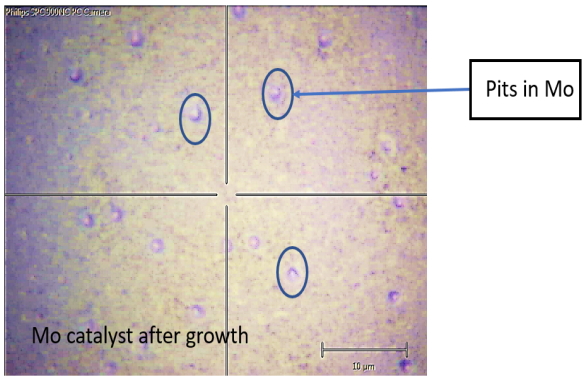

Figure D.1: The pits, due to oxidation are visible in Mo.

D.3.1. Raman Analysis on one such Mo layer, after growth

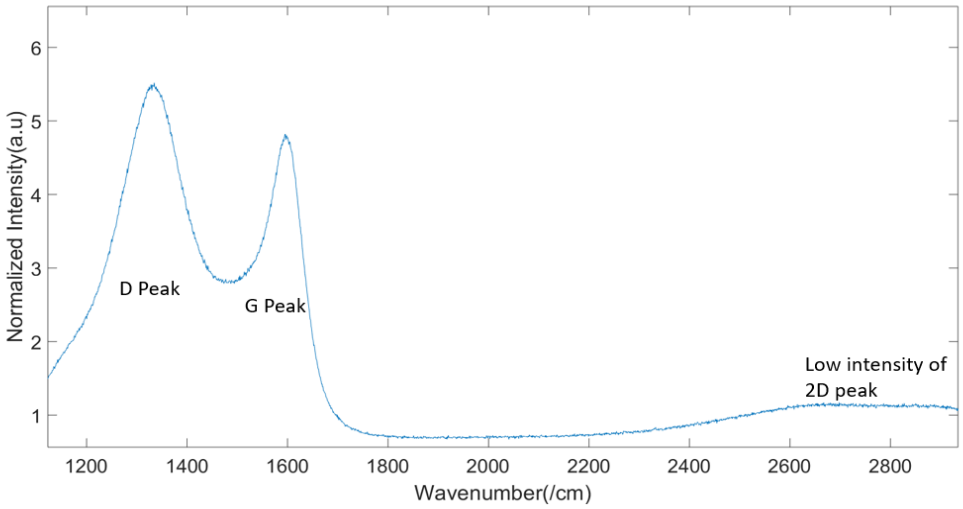

Figure D.2: The absence of a prominent 2D peak is visible. The membrane is not graphene.

E

Optical Profile Reconstruction

E.1. Deflection profile for Corresponding Differential Profile

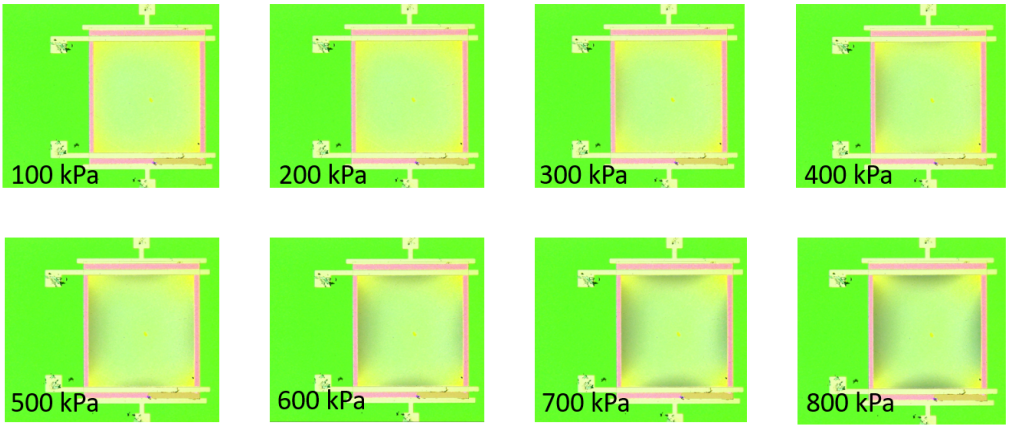

Figure E.1: Optical Deflection Profile.

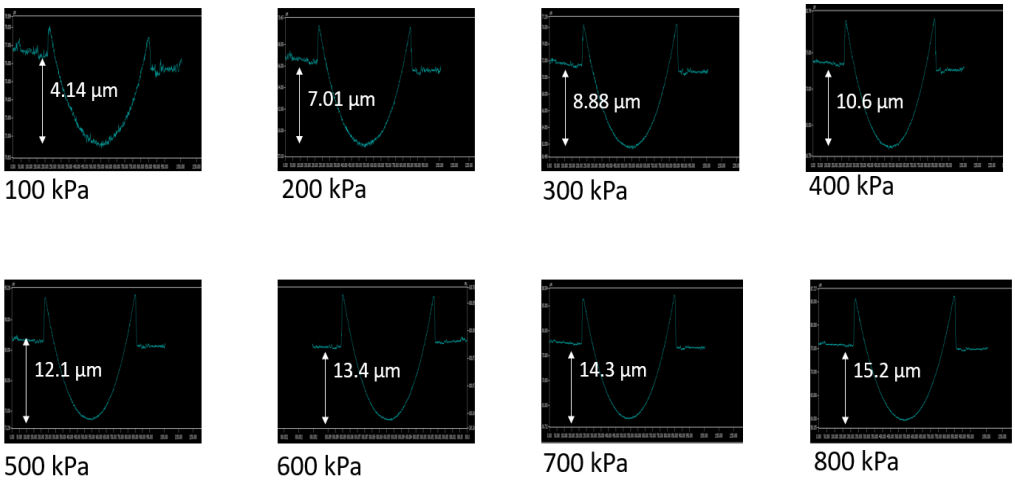

Figure E.2: Measured Deflection Profile.

F

Measurement Data

F.1. SEM Images

F.1.1. Top View

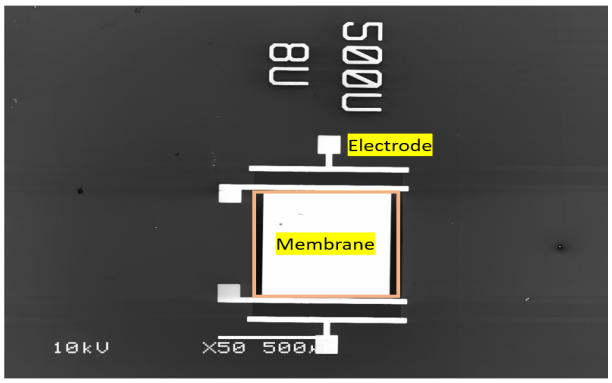

Figure F.1: SEM capture of the top-view of a single device. The electrodes and the membrane are visible.

F.1.2. Cross-section of the device.

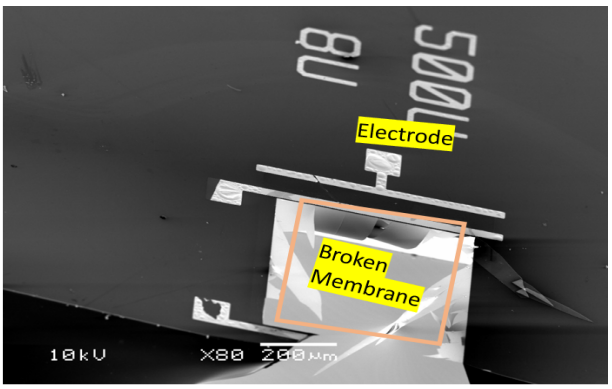

Figure F.2: A cross section view of a broken membrane.

List of Figures

List of Tables

Bibliography

[1] S.-E. Zhu, M. Krishna Ghatkesar, C. Zhang, and G. Janssen, "Graphene based piezoresistive pressure sensor," *Applied Physics Letters*, vol. 102, no. 16, p. 161904, 2013.

[2] Q. Wang, W. Hong, and L. Dong, "Graphene "microdrums" on a freestanding perforated thin membrane for high sensitivity mems pressure sensors," *Nanoscale*, vol. 8, no. 14, pp. 7663–7671, 2016.

[3] A. Smith, F. Niklaus, A. Paussa, S. Vaziri, A. C. Fischer, M. Sterner, F. Forsberg, A. Delin, D. Esseni, P. Palestri, *et al.*, "Electromechanical piezoresistive sensing in suspended graphene membranes," *Nano letters*, vol. 13, no. 7, pp. 3237–3242, 2013.

[4] M. Schulz, "The end of the road for silicon?," *Nature*, vol. 399, no. 6738, p. 729, 1999.

[5] A. K. Geim and K. S. Novoselov, "The rise of graphene," in *Nanoscience and Technology: A Collection of Reviews from Nature Journals*, pp. 11–19, World Scientific, 2010.

[6] J. Dauber, A. A. Sagade, M. Oellers, K. Watanabe, T. Taniguchi, D. Neumaier, and C. Stampfer, "Ultra-sensitive hall sensors based on graphene encapsulated in hexagonal boron nitride," *Applied Physics Letters*, vol. 106, no. 19, p. 193501, 2015.

[7] J. D. Fowler, M. J. Allen, V. C. Tung, Y. Yang, R. B. Kaner, and B. H. Weiller, "Practical chemical sensors from chemically derived graphene," *ACS nano*, vol. 3, no. 2, pp. 301–306, 2009.

[8] "Graphene, the wonder material." https://www.laboratory-journal.com/science/material-science/wonder-material-graphene, Access Date= 05/06/19.

[9] D. G. Papageorgiou, I. A. Kinloch, and R. J. Young, "Mechanical properties of graphene and graphene-based nanocomposites," *Progress in Materials Science*, vol. 90, pp. 75–127, 2017.

[10] S. Wagner, C. Weisenstein, A. D. Smith, M. Östling, S. Kataria, and M. C. Lemme, "Graphene transfer methods for the fabrication of membrane-based nems devices," *Microelectronic Engineering*, vol. 159, pp. 108–113, 2016.

[11] S. Vollebregt, B. Alfano, F. Ricciardella, A. Giesbers, Y. Grachova, H. van Zeijl, T. Polichetti, and P. Sarro, "A transfer-free wafer-scale cvd graphene fabrication process for mems/nems sensors," in *2016 IEEE 29th International Conference on Micro Electro Mechanical Systems (MEMS)*, pp. 17–20, IEEE, 2016.

[12] "Mcleod vacuum gauge." http://instrumentationandcontrollers.blogspot.com/2010/12/mcleod-vacuum-gauge.html, Access Date= 05/06/19.

[13] "Piezoressistive si based pressure sensor." https://www.avnet.com/wps/portal/abacus/solutions/technologies/sensors/pressure-sensors/, Access Date= 05/06/19.

[14] "Pirani gauge." http://instrumentationandcontrollers.blogspot.com/2012/03/pirani-gauge-thermal-conductivity-gauge.html, Access Date= 05/06/19.

[15] "Ionisation gauge." https://www.supervacoils.com/vacuum-gauges-explained/, Access Date= 05/06/19,.

[16] Z. He, W. Chen, B. Liang, C. Liu, L. Yang, D. Lu, Z. Mo, H. Zhu, Z. Tang, and X. Gui, "Capacitive pressure sensor with high sensitivity and fast response to dynamic interaction based on graphene and porous nylon networks," *ACS applied materials & interfaces*, vol. 10, no. 15, pp. 12816–12823, 2018.

[17] S. Watson, M. J. Gander, W. N. MacPherson, J. S. Barton, J. D. Jones, T. Klotzbuecher, T. Braune, J. Ott, and F. Schmitz, "Laser-machined fibers as fabry-perot pressure sensors," *Applied optics*, vol. 45, no. 22, pp. 5590–5596, 2006.

[18] A. A. Barlian, W.-T. Park, J. R. Mallon, A. J. Rastegar, and B. L. Pruitt, "Semiconductor piezoresistance for microsystems," *Proceedings of the IEEE*, vol. 97, no. 3, pp. 513–552, 2009.

[19] C. S. Smith, "Piezoresistance effect in germanium and silicon," *Physical review*, vol. 94, no. 1, p. 42, 1954.

[20] J. Bardeen and W. Shockley, "Deformation potentials and mobilities in non-polar crystals," *Physical review*, vol. 80, no. 1, p. 72, 1950.

[21] X. Liu, C. Tang, X. Du, S. Xiong, S. Xi, Y. Liu, X. Shen, Q. Zheng, Z. Wang, Y. Wu, *et al.*, "A highly sensitive graphene woven fabric strain sensor for wearable wireless musical instruments," *Materials Horizons*, vol. 4, no. 3, pp. 477–486, 2017.

[22] M. A. Hopcroft, W. D. Nix, and T. W. Kenny, "What is the young's modulus of silicon?," *Journal of microelectromechanical systems*, vol. 19, no. 2, pp. 229–238, 2010.

[23] "Properties of silicon-oxide." https://www.azom.com/properties.aspx?ArticleID=1114.

[24] O. Tabata, K. Kawahata, S. Sugiyama, and I. Igarashi, "Mechanical property measurements of thin films using load-deflection of composite rectangular membranes," *Sensors and actuators*, vol. 20, no. 1-2, pp. 135–141, 1989.

[25] L. Tong, M. Mehregany, and L. G. Matus, "Mechanical properties of 3c silicon carbide," *Applied physics letters*, vol. 60, no. 24, pp. 2992–2994, 1992.

[26] H. Hosseinzadegan, C. Todd, A. Lal, M. Pandey, M. Levendorf, and J. Park, "Graphene has ultra high piezoresistive gauge factor," in *2012 IEEE 25th international conference on micro electro mechanical systems (MEMS)*, pp. 611–614, IEEE, 2012.

[27] "Graphene: structure and shape." https://www.graphene-info.com/graphene-structure-and-shape Access Date= 05/06/19,.

[28] A. A. Balandin, S. Ghosh, W. Bao, I. Calizo, D. Teweldebrhan, F. Miao, and C. N. Lau, "Superior thermal conductivity of single-layer graphene," *Nano letters*, vol. 8, no. 3, pp. 902–907, 2008.

[29] A. K. Geim and K. S. Novoselov, "The rise of graphene," in *Nanoscience and Technology: A Collection of Reviews from Nature Journals*, pp. 11–19, World Scientific, 2010.

[30] P. Zhang, L. Ma, F. Fan, Z. Zeng, C. Peng, P. E. Loya, Z. Liu, Y. Gong, J. Zhang, X. Zhang, *et al.*, "Fracture toughness of graphene," *Nature communications*, vol. 5, p. 3782, 2014.

[31] Z. Zhang, L. H. Klausen, M. Chen, and M. Dong, "Electroactive scaffolds for neurogenesis and myogenesis: Graphene-based nanomaterials," *Small*, vol. 14, no. 48, p. 1801983, 2018.

[32] A. C. Neto, F. Guinea, N. M. Peres, K. S. Novoselov, and A. K. Geim, "The electronic properties of graphene," *Reviews of modern physics*, vol. 81, no. 1, p. 109, 2009.

[33] K. S. Kim, Y. Zhao, H. Jang, S. Y. Lee, J. M. Kim, K. S. Kim, J.-H. Ahn, P. Kim, J.-Y. Choi, and B. H. Hong, "Large-scale pattern growth of graphene films for stretchable transparent electrodes," *nature*, vol. 457, no. 7230, p. 706, 2009.

[34] L. Falkovsky, "Optical properties of graphene," in *Journal of Physics: Conference Series*, vol. 129, p. 012004, IOP Publishing, 2008.

[35] C. Reddy, S. Rajendran, and K. Liew, "Equilibrium configuration and continuum elastic properties of finite sized graphene," *Nanotechnology*, vol. 17, no. 3, p. 864, 2006.

[36] I. Ovid'Ko, "Mechanical properties of graphene," *Rev. Adv. Mater. Sci*, vol. 34, no. 1, pp. 1–11, 2013.

[37] I. Childres, L. A. Jauregui, W. Park, H. Cao, and Y. P. Chen, "Raman spectroscopy of graphene and related materials," *New developments in photon and materials research*, vol. 1, 2013.

[38] I. Childres, L. A. Jauregui, W. Park, H. Cao, and Y. P. Chen, "Raman spectroscopy of graphene and related materials," *New developments in photon and materials research*, vol. 1, 2013.

[39] A. Das, B. Chakraborty, and A. Sood, "Raman spectroscopy of graphene on different substrates and influence of defects," *Bulletin of Materials Science*, vol. 31, no. 3, pp. 579–584, 2008.

[40] Y. Hao, Y. Wang, L. Wang, Z. Ni, Z. Wang, R. Wang, C. K. Koo, Z. Shen, and J. T. Thong, "Probing layer number and stacking order of few-layer graphene by raman spectroscopy," *small*, vol. 6, no. 2, pp. 195–200, 2010.

[41] X. Li, W. Cai, L. Colombo, and R. S. Ruoff, "Evolution of graphene growth on ni and cu by carbon isotope labeling," *Nano letters*, vol. 9, no. 12, pp. 4268–4272, 2009.

[42] "Cvd growth of graphene." https://www.comsol.com/blogs/synthesizing-graphene-chemical-vapor-deposition/, Access Date= 05/06/19.

[43] S. Futko, B. Shulitskii, V. Labunov, and E. Ermolaeva, "Parametric investigation of the isothermal kinetics of growth of graphene on a nickel catalyst in the process of chemical vapor deposition of hydrocarbons," *Journal of Engineering Physics and Thermophysics*, vol. 89, no. 6, pp. 1487–1499, 2016.

[44] X. Li, Y. Zhu, W. Cai, M. Borysiak, B. Han, D. Chen, R. D. Piner, L. Colombo, and R. S. Ruoff, "Transfer of large-area graphene films for high-performance transparent conductive electrodes," *Nano letters*, vol. 9, no. 12, pp. 4359–4363, 2009.

[45] Y. Hwangbo, C.-K. Lee, S.-M. Kim, J.-H. Kim, K.-S. Kim, B. Jang, H.-J. Lee, S.-K. Lee, S.-S. Kim, J.-H. Ahn, *et al.*, "Fracture characteristics of monolayer cvd-graphene," *Scientific reports*, vol. 4, p. 4439, 2014.

[46] S. Gorantla, A. Bachmatiuk, J. Hwang, H. A. Alsalman, J. Y. Kwak, T. Seyller, J. Eckert, M. G. Spencer, and M. H. Rümmeli, "A universal transfer route for graphene," *Nanoscale*, vol. 6, no. 2, pp. 889–896, 2014.

[47] N. Peltekis, S. Kumar, N. McEvoy, K. Lee, A. Weidlich, and G. S. Duesberg, "The effect of downstream plasma treatments on graphene surfaces," *Carbon*, vol. 50, no. 2, pp. 395–403, 2012.

[48] T. E. Beechem, R. A. Shaffer, J. Nogan, T. Ohta, A. B. Hamilton, A. E. McDonald, and S. W. Howell, "Self-heating and failure in scalable graphene devices," *Scientific reports*, vol. 6, p. 26457, 2016.

[49] Y. Grachova, S. Vollebregt, A. L. Lacaita, and P. M. Sarro, "High quality wafer-scale cvd graphene on molybdenum thin film for sensing application," *Procedia Engineering*, vol. 87, pp. 1501–1504, 2014.

[50] J.-K. K. D.-W. L. X. L. Xiaohu Zheng, Xing Chen, "Measurement of the gauge factor of few-layer graphene," *Journal of Micro/Nanolithography, MEMS, and MOEMS*, vol. 12, no. 1, pp. 1 – 4 – 4, 2013.

[51] D. Maier-Schneider, J. Maibach, and E. Obermeier, "A new analytical solution for the load-deflection of square membranes," *Journal of microelectromechanical systems*, vol. 4, no. 4, pp. 238–241, 1995.

[52] S. Vollebregt, F. Ricciardella, J. Romijn, M. Singh, S. Shi, and P. Sarro, "A transfer-free approach to wafer-scale graphene deposited by chemical vapour deposition," *Graphene 2018*, 2018.

[53] S. Sinha. PhD thesis, 2018.

[54] P. Nemes-Incze, Z. Osváth, K. Kamarás, and L. Biró, "Anomalies in thickness measurements of graphene and few layer graphite crystals by tapping mode atomic force microscopy," *Carbon*, vol. 46, no. 11, pp. 1435–1442, 2008.

[55] R. Xu, Y. Wang, B. Liu, and D. Fang, "Mechanics interpretation on the bending stiffness and wrinkled pattern of graphene," *Journal of Applied Mechanics*, vol. 80, no. 4, p. 040910, 2013.

[56] Q. Zhou, J. Zheng, S. Onishi, M. Crommie, and A. K. Zettl, "Graphene electrostatic microphone and ultrasonic radio," *Proceedings of the National Academy of Sciences*, vol. 112, no. 29, pp. 8942–8946, 2015.

[57] "Types of photomasks." ://www.mems-exchange.org/users/masks/guidelines.html.

[58] E. N. Hoggan, D. Flowers, J. M. DeSimone, and R. G. Carbonell, "Spin coating and photolithography using liquid and supercritical carbon dioxide," in *Advances in Resist Technology and Processing XIX*, vol. 4690, pp. 1217–1223, International Society for Optics and Photonics, 2002.

[59] "Koh etching." :https://cleanroom.byu.edu/KOH urldate = 05/06/19.

[60] Y. Shuai, C. Wu, W. Zhang, Y. Li, X. Liu, and J. Zhu, "Optimization of (100)-si tmah etching for uncooled infrared detector," in *International Symposium on Photoelectronic Detection and Imaging 2009: Advances in Infrared Imaging and Applications*, vol. 7383, p. 73830H, International Society for Optics and Photonics, 2009.

[61] N. Stavitski, M. van Dal, J. Klootwijk, R. A. Wolters, A. Y. Kovalgin, and J. Schmitz, "Cross–bridge kelvin resistor (cbkr) structures for silicide–semiconductor junctions characterization," in *Proc. of the 9th annual workshop on Semiconductor Advances for Future Electronics and Sensors 2006, 23–24 Nov. 2006, Veldhoven, Netherlands*, pp. 436–438, 2006.

[62] K. Nagashio, T. Nishimura, K. Kita, and A. Toriumi, "Metal/graphene contact as a performance killer of ultra-high mobility graphene analysis of intrinsic mobility and contact resistance," in *2009 IEEE International Electron Devices Meeting (IEDM)*, pp. 1–4, IEEE, 2009.

[63] A. Vittore, M. R. Acocella, and G. Guerra, "Edge-oxidation of graphites by hydrogen peroxide," *Langmuir*, vol. 35, no. 6, pp. 2244–2250, 2019.

[64] F. Giubileo and A. Di Bartolomeo, "The role of contact resistance in graphene field-effect devices," *Progress in Surface Science*, vol. 92, no. 3, pp. 143–175, 2017.

[65] J. A. Robinson, M. LaBella, M. Zhu, M. Hollander, R. Kasarda, Z. Hughes, K. Trumbull, R. Cavalero, and D. Snyder, "Contacting graphene," *Applied Physics Letters*, vol. 98, no. 5, p. 053103, 2011.

[66] A. Quellmalz, A. D. Smith, K. Elgammal, X. Fan, A. Delin, M. Ostling, M. Lemme, K. B. Gylfason, and F. Niklaus, "Influence of humidity on contact resistance in graphene devices," *ACS applied materials & interfaces*, vol. 10, no. 48, pp. 41738–41746, 2018.

[67] K. L. Grosse, M.-H. Bae, F. Lian, E. Pop, and W. P. King, "Nanoscale joule heating, peltier cooling and current crowding at graphene–metal contacts," *Nature nanotechnology*, vol. 6, no. 5, p. 287, 2011.

[68] P. Sun, M. Zhu, K. Wang, M. Zhong, J. Wei, D. Wu, and H. Zhu, "Small temperature coefficient of resistivity of graphene/graphene oxide hybrid membranes," *ACS applied materials & interfaces*, vol. 5, no. 19, pp. 9563–9571, 2013.

[69] S. Venkataraman, J. A. Murakowski, T. N. Adam, J. Kolodzey, and D. W. Prather, "Fabrication of high-fill-factor photonic crystal devices on silicon-on-insulator substrates," *Journal of Micro/Nanolithography, MEMS, and MOEMS*, vol. 2, no. 4, pp. 248–255, 2003.

Transfer-free Graphene-based Differential Pressure Sensor

Raghutham Ramesha
Laboratory of Electronics Components Technology and Materials,
Delft University of Technology
Delft, The Netherlands

Sten Vollebregt
Laboratory of Electronics Components Technology and Materials,
Delft University of Technology
Delft, The Netherlands
s.vollebregt@tudelft.nl

Pasqualina M. Sarro
Laboratory of Electronics Components Technology and Materials,
Delft University of Technology
Delft, The Netherlands

***Abstract*—Graphene is an attractive material to be used for pressure sensors due to its thinness, electrical conductivity, and potential high gauge factor. One of the issues with processing graphene is the scalability, which is largely limited by the transfer process that is required for graphene deposited by chemical vapour deposition (CVD). In this work we employed a novel, transfer-free bulk-micromachining approach to realize graphene-based differential pressure sensors. The devices were successfully fabricated, and the samples were examined under Raman Spectroscopy, and electrically characterized. Further, pressure dependent measurements were performed for a dynamic range of 0 to 80 kPa of differential pressure and the corresponding change in resistance of the membrane was measured. The fabricated device has a sensitivity of 0.077 Ω/kPa and a gauge factor of 2.48.**

Keywords—Graphene, differential pressure sensor, bulk micromachining, piezoresistance, Raman spectroscopy

I. Introduction

Graphene, first isolated in 2004, is a promising material in the world of microelectromechanical systems (MEMS) owing to its excellent mechanical, electrical, optical and chemical properties. The sp^2 hybridised C-C atoms form covalent bonds and these are responsible for its high in plane strength [1]. Some studies have shown CVD graphene to have a piezoresistive gauge factor around 18000 [2]. These factors make graphene a promising material for highly sensitive pressure sensors.

The current state of the art in the area of graphene-based piezoresistive pressure sensor uses graphene membranes that are transferred on to thin dielectric films [3]. Generally, thin SiN_X layers act as the supporting structure for graphene conductors. For dimensions smaller than 50 µm, some researchers have made use of free standing graphene membranes made by transferring graphene over a cavity [4]. When laying on a dielectric film the mechanical properties are defined by the dielectric rather than graphene. This reduces sensitivity, but makes the sensor able to withstand more differential pressure across the membrane. In some works, perforated SiN_X membranes are used as the mechanical support layer and the device sensitivity is higher than for membranes without any perforations [5]. It would be ideal to have free-standing, suspended graphene membranes to achieve devices with very high sensitivity. However, large-area CVD graphene might not be structurally strong enough to survive large pressure differences due to the presence of grain boundaries, wrinkles, and defects [6].

In both cases, graphene transfer is used for the fabrication, a process which introduces polymer contamination, additional wrinkles, and has inherent scaling challenges [7]. In addition, during transfer, there are chances of inducing pin holes and tears in the graphene membrane which might compromise its structural integrity. Finally, transferring graphene over a cavity is problematic as the forces of the transfer process can easily break the membrane.

In this paper, we present a novel transfer-free method to fabricate graphene-based bulk micro-machined pressure sensors,. This method is based on previous results by Vollebregt et al [8], which we extended for the first time to bulk micro-machined SiN_X membranes.

II. Design

When a membrane is loaded by a differential pressure, the out of plane deflection, follows the equation [9],

$$P = A_1 \frac{t\sigma}{a^2/4} + A_2(\nu)\delta^3 \frac{tE}{a^4/16} \qquad (1)$$

Where, P is the differential pressure, A_1 and $A_2(\nu)$ are constants, a is the length of the side, t is the thickness, σ is the initial stress, E is the Young' Modulus and δ is the deflection.

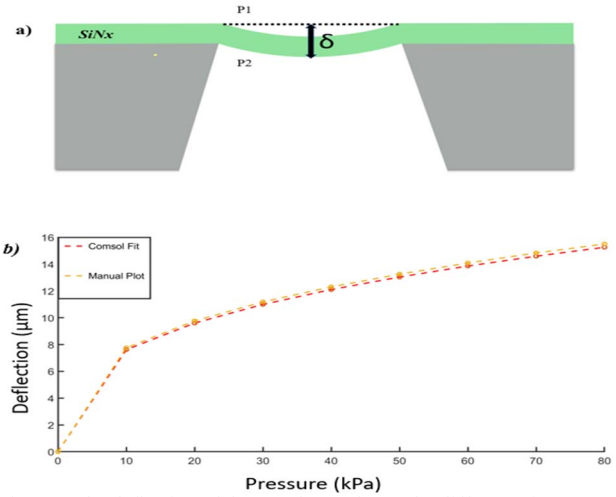

Fig 1. a) The deflection of the membrane due to the difference in pressure P_1 and P_2. b) COMSOL simulation and calculation based on eq. 1 for a differential pressure up to 80 kPa. The SiN_X membrane has a side length of 575 µm and a thickness of 300 nm.

In the device as shown in Fig. 1, the mechanical properties are dominated by the 300 nm thick SiN_X membrane. Simulations were performed using COMSOL Multiphysics using the parameters in Table I, and coherence was seen in the deflection as a function of differential pressure between the theoretical calculation (eq. 1) and the simulation. The deformation in the SiN_X membrane also causes a deformation in the graphene film. This deformation in the graphene film increases the strain. The change in resistance due to strain can be explained by two distinguishable physical phenomena. The total change in resistance can be expressed as [10]

$$\frac{\Delta R}{R} = (1 + 2\nu)\epsilon + \frac{\Delta \rho}{\rho} \quad (2)$$

Where $\frac{\Delta R}{R}$ is the normalized change in resistance, ν is the Poisson's Ratio, ϵ is the strain and $\frac{\Delta \rho}{\rho}$ is the normalized change in resistivity. The first term of the equation, $(1 + 2\nu)\epsilon$ is the geometric factor and is dependent on the mechanical properties of the SiN_X membrane.

In graphene, with increase in strain, the Fermi velocity of electrons decrease [5]. The mobility of electrons in graphene can be expressed as:

$$\mu_e(\epsilon) \sim v_f(\epsilon)^4 \quad (3)$$

Where $\mu_e(\epsilon)$ is the mobility of electrons, $v_f(\epsilon)$ is the Fermi velocity and (ϵ) is the strain. Resistivity of graphene can be expressed as:

$$\rho = \frac{1}{qN_e\mu_e} \quad (4)$$

Where q is the charge of the electron, N_e is the density of electrons and ρ is the resistivity.

From equations (1-4), the application of a differential pressure leads to deformation and hence the strain increases in the graphene film. The increase in strain then leads to an increase in resistance [4].

TABLE I. PROPERTIES OF SiN_X MEMBRANE

Properties of the Device	**Value**
Side length	575 µm
Thickness	300 nm
Young's Modulus	200 GPa [11]
Poisson's Ratio	0.22 [11]
A_1	3.45 [9]
$A_2(v)$	2.48 [9]

III. EXPERIMENTAL

The fabrication process is described in Fig. 2. We use 500 µm thick dual-sided polished 100 mm Si <100> substrates. First, a 300 nm thick oxide was grown using dry thermal oxidation. This was followed by a 300 nm thick LPCVD deposition of SiN_X (Fig 2a). Using plasma etching a window was etched in the backside (Fig 2b). Further, a 50 nm thick

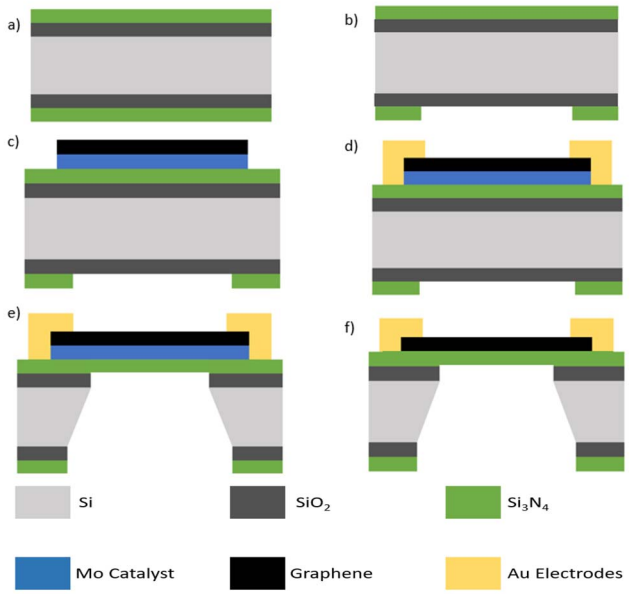

Fig. 2. The main process steps involved in the fabrication of the device: a) oxidation and Si_3N_4 deposition, b) backside etching of masking layer, c) Mo catalyst deposition and CVD graphene deposition, d) Cr/Au contact definition, e) Etching of Si substrate in KOH, followed by etching of the oxide on the top in BOE, f) Mo removal.

Molybdenum (Mo) layer was sputtered and patterned using reactive ion etching. Mo is used here as a catalyst for CVD graphene growth.

Graphene was then grown on the catalyst using an AIXTRON BlackMagic at 915 °C for 20 min using $CH_4/H_2/Ar$ at 25 mbar (Fig 2c). After this 10/100 nm Cr/Au electrodes were defined using e-beam evaporation and a lift-off process (Fig 2d). In the following step, the silicon oxide was removed by BOE (Buffered Oxide Etch 1:7) and this was followed by KOH etching (30 percent at $85°C$), which was further followed by a second BOE(1:7) step to remove the oxide on the nitride membrane (Fig 2e). The final step involved the removal of the Mo catalyst by using H_2O_2 wet etching.

IV. RESULTS AND DISCUSSION

A. *Raman Spectroscopy*

The samples were analysed under Raman spectroscopy during just after graphene growth and after complete fabrication with a 633nm laser (fig. 3). The Raman spectra of graphene has a G peak at 1580 cm^{-1} that represents a primary in plane C-C vibration mode, a defect related D peak at 1330 cm^{-1} and it's 2nd order overtone at 2660 cm^{-1}. Fig 3a represents the Raman spectrum just after graphene deposition. By comparing the intensity ratio of the G and the 2D peaks, (I_{2D}/I_G = 0.39) and the width of the 2D peak of 82 cm^{-1}, the graphene membrane is found to be multi-layered [12]. The ratio I_D/I_G indicates the order of disorder present in the graphene membrane [12]. By comparing Fig 3a and Fig 3b, we can concur that there is an increase in disorder after the graphene membrane is processed. The ratio of I_D/I_G of graphene just after processing is 0.46, while the ratio increases to 0.76 for the graphene membrane after complete processing. This signifies that the order of disorder has increased slightly and this could be due to multiple post processing steps after graphene growth.

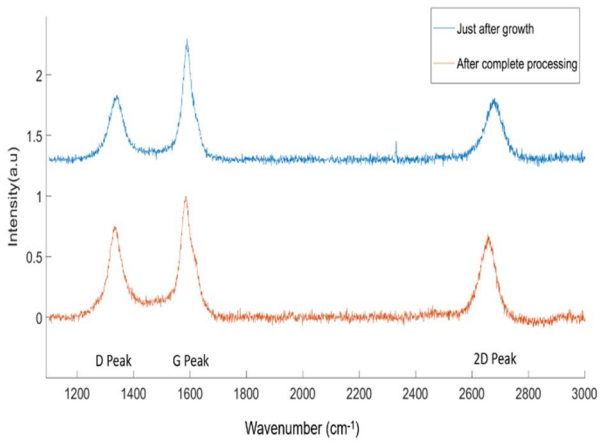

Fig. 3. Raman spectroscopy of membrane: a) when grown, b) after complete fabrication.

B. *Electrical Measurements*

Using a four-point probe method, the total resistance of the graphene membrane was measured. The total resistance can be expressed as:

$$R_t = 2R_c + R_S \tag{5}$$

Where R_t is the total resistance, R_c is the contact resistance between Cr/Au electrodes and graphene, and R_S is the sheet resistance of graphene. By using TLM structures, the Contact Resistance was measured to be 46.88 Ω (1404 Ω-µm). This is shown in Fig 3.

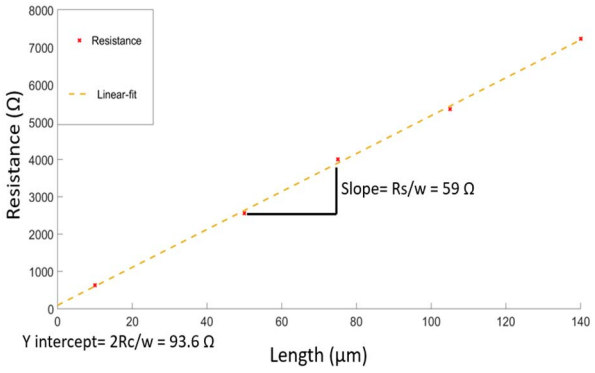

Fig 3. The plot of resistance as a function of the varying length of the graphene conductor. A linear fit is performed, and the slope is the function of the Sheet Resistance of the graphene conductor, while the Y-intercept gives the value of the contact resistance R_C [13]. Here, w = 30 µm, is the width of the graphene conductor. The value of R_S is 1.770 kΩ/sq and R_C is equal to 46.8 Ω or 1404 Ω-µm.

TABLE II. TOTAL RESISTANCE OF GRAPHENE MEMBRANE

Side Length (µm)	Total Resistance (kΩ)	Sheet Resistance of Graphene (kΩ)
575	1.450	1.356
575	1390	1.296
575	1.377	1.283
TLM	1.863	1.770

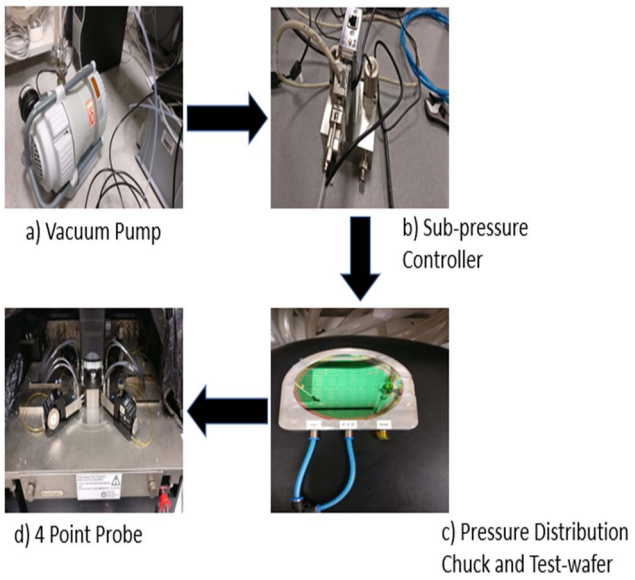

Fig. 4. The measurement setup used to activate the membranes.

The measurement was performed on multiple devices (table II) and the mean value of R_S is 1.42 kΩ/sq with a deviation of 0.20. This value is comparable to the values sheet resistance of CVD graphene reported in literature [1, 14].

C. *Pressure Dependent Measurement*

The measurement setup consisted of a vacuum pump, a pressure controller and a vacuum redistribution chuck (fig. 4). The pressure controller was used to set the amount of vacuum applied to the vacuum redistribution chuck. The vacuum redistribution chuck provided an air-tight seal for the wafer and a controllable vacuum was applied on the wafer through several ports in the chuck. The pressure at the membranes was indicated by the pressure controller.

Using the pressure controller, the differential pressure across the membrane was varied from atmospheric pressure, to 20 kPa sub-atmospheric pressure. Hence, the dynamic range is defined from 0 kPa (atmospheric) to 80 kPa (at 20 kPa setpoint). The pressure was increased by steps of 10 kPa and the resistance of the membrane was measured each time.

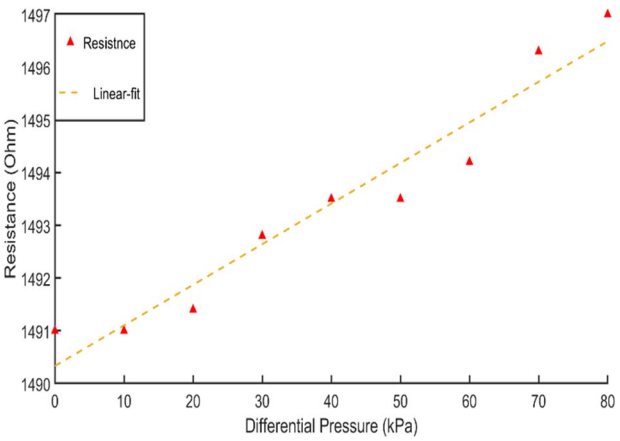

Fig. 5. The variation of the membrane electrical resistance as a function of the differential pressure across the membrane.

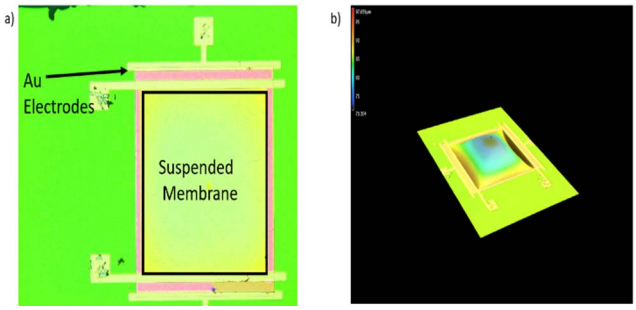

Fig. 6. a) Optical image of the top view of the device. The SiN_X membrane with graphene (green square) and the four Au electrodes are visible. b) The 3D deflection profile of the membrane showing a deflection of 15.25 µm at a differential pressure of 80 kPa, analysed under a Keyence laser microscope.

From the Fig. 5, it is evident that the resistance of the membrane increases as the differential pressure across the membrane increases. The device has a resistance of 1.497 kΩ at 80 kPa differential pressure and 1.491 kΩ at atmospheric pressure. The sensitivity of the device was calculated to be 0.077 Ω/kPa. All the measurements were performed at room temperature.

D. Membrane deflection measurements

The membranes were actuated by the pressure set up (Fig 4) and were then observed under Keyence 3D laser scanning microscope. The profile of the deformed membrane was mapped, and an out of plane deflection of 15.3 µm at a differential pressure of 80 kPa was measured. By considering the simulated values of deformation versus the differential pressure, the membrane has an average strain of 0.16% at a differential pressure of 80 kPa.

TABLE III. COMPARISON WITH DIFFERENT WORKS ON GRAPHENE-BASED PIEZORESISTIVE PRESSURE SENSORS.

Device Type	**Dynamic Range (kPa)**	**Gauge Factor**	**Ref**
Transfer-free graphene on SiN_X	0-80 kPa	2.48	This work
Transferred graphene on SiN_X	0-70 kPa	1.6	[3]
Transferred graphene on perforated SiN_X	0-60 kPa	4.4	[5]

E. Gauge Factor

The Gauge Factor (GF) is given by the equation

$$GF = \frac{\Delta R/R}{\Delta L/L} \qquad (6)$$

Where $\Delta R/R$ is the normalized change in resistance, $\Delta L/L$ is the strain. Using the values obtained from the measurements a GF of 2.48 was determined for this specific device. In comparison to the literature (Table III), our device has a better Gauge Factor than transferred graphene (1.6) on SiN_X and has the highest dynamic range (0-80 kPa).

The transfer-free method of graphene processing can be further extended to achieve graphene membranes on different substrates like SiC or SiO_2. The sensitivity of the device can be further increased by reducing the thickness of the SiN_x support layer.

V. CONCLUSION

We have successfully designed and fabricated transfer-free, bulk micromachined graphene-based pressure sensors. Raman spectroscopy performed at multiple stages during the process displayed a slight deterioration of the graphene membrane, likely due to the post-processing steps. However, the change in the quality of the graphene membrane is minimal and would not hamper the performance of the pressure sensor. Pressure related measurements were performed on the device and the sensitivity was calculated to be 0.077 Ω/kPa with a dynamic differential pressure range of 0 to 80 kPa. The device has a Gauge Factor of 2.48, which is comparable to that of transferred graphene devices.

In this work we demonstrate the feasibility of using a transfer-free process combined with bulk micromachining. The risks of polymer contamination of graphene and other disadvantages that are induced by the transfer process can be minimized. Also, with the integration of graphene processing into standard semiconductor processing, better scalability and throughput can be achieved.

ACKNOWLEDGMENT

The authors are grateful to the engineers and staff of Else Kooi Lab, TU Delft for their support during fabrication.

REFERENCES

[1] Geim, Andre K., and Konstantin S. Novoselov. "The rise of graphene." In Nanoscience and Technology: A Collection of Reviews from Nature Journals. *World Scientific*, 2010. 11-19.

[2] Hosseinzadegan, H., et al. "Graphene has ultra high piezoresistive gauge factor." *2012 IEEE 25th international conference on micro electro mechanical systems (MEMS)*, 2012.

[3] Zhu, S.-E., et al. "Graphene based piezoresistive pressure sensor." *Appl. Phys. Lett.* 102.16 (2013): 161904.

[4] Smith, Anderson D., et al. "Piezoresistive properties of suspended graphene membranes under uniaxial and biaxial strain in nanoelectromechanical pressure sensors." *ACS Nano* 10.11 (2016): 9879-9886.

[5] Wang, Qiugu, Wei Hong, and Liang Dong. "Graphene "microdrums" on a freestanding perforated thin membrane for high sensitivity MEMS pressure sensors." *Nanoscale* 8.14 (2016): 7663-7671.

[6] Wagner, S., et al. "Graphene transfer methods for the fabrication of membrane-based NEMS devices." *Microelectron. Eng.* 159 (2016): 108-113.

[7] Papageorgiou, D.G., I.A. Kinloch, and R.J. Young. "Mechanical properties of graphene and graphene-based nanocomposites." *Prog. in Mater. Sci.* 90 (2017): 75-127.

[8] Vollebregt, S., et al. "A transfer-free wafer-scale CVD graphene fabrication process for MEMS/NEMS sensors." *2016 IEEE 29th International Conference on Micro Electro Mechanical Systems (MEMS)*, 2016.

[9] Maier-Schneider, D., J. Maibach, and E. Obermeier. "A new analytical solution for the load-deflection of square membranes." *J. Microelectromech. Sys.* 4.4 (1995): 238-241.

[10] Barlian, A.A., et al. "Semiconductor piezoresistance for microsystems." *Proc. IEEE* 97.3 (2009): 513-552.

[11] Gavan, K. Babaei, et al. "Impact of fabrication technology on flexural resonances of silicon nitride cantilevers." *Microelectron. Engin.g* 86.4-6 (2009): 1216-1218.

[12] Childres, I., et al. "Raman spectroscopy of graphene and related materials." *New developments in photon and materials research* 1 (2013).

[13] Giubileo, F., and A. Di Bartolomeo. "The role of contact resistance in graphene field-effect devices." *Prog. in Surf. Sci.* 92.3 (2017): 143-175.
[14] Jo, G., et al. "The application of graphene as electrodes in electrical and optical devices." *Nanotechn.* 23.11 (2012): 112001.